UNIVERSIDAD DE CHILE
FACULTAD DE CIENCIAS FÍSICAS Y MATEMÁTICAS
DEPARTAMENTO DE GEOLOGÍA

ANOMALOUS HIGH HALOGEN CONCENTRATION IN WATER DEPLETED ERUPTIVE CENTERS FROM LONQUIMAY VOLCANIC COMPLEX

TESIS PARA OPTAR AL GRADO DE MAGISTER EN CIENCIAS MENCIÓN GEOLOGÍA
MEMORIA PARA OPTAR AL TÍTULO DE GEÓLOGO

FABIÁN EDUARDO TAPIA RODRÍGUEZ

PROFESORA GUÍA:
DRA. CLAUDIA CANNATELLI

MIEMBROS DE LA COMISIÓN:
DR. ÁNGELO CASTRUCCIO ÁLVAREZ
DR. JAMIE BUSCHER
DR. ÁLVARO AMIGO RAMOS
DRA. SARA FANARA

Este trabajo ha sido financiado por el Centro de Excelencia en Geotermia de Los Andes (CEGA) proyecto FONDAP-CONICYT #15090013 y parcialmente por el Programa de Estadías Cortas de Investigación Convocatoria 2019 del Departamento de Postgrado y Postítulo, Vicerrectoría de Investigación y Desarrollo, Universidad de Chile.

SANTIAGO DE CHILE
2019

RESUMEN

Los halógenos (Cl, F, Br, I) son un grupo de elementos que cumplen un rol fundamental en los sistemas volcánicos, junto con el agua, el CO_2 y el S, pertenecen a la fase volátil del magma. Ellos pueden modificar las propiedades físicas de los magmas tales como la densidad y la viscosidad directamente. La última erupción del Complejo Volcánico Lonquimay (CVL), que formó el cono Navidad, ocurrió en 1988-1990, emitiendo cantidades anómalamente altas de F hacia la atmósfera. Hasta 3000 ppm de flúor soluble fue medido en ceniza volcánica. Esta erupción ocasionó una gran mortalidad en el ganado bovino, ovino además de afectar a otras especies, debido a las altas concentraciones de F en pastos y forraje. Entre los volátiles, el agua es el más importante y un factor decisivo, junto con el CO_2, para entender el comportamiento de los sistemas magmáticos. Mundialmente, los volcanes asociados a zonas de subducción presentan un estrecho rango composicional de agua, alrededor del 4 wt.%. El CVL no presenta en la literatura mediciones directas del su contenido de volátiles, el contenido de agua ha sido solo estimado en base a geotermobarómetros. CVL se encuentra en la región de La Araucanía, Chile, sobre la traza más al norte de la zona de falla Liquiñe-Ofqui (ZFLO) in la zona volcánica sur (ZVS). CVL está compuesto por un estratocono principal (Lonquimay) y varios centros eruptivos y fisuras alineados NW-SE, este conjunto es conocido como el Cordón Fisural Oriental, aquí se emplaza el cono Navidad. Las inclusiones vítreas (IVs) son famosas por ser la mejor herramienta para conocer el contenido pre-eruptivo de volátiles y la composición parental de los magmas, dado que las IVs se comportan como sistemas cerrados. Las inclusiones vítreas son pequeñas gotas de magma atrapadas en irregularidades o fracturas de los cristales durante su crecimiento y pueden estar compuestas de burbujas, una parte vítrea, además de cristales heredados y/o hijos. Las IVs son la única forma de medir de forma directa la composición pre-eruptiva de los magmas. En esta tesis se estudió inclusiones vítreas con burbujas hospedadas en cristales de olivino para determinar el contenido total de volátiles de erupciones específicas del CVL. Por medio de análisis de microsonda electrónica, microsonda iónica y espectroscopía de Raman se determinó la composición de elementos mayores y trazas a dos lavas similares y contemporáneas, pertenecientes al estratocono Lonquimay y el cono Navidad. Los resultados muestran que los contenidos de F y Cl de IVs hospedadas en olivinos (Fo entre 80 y 50) son similares a magmas provenientes de zonas con arcos volcánicos. Las inclusiones vítreas del cono Navidad tienen mayores contenidos de F (200 a 1200 ppm) que las inclusiones vítreas del estratocono Lonquimay (200 a 600 ppm). Así mismo, los contenidos de Cl son similares entre las dos lavas (200 a 1200 ppm). La fuente más probable de los halógenos es el manto con contribuciones de fluidos provenientes de la corteza subductante. Adicionalmente, nuestros datos muestran que tanto las inclusiones de Navidad como de Lonquimay se encuentran empobrecidas en agua (0.1 a 0.25 wt.%). Las inclusiones de Lonquimay muestran que su magma parental pudo haber sufrido desgasificación de agua, lo que nos impide constreñir de forma precisa el contenido original de agua de su fuente. Por el contrario, las inclusiones vítreas del cono Navidad no muestran ninguna evidencia de una pérdida importante de agua, ni por desgasificación ni por pérdida asociada a difusión a través de los olivinos, sugiriendo que probablemente la fuente de los magmas del cono Navidad

son pobres en agua. Adicionalmente, las inclusiones de Navidad tienen composición de CO_2 que son típicas de sistemas sin desgasificación. Las tierras raras muestran una fuente común para los dos volcanes. Finalmente, un alzamiento del manto, debido a un contexto extensional local, bajo el CVL, pudo haber producido condiciones extraordinarias para que magmas pobres en agua ascendieran y alimentaran las erupciones tanto del estratocono Lonquimay y el cono Navidad.

SUMMARY

Halogens (F, Cl, Br, I) are a group of elements that are important in volcanic systems, and along with water, CO2 and S, they belong to the volatile phases of magmas. They can directly affect the physical properties of magmas such as density and viscosity. The last eruption of the Lonquimay Volcanic Complex (LVC), which formed the Navidad cone, occurred in 1988-1990, emitting anomalously high amounts of F into the atmosphere. Up to 3000 ppm of soluble fluorine was measured in volcanic ash. This eruption caused a great mortality in cattle, sheep and other animals due to an elevated F content in grass and forage. Among the volatiles, water is the most important one and is a key factor, with CO2, to understand the behavior of magmatic systems. Worldwide, subduction zone volcanoes have a narrow water composition range roughly 4 wt.%. No direct measurement of volatiles are available in the literature for the LVC, only water has been estimated through geothermobarometers.

LVC is in La Araucanía region in Chile above the northernmost trace of Liquiñe-Ofqui fault zone (LOFZ) in the Andean south volcanic zone (SVZ). LVC is made up of a main stratacone (Lonquimay) and several eruptive centers and fissures located NW-SE known as Cordón Fisural Oriental (CFO) where Navidad cone is placed.

Melt inclusions (MIs) are known as the best tool for estimating the pre-eruptive volatile content and parental composition of magmas since they can behave as a closed system encapsulating the magma. Melt inclusions are small droplets of magma trapped in either crystal irregularities or crystal fractures during growth, and may be composed of bubbles, glassy phases and daughter and/or inherited crystals. They are the only way to directly measure the pre-eruptive chemical composition of magmas (including volatiles).

In this thesis, we studied bubble-bearing olivine-hosted melt inclusions to determine the total volatile content for selected eruptions of the LVC. A determination of major and trace elements from two similar and contemporary lavas, one from the Lonquimay stratocone and the other from the Navidad cone, was done by Electron microprobe analysis, Secondary Ion Mass Spectrometry and and Raman spectroscopy.

Results show that F and Cl contents in melt inclusions hosted in olivine (Fo 80 to 50) are similar to those characteristic of magmas from arc volcanic settings. Navidad MIs have a higher F content (200 to 1200 ppm) than Lonquimay MIs (200 to 600 ppm) and similar Cl content between 200 to 1200 ppm for both lavas. The halogen source is most likely the underlying mantle with a contribution from the subducting slab.

Our data show there are water depleted MIs in both Navidad and Lonquimay (0.1 to 0.25 wt.%). Lonquimay MIs show that their parental magma may have suffered water degassing, preventing us to precisely constrain the original water content of its source. On the other hand, Navidad MIs do not show any evidence of strong water loss, neither by water degassing or water diffusion through olivine. Our results suggest that the Navidad magma source most likely was

water depleted. Additionally, Navidad MIs have CO2 contents that are typical of undegassed systems. Rare earth elements systematics for Lonquimay and Navidad MIs show a common magma source for the two volcanoes. A local mantle upwelling, due to the extensional tectonic setting of the LVC, may have produced an extraordinary condition for the ascent of a water depleted magma that fed the eruptions of Lonquimay and Navidad.

"… el cronista está más bien tentado de creer que dando demasiada importancia a las bellas acciones, se tributa un homenaje indirecto y poderoso al mal. Pues se da a entender de ese modo que las bellas acciones sólo tienen tanto valor porque son escasas y que la maldad y la indiferencia son motores mucho más frecuentes en los actos de los hombres. Ésta es una idea que el cronista no comparte. El mal que existe en el mundo proviene casi siempre de la ignorancia, y la buena voluntad sin clarividencia puede ocasionar tantos desastres como la maldad. Los hombres son más bien buenos que malos, y, a decir verdad, no es ésta la cuestión. Solo que ignoran, más o menos, y a esto se lo llama virtud o vicio, ya que el vicio más desesperado es el vicio de la ignorancia que cree saberlo todo y se autoriza entonces a matar. El alma del que mata es ciega y no hay verdadera bondad ni verdadero amor sin toda la clarividencia posible."

« … le narrateur est plutôt tenté de croire qu'en donnant trop d'importance aux belles, on rend finalement un hommage indirect et puissant au mal. Car on laisse supposer alors que ces belles actions n'ont tant de prix que parce qu'elles sont rares et que la méchanceté et l'indifférence sont des moteurs bien plus fréquents dans les actions des hommes. C'est là une idée que le narrateur ne partage pas. Le mal qui est dans le monde vient presque toujours de l'ignorance, et la bonne volonté peut faire autant de dégâts que la méchanceté, si elle n'est pas éclairée. Les hommes sont plutôt bons que mauvais et en vérité ce n'est pas la question. Mais ils ignorent plus ou moins, et c'est ce qu'on appelle vertu ou vice, le vice le plus désespérant étant celui de l'ignorance qui croit tout savoir et qui s'autorise alors à tuer. L'âme du meurtrier est aveugle et il n'y a pas de vraie bonté ni de bel amour sans toute la clairvoyance possible. »

- Albert Camus, La Peste (1947).

ACKNOWLEDGEMENTS

Esta tesis de magíster ha sido desarrollada y financiada gracias al proyecto FONDAP-CONICYT #15090013, Centro de Excelencia en Geotermia de los Andes, por medio de su investigadora Dra. Claudia Cannatelli, y su director, Dr. Diego Morata.

Agradezco al Departamento de Postgrado y Postítulo, VID, Universidad de Chile y su programa Estadías Cortas de Investigación Convocatoria 2019 por haber financiado la estadía del autor en Alemania y el Reino Unido que permitió el desarrollo de esta tesis.

Agradezco a la Dra. Claudia Cannatelli, primeramente, por haberme dado la oportunidad de realizar el programa de magister bajo su tutela. Además, le agradezco por enseñarme a trabajar con inclusiones vítreas, abrir caminos para avanzar en mi tesis, las retroalimentaciones que me dio, consejos sobre el futuro de mi carrera y, más importante, la confianza en el trabajo que estaba llevando.

Agradezco a la comisión de esta tesis Dr. Ángelo Castruccio, Dr. Jamie Buscher, Dr. Álvaro Amigo y Dra. Sara Fanara, por revisar cuidadosamente este trabajo entregando correcciones que la hicieron mejorar.

I thank Dr. Sara Fanara for receiving me in Germany, guiding me in this work, teaching me some methodology in lab, giving me advises and performing microprobe analysis and Raman spectroscopy. In the same way, I thank the whole group of Institute of Experimental and Applied Mineralogy, specially to Dr. Burkhard Schmidt, Frau Wolfrath, Dra. Graciela Sosa, Dr. Alfons M. van den Kerkhof and M.Sc. Max Schanofski. I also thank Dr. Cees-Jan De Hoog for receiving me in Scotland, and performing ion probe analysis at the Geosciences School, University of Edinburgh, United Kingdom.

Agradezco a Dr. Jamie Buscher por leer y revisar cuidadosamente esta tesis corrigiendo la ortografía y la gramática del escrito, además de aportar con su conocimiento y experiencia en el área de geología estructural. Agradezco también Dr. Diego Morata, Loreto Hernández, Roberto Valles, Pablo Molina, Javiera Véliz por ayudarme a desarrollar este trabajo, ya sea por medio conocimiento, ideas y/o trabajo. También agradezco a Maritza Acuña, Blanca Baccola, Bernardette Vázques y Karin Rojas por facilitarme el trabajo con la burocracia permitiéndome finalizar esta tesis.

Agradezco a mis amigos y padrinos Sergio y Rodo por escuchar mis quejas, compartir un té o un café, reírnos de los políticos, por darme ánimo con el estrés y todo lo que compartimos que hace más llevadera la vida. Agradezco a las personas con las que compartí mi vida especialmente al grupo de pregrado Sergio, Jupu y Paolo, además de Jacqui. También agradezco a la gente con que compartí una conversación en Geología, que me escucharon y que me compartieron sus vivencias.

Agradezco especialmente a Andrés Pica y Loreto CoX por creer cuando era muy difícil creer, a ustedes les debo mucho. Agradezco a mis tíos Manuel y Leticia por ayudarme cuando los necesité e interesarse por mi calidad de vida en la universidad. Agradezco a la tía Alicia por los consejos, los cafés, los sándwiches y los helados. Al tío Juan por los helados y los consejos. Agradezco a mis suegros (Jacqueline y Andrés) por interesarse por mí y estar dispuestos a

ayudarme siempre, además de permitirme estar con Jacquita jajaja.

Agradezco a mis padres y hermano, por apoyarme incondicionalmente, por creer incondicionalmente, por soportarme incondicionalmente. Gracias papá por enseñarme a soñar, gracias hermano por aguantarme, hacerme reír y traer al Cris al mundo jajaja. Gracias mamá por enseñarme que lo sueños se pueden cumplir con trabajo duro, a discernir entre lo importante y lo que no, por enseñarme lo importante que es la educación.

Finalmente, quiero agradecer a Jacqui, mi esposa. Gracias Jacquita por aguantarme en este proceso que ha sido largo y lleno de estres. Gracias por tus arrumacos, tus caricias, tus hummus, tus consejos, tus cariños, por creer en mí, por apoyarme, por siempre buscar el bien superior de nuestra relación. Gracias por soñar conmigo y hacerme soñar aunque quiera tener los pies en la tierra. Gracias las conversaciones sobre mi tesis y el fondo físico de fondo. Gracias por amarme incondicionalmente, sin ti, este trabajo hubiera sido mucho más pesado. Ik hou erg van jou.

CONTENTS

1

INTRODUCTION

1

1.1. INTRODUCTION

Halogens are present in the mantle and crust, although greater amounts are concentrated in the crust. Heavier halogens are more incompatible than lighter halogens, because of their atomic radii and charge-size ratios. Halogens are soluble in water, which strengthens their incompatible nature. Experiments focused on determining mineral, melt and fluid partition coefficients have shown a more incompatible behavior of chlorine than fluorine (Bernini et al. (2013)[6]), the latter behaving in some cases as a compatible element (Bernard et al. (2017)[5]). This behavior has a relevant role when magma undergoes different partitioning processes, such as degassing, fluid separation, melt crystallization, etc.

Halogens may also affect the physical properties of a melt. Experiments have highlighted an unequivocal decrease in viscosity with an increase in fluorine. Nonetheless, this effect is negligible when water is also present. Although water has the strongest effect, fluorine plays the role of further reducing the decrease in viscosity (Giordano et al. (2004)[31]), thus water-bearing magmas with smaller amounts of fluorine are less viscous. Experimental work by Dingwell (1993)[20]) have shown that an increase in fluorine produces a drop in density as well. The presence of chlorine has variable effects on viscosity. Depending on the magma composition, chlorine may increase or decrease viscosity. For instance, in a F-bearing melt, the addition of chlorine lowers the fluorine effect on viscosity (Webster et al. (2018))[90]. The role of halogens in magmas is very well constrained from models, such as the one proposed by Giordano et al. (2008)[32], which incorporates the effects of both water and fluorine.

Water is the most important volatile in a magma, as it reduces magma viscosity and density, which in turn drives magma ascent. Magma from volcanic arcs worldwide contains high water concentrations ranging from 2 to 6 wt.%, but 4 wt.% is most common (Plank et al. (2013)[66]). There are a few case studies in the literature reporting an anomalously low water content in volcanic arcs (Sisson et al. (1998)[78]), with the vast majority of them having low values due to water degassing or water loss (Lloyd et al. (2013)[50]). There are no studies reporting the amount of water directly measured in the magma from LVC, although Campos (2016)[11]) determined an amount of water of 1.58-2.1 wt.% for the source magma of Lonquimay based on an indirect estimation linked to mineral association and geothermobarometry.

A direct way to estimate the magma volatile content is through melt inclusions (MIs). MIs are small droplets of magma trapped inside a crystal during crystallization. They can contain glass, minerals and/or gas inside them (Roedder (1984)[72]). They can behave as time capsules, recording processes occurring in the magma from initial formation at mantle depths through the varying stages of magma chamber development (Cannatelli et al.(2016))[12]. Moreover, MIs may preserve the pre-eruptive physical and chemical conditions that took place during crystal growth (Cannatelli et al. (2016)[12]; Esposito et al. (2018)[26]). In the last decade, researchers reported that MIs are not a completely closed system. Post-entrapment modifications in MIs have been studied extensively and several authors have shown that a water loss can occur through diffusion of elements from the MI to the host crystal (Portnyagin et al. (2008)[68]; Hauri et al. (2002)[37]; Koleszar et al. (2009)[44]; Lloyd et al. (2013)[50]; Gaetani et al. (2012)[29]). Danyushevsky et al. (2000)[17] determined that olivine-hosted MIs experience Fe-loss associated with olivine crystallization on MI rims. Post-entrapment crystallization in MIs, therefore, modifies volatile content in the glassy phases, making the study of bubbles in MIs compulsory (Steele-

MacInnis et al. (2011)[81]; Moore et al. (2015)[54]). Taking this into account, several attempts have been made to correct these modifications based on REE content, studying bubbles and reconstructing the "theoretical" composition in equilibrium with the host (Steele-MacInnis et al. (2011)[81]; Danyushevsky et al. (2000)[17]; Lloyd et al. (2013)[50]; Hartley et al. (2015)[36]).

The Lonquimay volcanic complex (LVC) located at 38°22'30" S and 71°35' 30" W in the La Araucanía region, Chile, is part of the Andean Southern Volcanic Zone and extends along the northernmost trace of the Liquiñe-Ofqui Fault Zone (LOFZ). The LVC is composed of a main strata cone called Lonquimay and several adventitious eruptive centers and fissures aligned N60-70E known as Cordón Fisural Oriental (CFO) (Moreno and Gardeweg (1989)[55]). The LVC is an Upper Pleistocene-Holocene volcano and its last eruption was in A.D. 1989-90, emitting 0.23 km^3 of volcanic products, with the longest lava flow reaching up to 10.2 km (Naranjo et al. (1992)[57]). The eruption lasted for 13 months (Naranjo et al. (1992)[57]) and emitted a volcanic plume up to 9000 m high (Moreno and Gardeweg (1989)[55]). The rock types found at the LVC are basalts, andesites, intermediate andesites, silicic andesites, aphanitic dacites and micro-porphyritic dacites (Polanco (2010)[67]).

The last eruption that occurred in A.D. 1989-90 at the LVC is known as the Navidad eruption (VEI = 3). The eruption had a disastrous impact on the environment, as a high fluorine content of up to 3000 ppm had been measured in volcanic ash, as well as in grass, pastures and forage, causing great mortality of cattle, horses, sheep and a handful of dogs by osteofluorosis (González-Ferrán et al. (1989)[35]). The effects of the Navidad eruption lasted at least 2 years after the eruption ended (Araya et al. (1993)[3]). (1993)[3]).

Previous studies have shown that LVC rocks originated from the mantle, showing important contributions from the lower continental crust but little sediment contribution from the subducting slab compared to other Andean volcanic centers. A series of small magma chambers intertwined at different levels have been interpreted from geothermobarometric data in pyroxenes (Polanco (2010)[67]). Moreover, the LVC magmas are different than those of the Andean Southern Volcanic Zone because of their higher values of FeO^t and Na_2O and lower values of K_2O and MgO. Lavas from the southwest CFO volcanoes have been produced by more evolved magmas, similar to the Lonquimay stratocone, and northeast CFO products have a less evolved source of magma (Vergara (2010)[86]). Contreras (2013)[15] focused her study on the rheological properties of magmas that produced Navidad lavas, and her results show that the different lava flows during the eruption of Navidad were moving quite slow, which allowed microcrystals to crystallize during lava advancement. Gilbert et al. (2014)[30] focused their study on the LVC tephrostratigraphic record, determining that there was a longer repose time for eruptions before 6000 b2k ago, which was interpreted as a change in the magma storage and plumbing system of the LVC. Additionally, this record showed that there are three levels of magma storage, where eruptions triggered by the intermediate-depth chambers are restricted to older ages (>6000 b2k). The study of Robbiano (2017)[70] focused on the Navidad eruption, concentrating the analysis on olivine-hosted MIs. Results from this study show that MIs compositions are produced by the mixing of two end-member magmas, one that is trachyandesitic-basaltic and the other dacitic. These authors also studied the widespread fluor-apatite minerals crystallized in MIs and in the ground mass, showing that there was a high content of fluorine throughout the entire crystallization process of this magma.

1

1.2. OBJECTIVES

1.2.1. GENERAL AIM

The purpose of this study is to understand the origin of the anomalously high halogen and low water contents in the magmas erupted during the history of the Lonquimay volcanic complex, comparing the composition of olivine-hosted melt inclusions from two similar and contemporaneous lavas belonging to the Lonquimay stratocone and Navidad Cone.

1.2.2. SPECIFIC AIMS

In order to achieve the general objective, a series of specific objectives have to be fulfilled, which are listed below:

1. Determine the petrography and mineral/MIs relationship of the selected samples.
2. Determining the geochemistry of the bulk rock for the Lonquimay stratocone and Navidad cone.
3. Determining the major and trace elements composition of melt inclusions from the Lonquimay through Electron Microprobe and Ion Probe.
4. Determining the pre-eruptive volatile content of magma in the selected samples by Raman Spectroscopy and Ion Microprobe.

1.3. HYPOTHESIS

Volatile contents in magmas (H_2O, CO_2, Cl, F) can be quantified by studying melt inclusions, which record the geochemistry of the magma prior to its eruption. Olivine-hosted melt inclusion compositions are considered to be the best representations of the pristine geochemistry of the magma, as they record the melt when it forms in the mantle and the subsequent processes occurring during its evolution in the crust. By studying MIs for the Lonquimay stratocone and Navidad cone, we will be able to determine the mantle source of halogens and possibly anomalies, as well as the physical-chemical reasons for such a ”dry´´ magma.

2

MELT INCLUSIONS

2.1. INTRODUCTION

Melt inclusions (MIs) are small droplets of magma trapped inside a crystal that may consist of glass, minerals and/or gas. The MIs usually have a round shape, although it is possible to find irregular shaped ones, with sizes varying between 1 to 100 μm. Their importance resides on the fact that they could represent the original fluid/melt from which the host crystal was formed (Sorby (1958)[79]), i.e. in igneous minerals, inclusions may represent the composition of the original magma. Moreover, they can behave as a time capsule recording processes since formation at mantle depths to their evolution in magma chambers (Cannatelli et al.(2016))[12].

The phases observed in a MI strongly depend on size and cooling rate. As MI size decreases, the probability of MIs recrystallizing lowers, while a slow cooling rate favors the occurrence of recrystallized MIs (Cannatelli et al. (2016)[12]; Roedder (1984)[72]).

2.2. ROEDDER'S RULES

The study of MIs is based on three fundamentals assumptions known as Roedder's rules. They were defined and established by Roedder (1979)[71] and are based on the work of several authors, including Sorby (1958)[79], in igneous rocks. These rules were introduced to define a common methodology for everyone conducting a MIs study.

Each MI has to obey all three rules in order to be suitable for analysis, these rules are the following:

1. Melt inclusions were trapped as a single homogeneous phase.

2. Melt inclusions behaved as an isochoric system.

3. Melt inclusions were closed systems, i.e.nothing went in or out the melt inclusion.

2.3. TYPES OF MELT INCLUSIONS

Roedder (1984)[72]) defined three types of melt inclusions based on their trapping mechanism. These types were primary, pseudo-secondary and secondary melt inclusions.

- Primary MIs are trapped in crystals during their growth. Entrapment occurs in irregularities of crystals in the growth process (Roedder (1984)[72]).

- Pseudo-secondary MIs form when magma enters into a fracture of a crystal during its growth. Later fracture fill and heal while host crystal goes on growing (Roedder (1984)[72]).

- Secondary MIs are trapped in a healed fracture after crystal growth, i.e. they were trapped once the crystal has completely crystallized (Roedder (1984)[72]).

However, nowadays primary and pseudo secondary melt inclusions are both considered in the scientific community as primary MIs (Cannatelli et al. (2016)[12]).

2.4. POST ENTRAPMENT MODIFICATION

Although Roedder (1984)[72] considered MIs as a closed systems, subsequent studies have demonstrated that MIs do not always behave as closed system at all. Furthermore, "Fe-loss" and H_2O diffusion have been reported as possible processes ocurring after the formation of MIs (Danyushevsky et al. (2000)[17]; Gaetani et al. (2012)[29]; Moore et al. (2015)[54]). These processes, known as post entrapment modifications (PEMs) or post entrapment crystallization (PEC) of a MI, are summarized in the following paragraphs.

2.4.1. GENERATION OF BUBBLES

Some MIs have inherited bubble since the presence of a pre-existing bubble which shows the volatile-saturated state of the magma prior the entrapment. The MIs trapped an extra amount of volatile which not resemble the exact content into the melt. Moreover, this process is not a PEC. On the other hand, when the magma is trapped as a single homogeneous phase a bubble may be formed as a PEC. Although most melt inclusions have the potential to form bubbles, not all MI have them when they are observed at room room temperature. Sometimes MIs contain a bubble as a result of slow cooling, leakage or decrepitation of the host crystal. In some cases, a bubble never forms inside a MI because certain factors can prevent bubble nucleation. For instance, a tiny MI does not have enough surface volume to enhance a heterogeneous nucleation. Likewise, smaller MIs have fewer atoms, so the likelihood of homogeneous nucleation decreases. Additionally, the internal pressure increases as the MI ratio decreases, so smaller MIs have a higher probability of nucleating bubbles (Roedder (1979)[71]).

On the other hand, a homogeneous melt may form bubbles after entrapment which is a natural process as PTXV conditions vary. These bubbles are known as shrinking bubbles and are the result of the host crystal and melt inclusion cooling process. Then, a decrease of temperature and pressures provoke a solubility decrease of volatiles originating bubbles (Moore et al. (2015)[54]).

2.4.2. POST ENTRAPMENT CRYSTALLIZATION

One of the simplest way MI are modified is a crystallization of a single phase on the MIs' wall. This phenomenon, known post entrapment crystallization (PEC), may occur inside magmatic chamber, during the magma ascent as well as on Earth's surface (Steele-MacInnis et al. (2011)[81]). If this process occurred, it may head a compositional change of MIs. For instance, Danyushevsky et al. (2000)[17] reported modification of MIs caused by olivine crystallization on MIs' walls. An olivine host with a higher #Mg than the hosted MIs, allows to crystallize smaller-#Mg olivine on the MIs' wall. Eventually, the new mew crystallized olivine will adjust its Fo content with olivine host. This process triggers the movement of Fe^{2+} from the daughter olivine to the host olivine, leading researchers to consider erroneous Fe-poorer MIs. This process is known as **"Fe-loss"** (Danyushevsky et a. (2000)[17]) and olivine with higher Fo content is subject to a higher modification/loss of Fe in their hosted MIs.

Another PEC consequence is the formation of a shrinkage bubble caused by the crystallization of minerals from MI melt phase. During the post entrapment crystallization, a small increase in water solubility and slightly decrease of CO_2 solubility can occur in the melt. This process pro-

duces a CO_2-richer bubble and a water-rich melt compared to MI without PEC (Steele-MacInnis et al. (2011)[81]).

2.4.3. WATER DIFFUSION

Another important post entrapment modification, caused by the rapid diffusion of water, is the absence of a closed system behavior between MI and the host mineral (Gaetani et al. (2012)[29]). This rapid diffusion led several researcher to assess the reliability of water in MIs (Hauri (2002)[37]; Cannatelli et al. (2016)[12]). A handful of researchers have tried to estimate the amount of water diffused and their results reached up to 4 wt.% of water loss (Koleszar et al. (2009)[44]; Lloyd et al. (2013)[50]; Hartley et al. (2015)[36]). Water can diffuse through olivine its host by means of an exchange of protons between melt inclusion and the olivine host. The proton exchange may be generated by either the reduction or oxidation of Fe on a octahedral lattice site and either creation or destruction of 2 OH^- defects linked to an octahedral site metal vacancy (Gaetani et al. (2012)[29]).

2.5. MELT INCLUSION ASSEMBLAGE

Fluid inclusionist had intensively worked in fluid inclusions (FIs) to determine correctly the composition of the original fluid. Goldstein and Reynolds (1994)[33] defined ***fluid inclusion assemblage*** **(FIA)** as a "*the most finely discriminated, petrographically distinguishable group of fluid inclusions*". Additionally, FIs in a FIA must share the volumetric proportion of vapor/liquid phase. In other words, they must be trapped at the same "time", i.e. they share the same conditions of entrapment (pressure, temperature, fO2, etc.).

Acknowledging above mention study, Bodnar and Student (2006)[8] defined ***melt inclusion assemblage*** **(MIA)** as a "*group of melt inclusions trapped at (essentially) the same time and, by analogy, at the same temperature and pressure, and from a melt of the same composition*" because similar petrographically techniques should be used to identify melt inclusions[8].

However, testing conditions to prove whether a melt inclusion belongs to a MIA is difficult. Thus, Bodnar and Student (2006)[8] proposed a method similar to FIA for MIs: if all the inclusions have the same number of phases, in the same volume proportions when observed at room temperature, and if the temperatures of phase changes are the same in all of assemblage. It indicates that the all inclusions have the same composition. Crystallized melt inclusions must be homogenized and analyzed, by means of analytic techniques, to determine if all of the inclusions in MIA have the same composition and phase behavior during heating.

2.6. DETERMINING VOLATILE CONTENTS

Many researches have calculated CO_2 content in melt inclusions (Moore et al. (2015)[54]; Esposito et al. (2011)[25]; Steele-Macinnis et al.(2011)[81]) through Raman spectroscopy. Because Kawakami et al. (2003)[40] developed a reliable way to obtain CO_2 density. Subsequently, Fall et al. (2011)[27] and Lamadrid et al. (2017)[47] have made modifications of the previous models.

The method is based on a separation between two Raman bands of CO_2 due to Fermi resonance.

CO_2 is a three-atomic molecule which presents four vibrations modes: a symmetric stretching mode ν_1 an antisymmetric stretching mode (ν_3) and two degenerate bending modes (ν_{2a} and ν_{2b}). However, energies belonging to degenerate modes and the symmetric stretching mode overlap themselves. Hence, CO_2 spectra only shows two strong lines whose frequencies are 1388.2 cm^{-1} (ν_+) and 1285.4 cm^{-1} (ν_-) (figure 2.1).

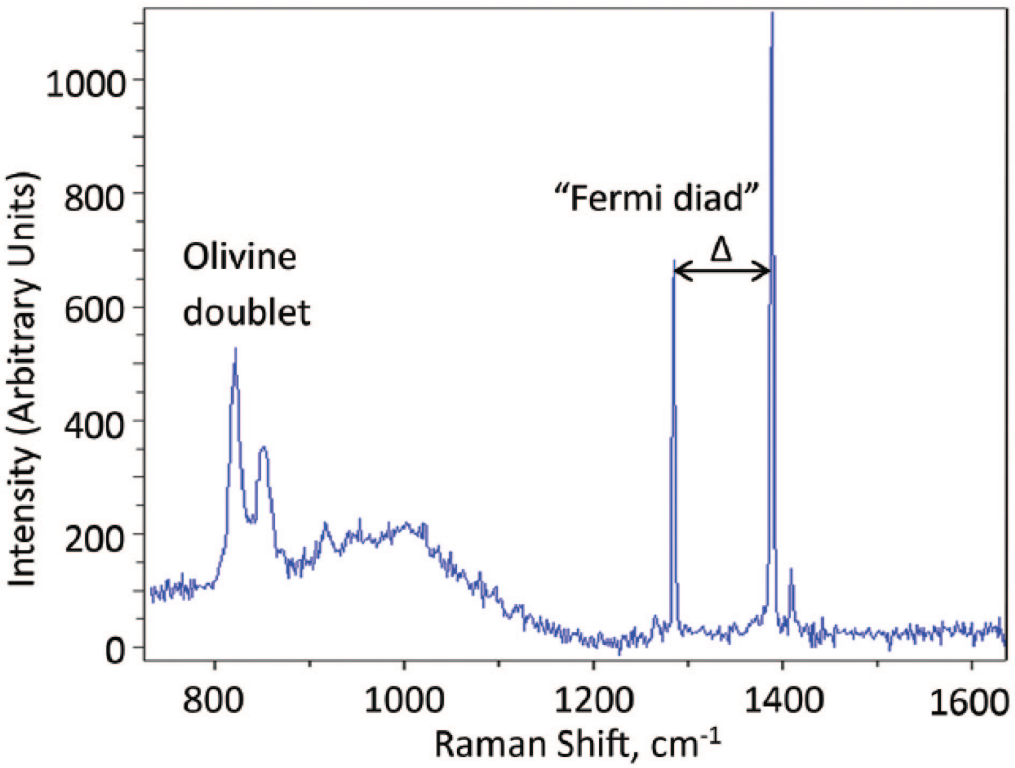

Figure 2.1: Raman spectrum of a vapor bubble in an olivine-hosted melt inclusion belonging to Fuego volcano. Peaks are from olivine doublet, ν_+ and ν_-. The difference between ν_+ and ν_-, in units of cm^{-1}, is known as Fermi diad "$\triangle$". CO_2 density is proportional to $\triangle$. Modified from Moore, et al. (2015)[54].

Regarding state equations of CO_2, Fall, et al. (2011)[27] measured pressure of bubble in melt inclusions. Thus an empiric relation was made depending on CO_2 density and Fermi diad ($\triangle$). Regression analysis generated the following equation of the Fermi diad for CO_2:

$$\rho CO_2 = -0.030314551\triangle^3 + 9.432834797\triangle^2 - 977.9384933\triangle + 33780.38242 \quad (2.1)$$

Likewise, Lamadrid et al. (2017)[47] modified this equation generating the following equation (equation 2.2):

$$\rho CO_2 = -36.42055 + (0.354812\triangle) \quad (2.2)$$

where ρCO_2 is measured in g/cm^3 and $\triangle$ in cm^{-1}.

Once ρCO_2 is determined, it is assumed that the bubble has a spherical shape, then, the volume is known based on bubble radio measurements.

$$V_{bubble} = \frac{4}{3}\pi r^3 \tag{2.3}$$

The CO_2 mass is obtained from definition of density $\rho = \frac{m}{V}$ and equations 2.1 and 2.3.

$$m = \frac{4}{3}\rho CO_2 \pi r^3 \tag{2.4}$$

Finally, CO_2 moles (n_{CO_2}) are obtained from the relation $n = \frac{m}{PA_{CO_2}}$.

Bubble-bearing melt inclusions may contain from 40% to 90% of the bulk content of CO_2 inside the bubble. Processes reported by researchers (Wallace, et al. (2015)[88] and Esposito et al. (2011)[25]) showed melt inclusions can lose CO_2 to shrinkage bubble, due to post entrapment crystallization processes which create a pressure drop into the bubble contributing to the lost (Steele-MacInnis et al. (2011)[81]).

Regarding CO_2 content in the glass phase of a MI, SIMS (Secondary Ion Mass Spectrometer) provides CO_2 concentrations in ppm. Hence, it is necessary to divide concentration by CO_2 atomic weight, and to use a magma model density. For instance, in our study we used the model proposed by Bottingan and Weill (1970)[9] with volume and thermal expansion from Lange and Charmichael (1987)[48] and compressibility from Kress and Charmichael (1991)[46]. Therefore, the total CO_2 content in MIs is obtained by adding CO_2 moles from the bubble (gas) phase and the glass (solid) phase.

3

GEOLOGICAL BACKGROUND

3.1. SOUTHERN VOLCANIC ZONE

Chile has almost 90 active volcanoes, with the most active volcanoes in the Southern Andean Volcanic Zone (SVZ) and the Central Andean Volcanic Zone (CVZ). Lonquimay volcano, or Lonquimay volcanic complex (LVC), is the 15th-most-dangerous volcano in Chile according to the ranking of Chilean active volcanoes by SERNAGEOMIN and is located in the SVZ.

The SVZ has been created from the collision between the Nazca and South American plates (figure 3.1). The SVZ extends from 33°S to 45°S and has first-order features that control the magma behavior and composition, including the crustal thickness and the Liquiñe-Ofqui fault zone (LOFZ) (Cembrano and Lara (2009)[13]. The crustal thickness varies from 35 km to 50 km along the strike of the southern Andes (Hildreth and Moorbath (1988)[39]; Cembrano and Lara (2009)[13]) but the thickness is around 35 km at the latitude of Lonquimay,. The second main feature, the LOFZ (figure 3.1) is a 1.2km-long intra-arc strike-slip fault system that has been active over the last 6 Ma (Pérez-Flores et al. (2017)[64]; Cembrano et al. (2009)[13]). The LOFZ is a transpressional fault zone dominated by dextral to dextral-reverse slip along subvertical NNE-striking faults, as well as dextral-normal slip along NE-ENE-striking faults and NE-striking extensional fractures (Pérez-Flores et al. (2017)b[65]; Lavenu et al. (1999)[49]; Cembrano and Lara (2009)[13]).

3.2. STRATIFIED ROCKS

3.2.1. CURA-MALLÍN FORMATION

Lower - Middle Miocene

The Cura-Mallín formation is made up of andesitic to rhyolitic volcanic rocks, lacustral rocks, and a small quantity of fluvial sedimentary rocks. The formation was first defined by González and Vergara (1962)[34] and modified by Suarez and Emparán (1997)[82], and was named after the gully in the north of Curacautín. It overlays discordantly the Eocene Malla-Malla formation and underlies rocks from Trapa-Trapa Formation. The formations is composed by two continental members: Guapitrío and Rio Pedregoso in Hoja Cuaracautín.

The Guapitrío member is a volcanic succession, with intermediate to acid composition, consisting mainly of pyroclastic and lava rocks interbedded with continental sediments. The pyroclastic succession is made up of green to brown vitric and lithic tuffs representing fall deposits and pyroclastic density current deposits. The sedimentary layers are primarily cross-stratified fluvial sandstones and layer lutites. Lavas are 200 m-thick andesites (Suarez and Emparán (1997)[82]).

The Rio Pedregoso member is made up of a combination of fluvial, deltaic and lacustral facies. The lacustral facies are composed of stratified layers and abundant lacustral fauna such as fish, ostracods and mollusks. The deltaic association has several features which has been divided based on the grain size, the layer thickness as well as the presence of frontal bended deltaic caps of megaforesets made up of gravitational and pyroclastic fluxes. (Suarez and Emparán (1997)[82]).

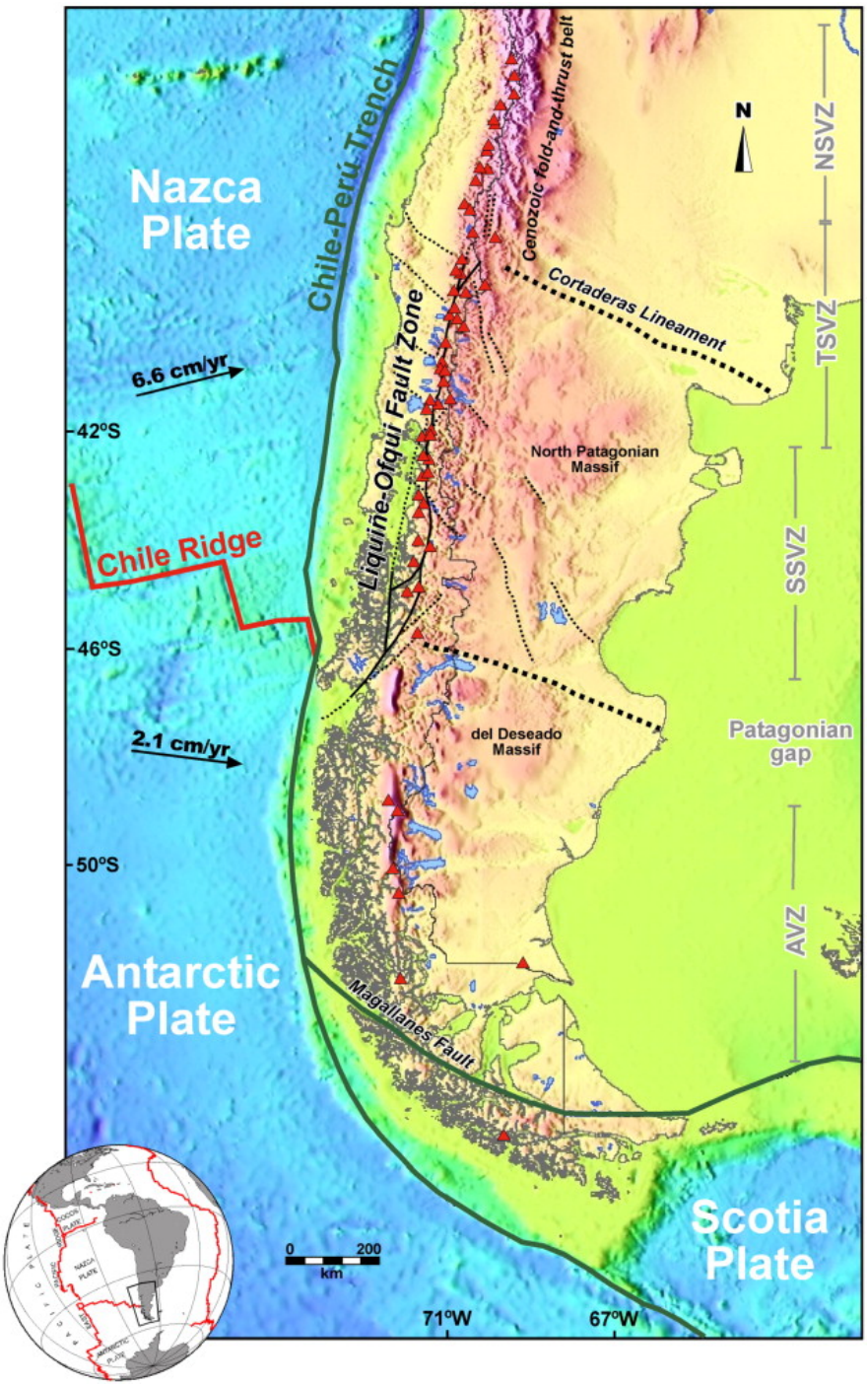

Figure 3.1: The Andean Southern Volcanic Zone (SVZ) extends from 33°S to the area of collision between the Chile ridge and the South American plate. The Liquiñe-Ofqui fault zone is an intra-arc transpressional fault zone that is aligned with volcanoes of the SVZ. Modified from Cembrano and Lara (2009)[13].

3.2.2. MITRAUQUÉN FORMATION

Upper Miocene

The Mitrauquén formation was first defined by Suarez and Emparán (1997)[82] as a unit composed of conglomerates, ignimbrites and andesitic lavas. The formation outcrops between Mitrauquén and Licura rivers east of the Bio-Bio river. Additionally, it overlays the Cura-Mallín formation with an unknown contact. In the south valley of the Mitrauquén river, it underlays Pliocene lavas. The Mitrauquén formation has two members: the first one is a sedimentary member consisting mainly of conglomerates interbedded with dacitic ingnimbrites and andesitic lavas. The second member is made up of andesitic lavas and tuffs.

3.2.3. MALLECO FORMATION

Pliocene - Lower Pleistocene

The Malleco formation overlies the Vizcacha-Cumilao and Cura-Mallín formations and Huichaue strata along an angular unconformity, and granitoids from the Meli-Peuco plutonic group along an non-conformity. Additionally, the formation underlies the lavas from Conjunto de Volcanes de la Cordillera Principal. The Malleco formation is mainly made up of volcanic rocks interbedded in places with continental sedimentary layers. It has four units: the **Lower Unit** is composed of volcanic breccia, agglutinates, lapili and vitric tuff, diamictites, paraconglomerates, conglomerates and sandstones. The **Middle Unit** consists of interbeds of basaltic andesitic lavas and volcanoclastic rocks. The **Upper Unit** consists of andesitic basaltic lava, with olivine a trace amount of volcanoclastic layers. The **fourth unit** is an assemblage of isolated andesitic basaltic volcanic outcrops or lavas located adjacent to the volcanic centers (Suarez and Emparán (1997)[82]).

3.2.4. CONJUNTO DE VOLCANES DE LA CORDILLERA PRINCIPAL

Quaternary

This group of volcanoes has been defined by Suarez and Emparán (1997)[82] as an assemblage of five volcanoes, with one inactive and four active volcanoes. The group of volcanoes extend from south to north and are named as the following: Sollipulli, Llaima, Sierra Nevada, Lonquimay (Lonquimay volcanic complex; LVC) and Tolhuaca.

SOLIPULLI VOLCANO

Solipulli volcano is located at 38° 59’ S and 71° 31’ W in the Cordillera Principal in the La Araucanía region. Sollipulli volcano is made up mainly of an eroded collapse caldera and a younger caldera volcano. On the south, there are several lava domes and to the east there are four blast craters, eight parasitic pyroclastic cones and some andesitic-basaltic lavas. Sollipulli volcano had a Plinean eruption roughly 2900 years ago and its last eruption occurred in A.D. 1240 ± 60, which generated the Chufquén cone.

LLAIMA VOLCANO

Llaima volcano is located at 38° 41’ 30" S and 71° 44’ W in the La Araucanía region of Chile. Llaima volcano is one of the most voluminous volcanoes in Chile with a volume of roughly 400

m^3. It is a mixed volcano, between composite and shield volcanoes, with an 8 km-diameter buried caldera. It is surrounded by 40 adventitious cones as well as fissures (Naranjo and Moreno (1991)[58]; Suarez and Emparán (1997)[82]). Llaima volcano has evolved following four main construction periods. It began with Llaima I, when the first volcanic construction began, with the 8km-diameter caldera forming at the final stage of this episode. The second stage, called Llaima II, began with the Curacautín ignimbrite, marking a more explosive period. In this stage, a $4km^3$-Plinean eruption was generated. Llaima III began with a new effusive stage, mainly composed of basaltic andesites and basalts, which created the mixed volcano. After this stage, the adventitious cones formed with a composition that was slightly more silicic than the main cone (Naranjo and Moreno (1991)[58]; Suarez and Emparán (1997)[82]).

TOLHUACA VOLCANO

Tolhuaca volcano is located at 38° 18' S and 71° 39' W in the La Araucanía region in Chile. It is a mixed strata volcano of lavas and pyroclasts. The summit is aligned NW-SE with the Lonquimay main volcano and several parasite craters to the northwest unveiling magmatic migration. The last evidence of volcanic activity are a 2km-long fissure and a pyroclastic cone. Tolhuaca has had intense erosion by glaciers. It is not certain when the last eruption occurred and current activity consists of only geothermal activity, such as solfatara areas with fumaroles, boiling pools and hot springs (Suarez and Emparán (1997); Sánchez-Alfaro (2016)[77]).

SIERRA NEVADA VOLCANO

Sierra Nevada volcano is an extinct stratovolcano that has been eroded for at least two Pleistocene glacial periods (Thiele et al. (1987)[83]; Suarez and Emparán (1997)[82]).

3.3. LONQUIMAY VOLCANIC COMPLEX

Lonquimay volcanic complex (LVC) (figure 3.2) is located in the Andes Cordillera at 38°22'30" S and 71°35' 30" W in the La Araucanía region, Chile. Its main cone has a summit elevation of 2865 m a.s.l. LVC is composed of a main cone known as Lonquimay stratocone and several smaller adventitious centers aligned northeastward along a fissure known as Cordón Fissural Oriental (CFO) (Suarez and Emparán (1997)[82]; Moreno and Gardeweg (1989)[55] and cites therein).

Lonquimay stratocone (Lonquimay) is a smaller stratovolcano with a *"truncated shape"*, which is enlarged to the WSW-ESE and consists of pyroclastic material and lavas. Lonquimay has a roughly circular 8.5km-diameter base and a 700m-diameter elliptical crater. There are three 150-to-250m-diameter secondary craters along the northern flank, one 300m-diameter crater on the WSW boundary and minor craters linked to fissures on the southwest and eastern flanks. Numerous eruptive centers form a small pyroclastic area aligned WSW-ENE along a 2km-long fissure. Also, only the southern boundary has evidence for glacial erosion (Moreno and Gardeweg (1989)[55]).

Cordón Fissural Oriental (CFO) is made up of a few craters, smaller than 1km-long fissures, pyroclastic cones and domes built upon almost horizontally stratified sequences of lavas, breccia and agglutinates affected by glacial erosion. CFO is covered by a thick pyroclastic blanket of bombs, smaller blocks, scoria and pumice (Moreno and Gardeweg (1989)[55]). The CFO includes the

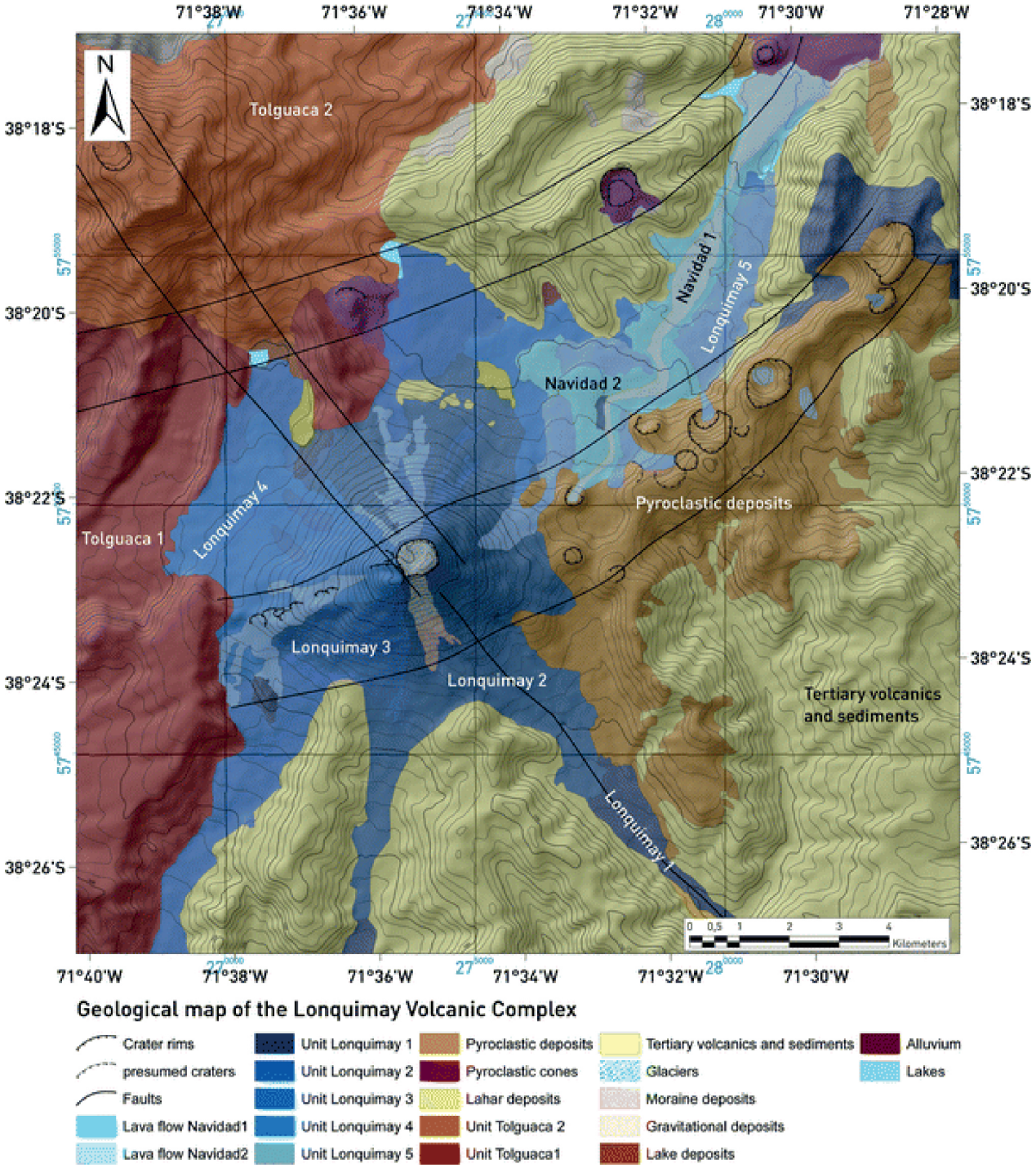

Figure 3.2: Geologic map of Lonquimay Volcanic Complex (LVC), showing geological units of Lonquimay stratocone and Navidad cone. Modified from Gilbert et al. (2014)[30] and Moreno et al. (1989)[55].

Navidad cone over one fissure trace (Naranjo et al. (1991)[58]).

Lonquimay is a Holocene volcano with historic activity in 1853, 1887-1890, 1933, 1936, 1940 and 1988-1990 (Gilbert et al. (2014)[30]; Moreno and Gardeweg (1989)[55]). Based on stratigraphic analysis, there have been 27 post-glacial eruptions including historic ones over the last ~ 12000 years (Gilbert et al. (2014)[30]). The last eruption occurred between 1989-1990, forming the Navidad cone (Moreno and Gardeweg (1989)[55]; Naranjo et al. (1991)[58]; Naranjo et al. (1992)[57]).

Lonquimay eruptive activity has been divided into four stages based on lavas that represent several hawaiian and strombolian eruptions (Polanco (2010)[67]). Classification based on stratigraphic succession reveals three sequences of explosive eruptions (Gilbert et al. (2014)[30]). Three different compositional differences are revealed, which authors link to differences in chamber depth and temperatures. The authors infer a shallow chamber for the most evolved composition, a deeper chamber for more primitive composition and one at intermediate levels for intermediate compositions (Gilbert et al.(2014)[30]).

The LVC is formed by basalts, andesites, intermediate andesites, silicic andesites, aphanitic dacites or micro porphyritic dacites. The have few crystals, mainly plagioclases but it is possible to find olivine, clinopyroxenes and opaque minerals. There is a slight trend to increase silicity in LVC. Oldest units have more primitive composition without dacite and youngest units have more evolved composition without basalts. LVC has SVZ geochemistry with a great range of silicic content where CFO has the highest silicic content (Moreno and Gardeweg (1989)[55]).

The last eruption formed Navidad Cone during the 1988-1990 eruptive cycle. The eruption began in a 400m-long fissure with four distinguishable craters. This eruptive cycle had several phases. The first phase was phreatomagmatic that occurred predominantly during the beginning of the eruption. A strombolian phase followed and then a vulcanian phase started after the second half of the eruptive cycle. The vulcanian phase was the most hazardous of the phases, producing a 9 km-high volcanic plume (Naranjo et al. (1991)[58]). The Navidad lavas contain olivine, plagioclase, clinopyroxene, magnetite and sometimes ilmenite, with some pyrite associated with the ilmenite found. Lava composition is almost exclusively andesite (57.8 wt.% - 59.1 wt.%) that has remained invariable with time. Although Navidad lavas are considered to have a LVC composition, the lavas are less evolved compared to the previous eruptive cycle (Moreno and Gardeweg (1989)[55]). An spotlighting phenomenon occurred durig and after the last eruption due to Araya et al. (1990)[2] and Araya et al. (1993)[3] reported fluorosis in cattle showing high fluorine concentration in grass and cattle up to ten month after the Navidad eruption finished. Furthermore, fluorine soluble concentrations measured in eruption ash reached 3000 ppm in samples (González-Ferrán et al. (1989)[35]) although one study denies abnormal fluorine concentration in soils and pastures (Besoaín et al. (1992)[7]).

At LVC, there is a transfer zone that connects the northern Lolca fault with the southern Malalcahuello fault (Pérez-Flores et al. (2016)[63]). Tolhuaca volcano is located on a NNE-striking master fault close to a releasing bend defined by NE-striking faults at the Lonquimay volcano (figure 3.3), which have documented extensional behavior (Pérez-Flores et al. (2016)[63]; Pérez-Flores et al. (2017)[64]).

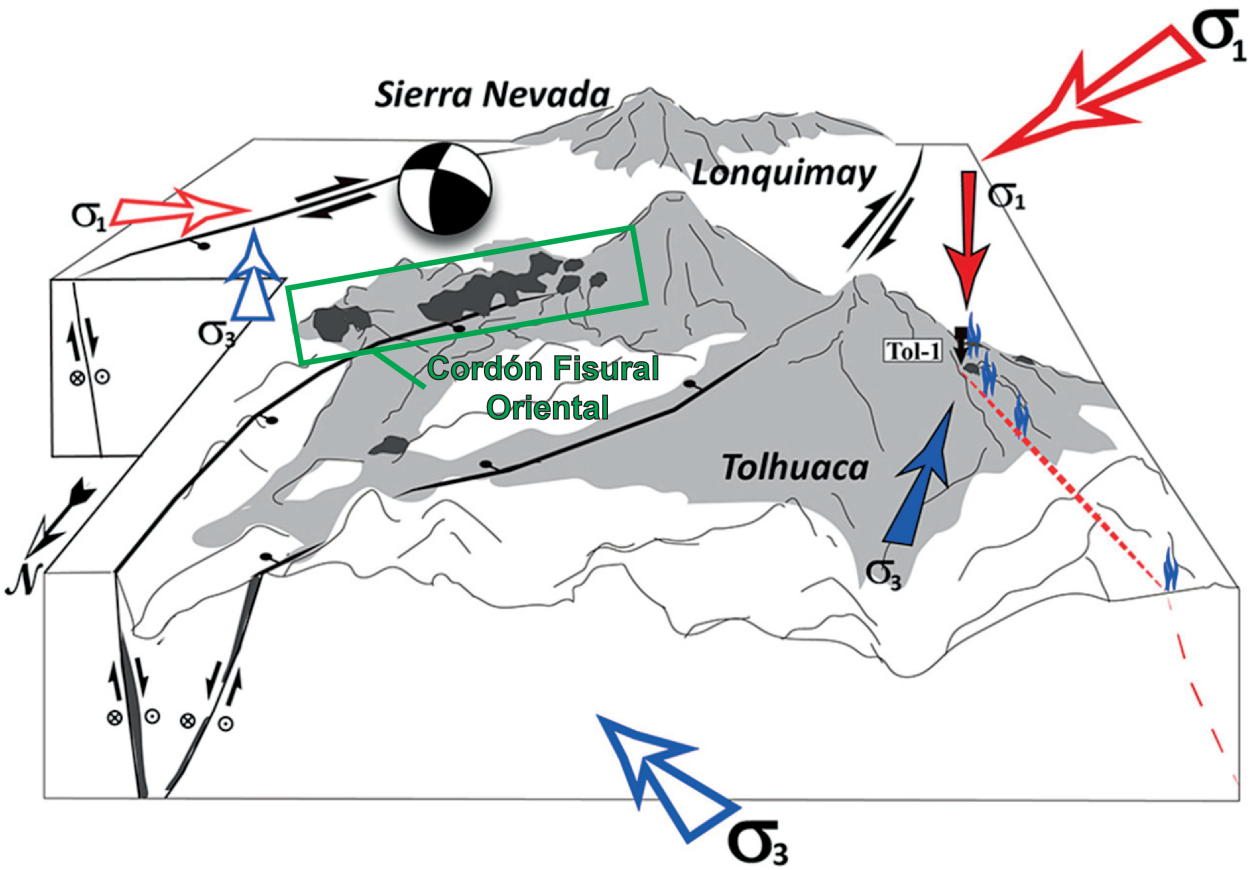

Figure 3.3: Northernmost trace of the Liquiñe-Ofqui fault zone at the LVC, with subvertical NNE-trending strike-slip faults along Lonquimay, Cordon Fissural Oriental (CFO) and Tolhuaca volcano. The behavior of this fault zone is extensional. Small red and blue arrows indicate the maximum local stresses, while the large red and blue arrows show the regional distribution of forces. Navidad cone is located in the CFO. Modified from Perez-Flores et al. (2017)[64].

4

METHODOLOGY

4.1. SAMPLES

Samples used in this research consist of four lavas, with three belonging to the Navidad eruption (NV18, NV19, NV24) and one from the Lonquimay stratocone (H4). Navidad lavas are porphyritic andesite with plagioclase, olivine and clinopyroxene, in order of abundance. In contrast, Lonquimay lava is a porphyritic andesite with plagioclase as the main phenocrystal, with crystals smaller in size with respect to Navidad.

4.2. MINERAL SEPARATION

Mineral separation was performed at the **"Laboratorio de Preparación de Muestras"** in the Department of Geology at the University of Chile. The following paragraphs describe the procedure used to prepare the samples from both volcanoes.

The first step was to obtain phenocrystals from the rock. In order to achieve this, it was necessary to reduce the rock volume using tools such as a hammer and an anvil; the latter gave a hard surface to hold the rock. However, to avoid metal contamination, the anvil and hammer surfaces were covered by a strong piece of cloth. The rock was hammered until its fragments had a size below 5 cm. An agate mortar and a pestle were then used to further reduce the size of rock fragment and to grind them. When the fragments reached sand-grain sizes, we used 1 mm and 0.031 mm plastic sieves to separate mineral grains.

The succeeding reduction had the aim of releasing crystals of its fundamental mass. For this, agate mortar and pestle were used as tools. It was set into mortar a few rock fragment, then, bigger fragments were hit with pestle until they reached pebble size. After that, pestle was used to grind pebble moving its surface onto mortar. This process stopped when fragment had sand range size. Finally, the sand-size rock fragments were sifted onto 1mm-aperture and 0.031mm-aperture plastic sieves. The useful sifted grains were those that were trapped by the 0.031mm-aperture plastic sieve. This process was repeated until a considerable amount of grains was obtained.

The last step involved the cleaning of the rock fragments in order to select the most suitable crystals. Sifted rock fragments were put into a glass beaker, and then, ethanol was poured into the beaker. We did not use water in this process to avoid filling mineral fractures with water that could lead to the artificial generation of fluid inclusions. The beaker was put into an ultrasonic washer for three minutes, and then the grains were dried under an infrared light for one hour.

4.3. MINERAL SELECTION

We used a binocular stereomicroscope to select the largest and most transparent crystals for this study, as they most likely contain easily observable melt inclusions. Crystals were handpicked by either tweezers or a 0-number pencil, classified regarding their mineral phases and then stored in different small plastic containers. Picked crystals were then mounted in epoxy and polished to perform petrographic descriptions.

4.4. EPOXY HOLDER CONSTRUCTION

Once enough crystals were handpicked, they were mounted in suitable holders based on the ratio between the groundmass and crystals. Epoxy was made by a combination between Epoxy resine and hardener in a 7:1 proportion.

4.4.1. 25MM-DIAMETER HOLDER

Crystals were mounted with Epoxy resin in a 25mm-diameter holder (figure 4.1 a) when their transparency was enough to allow the passage of light, i.e. when the ratio of groundmass and crystals was small and it was possible to observe melt inclusions. A holder mold is composed of a 25mm cylindrical part and a 25mm circular flat-face part. On the circular flat-face part, we put double-sided tape and on top of it we put several crystals along with their groundmasses. The cylindrical-mold part was then joined to the crystal-bearing part and Epoxy was poured into the mold to cover the crystals (5 cm-thick layer). Finally, the mold was put in a non-mobile flat surface, and once it was dried, the mold was removed from the Epoxy holder.

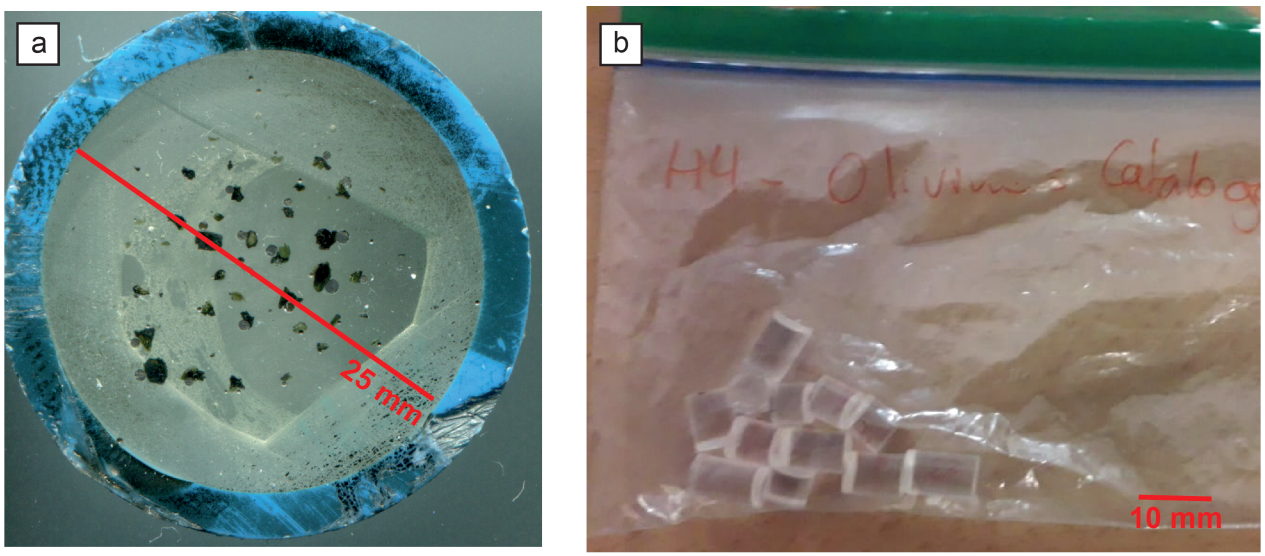

Figure 4.1: a) 25mm-diameter holder with crystal on surface and b) Straw holder inside a bag.

4.4.2. STRAW HOLDER

Crystals with little transparency, a high groundmass-to-crystal ratio and/or few melt inclusions were mounted in straw holders singularly, following a similar procedure to the one described above. We used double-sided tape, on which we put the mold with 7 plastic straw pieces, marking its perimeter. The straws, cylindrical mold and mineral-bearing mold parts were then joined, and epoxy was poured into every straw, covering crystals with a layer of about 5 cm-thick. This mixture did not remain in the straws, it flowed outward from the straw, and remained in the mold. Finally, the mold was put in a non-mobile flat surface, and once it was dried, the mold and all of the single-straw holders were taken apart, with single-straw holders (figure 4.1 b) having either single grains or crystals.

4.4.3. MICROPROBE AND IONPROBE HOLDERS

Crystals mounted in straw Epoxy holders were polished until homogeneous melt inclusions were exposed at the surface. Following a similar procedure, bubble-bearing melt inclusions, already analyzed by Raman, were also polished until the glassy phase was exposed. This was performed using 0.5μm-aluminum powder. Straw holders were then put into a 25 mm-diameter metal cylinder with four circular holes, glued with an UV-superglue and a thin layer of epoxy on the cylinder base (figure 4.2). Before analysis, holders were coated with either carbon or gold depending on the electron/ion microprobe requirements. It is important to highlight that this procedure was also useful for observing samples and melt inclusions with SEM images.

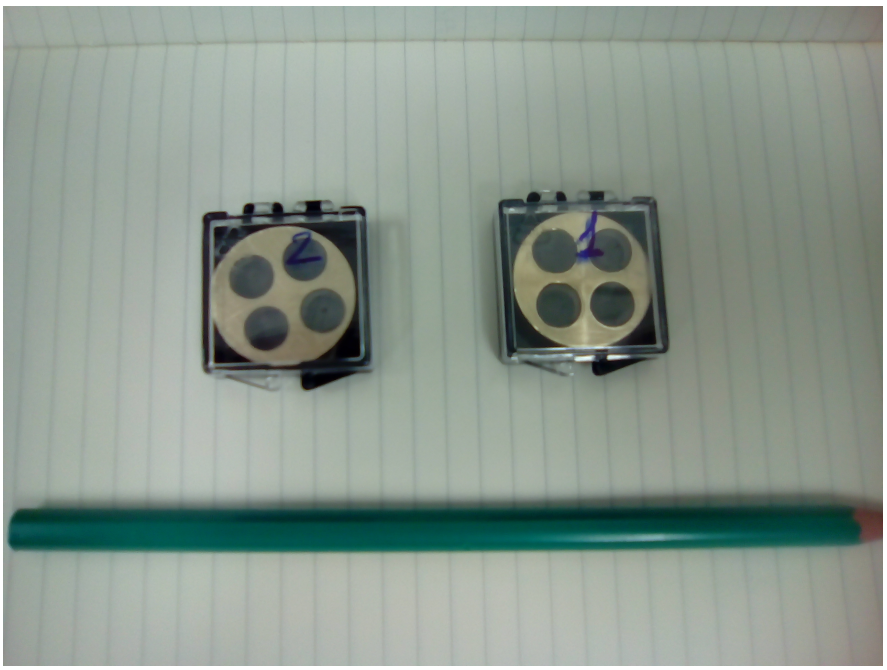

Figure 4.2: Metal holders used to mount melt inclusion-bearing crystals. Each epoxy-made straw containing single crystals were mounted inside the 25 mm-diameter holder (7 straws for each metal holder).

4.5. POLISHING

The polishing step was conducted at the **"Laboratorio de Inclusiones Fluidas y Vítreas"** in the Department of Geology at the University of Chile and in the **Institute of Mineralogy** at the University of Göttingen in Germany.

Once the epoxy mounts were dried, they were first polished on the base of the 25 mm-diameter holder and then on the other side. We used 180-grit sandpaper and milli-q water until every crystal face appeared on the surface and the double-sided tape completely disappeared. After that, the holder was cleaned inside a beaker filled with ethanol that was put into an ultrasonic cleaner for 3 minutes. The sandpaper was changed every 5 to 6 minutes of polishing, from 180 to 5000 grit sandpaper. For every change of sandpaper, the cleaning process was repeated. In addition, before starting the next polishing step, the holder was put under a microscope to observe

minerals and their melt inclusions. The polishing process ended when melt inclusions were on the surface and there were no lines or holes on the host crystal surface.

When using straw holders, we took special care to preserve the melt inclusions. These holders were first polished on the face with the grains using 180-grit sandpaper. After that, the straw holder was cleaned inside a beaker filled with ethanol that was put into an ultrasonic cleaner for 3 minutes. The sandpaper was changed depending on how much of the crystals or groundmass had been abraded. Continuous detailed observations of the holders and melt inclusions were performed during the whole polishing process, which included the use of a wide range of 180 to 5000-grit sandpaper. Additionally, for every sandpaper change, the cleaning process was repeated. The sandpaper grinding process ended when no lines or holes were observed on the sample surface.

A final polishing step was made by a polishing machine and alumina powders of 1 μm and 0.5 μm. This final step was mandatory before microprobe, ion microprobe and Raman spectroscopy analysis.

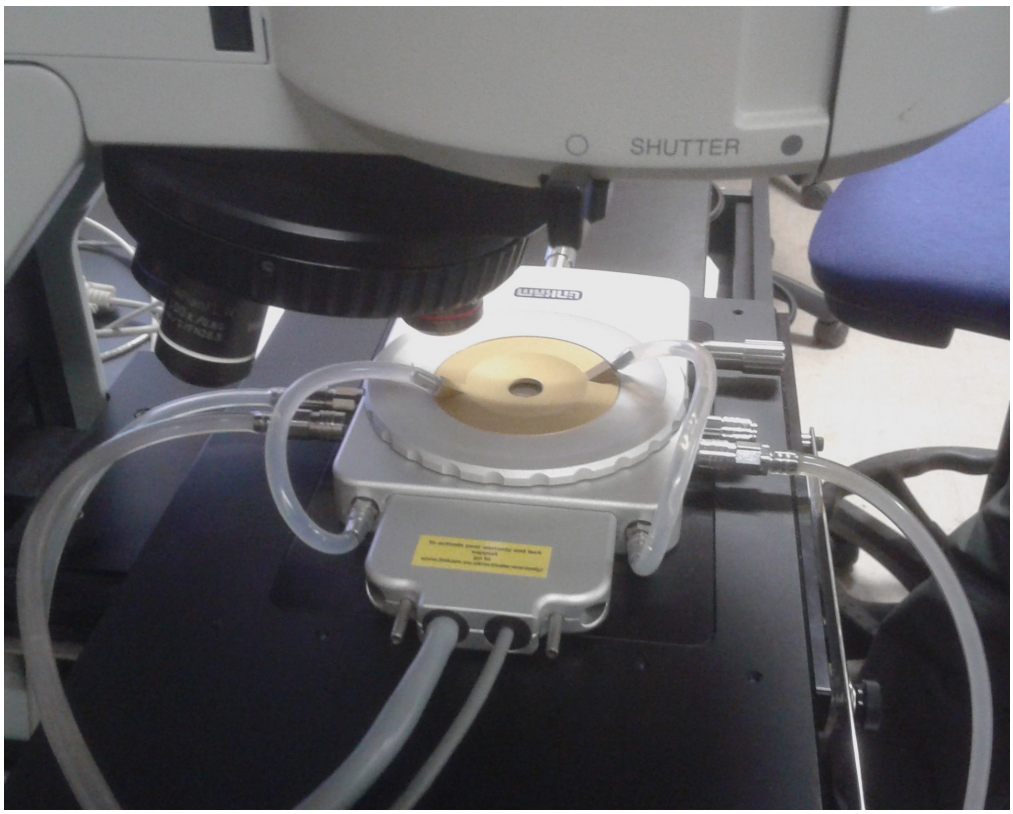

Figure 4.3: High temperature stage used for performing re-heated experiments attached to a transmitted light microscope. Resolution of the stage allows to watch minerals with a 10x objective. Stage has one hose for Ar gas and four hoses for cooling system which brings cold water to the stage enabling the quenching process of homogenized melt inclusions.

4.6. MICROTHERMOMETRY APPROACH

In this study, several melt inclusions were bubble-bearing MIs, and therefore a handful of them were subjected to microthermometry experiments in order to homogenize both the solid and gas phases. To perform microthermometry experiments, we used a high-temperature LINKAM TS1400XY stage (figure 4.3), which uses Ar gas to prevent oxidation of the mineral. Experiments were carried out at the **"Laboratorio de Inclusiones Fluidas y Vítreas"** in the Department of Geology at the University of Chile.

Microthermometry experiments were based on previous instrument calibration, based on gold and silver standards, to compare the measured homogenization temperatures. Melting temperatures of 1064.0 °C and 962 °C for gold and silver, respectively, were used as internal standards and thecalibration was carried out at the beginning and end of each homogenization experiment.

Crystal embedded in Epoxy was picked up from Epoxy blocks with a hot needle (figure 4.4). After that, those picked-up crystals were laid a nigh into a Petri dish filled with acetone to set apart the remaining Epoxy fragments.

The Epoxy-free crystals were each mounted onto a sapphire sample slide and Ar was released into the internal stage atmosphere.. We programmed different temperature ramps and an upper limit temperature for olivine was set to 1100 °C. The different ramps had a higher rate at low temperatures (<600 °C) and a lower rate at higher temperatures (>900 °C). Once the limit temperature was reached, the crystal was quenched by a cooling system based on cold water and the sample was taken out of the ceramic heater.

Figure 4.4: High-temperature needle used to liberate minerals from Epoxy mounts. The needle is plugged into the electrical socket and works by resistance. By increasing the current, the temperature increases and allows the needle to locally melt the necessary epoxy to "free´´ the crystals.

4.7. SCANNING ELECTRON MICROSCOPE

Scaninng electron microscope (SEM) was used to obtain images of crystal embedded in Epoxy and its hosted melt inclusions. We used a FEI model Quanta 250 (figure 4.5 of the Andean

Geothermal Center of Excellence (CEGA) available in the Department of Geology, Faculty of Mathematical and Physical Sciences, at the University of Chile. The voltage was 20 kV with a 5 μm-diameter beam at a pressure of 10^{-6} Pa.

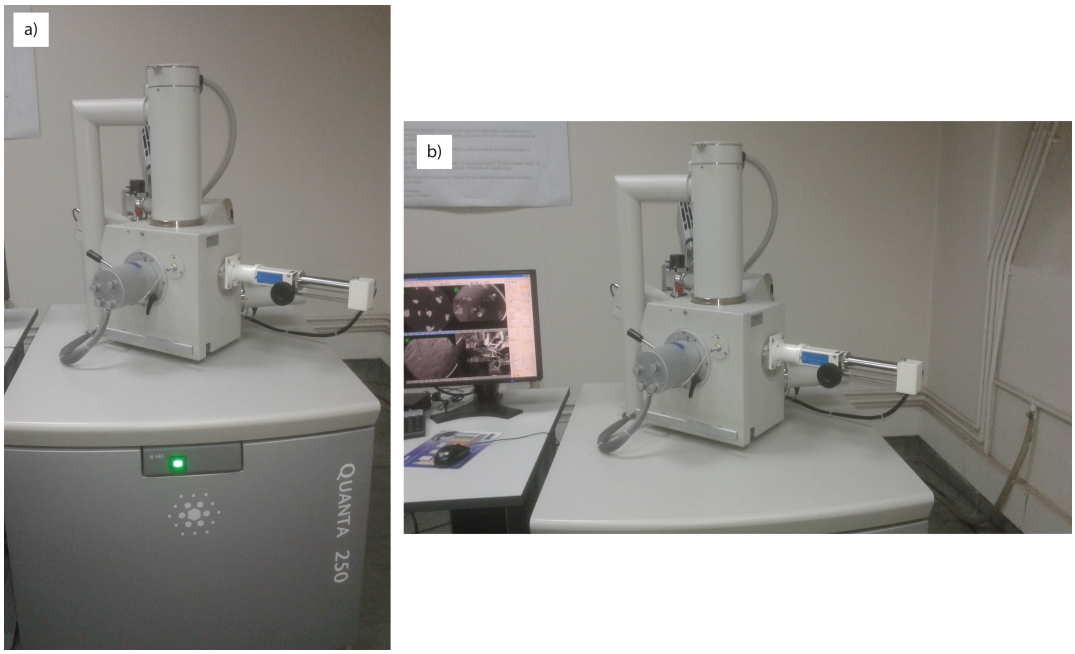

Figure 4.5: Scanning Electron Microscope (SEM), Department of Geology, University of Chile. SEM analytical conditions were high pressure, 20 kV and a spot size of 5 μ m. The EDX detector is on the back of the vacuum chamber.

4.8. RAMAN SPECTROCOSPY

Raman spectroscopy analysis of bubble-bearing olivine-hosted melt inclusion from Lonquimay stratacone (n=7 bubles) and Cono Navidad (n=27 bubbles) was carried out with a Typ Horiba Jobin-Yvon Labram HR800UV at the **Department of Experimental and Applied Mineralogy, Geowissenschaftliches Zentrum (GMZ)**, George August University of Göttingen, Germany.

We used either 100x objective or 100x LWD objective depending on melt inclusion position into the crystal; for shallow melt inclusion, we used a normal 100x objective and for deeper melt inclusions, we used a 100x LWD objective. Additionally, the laser was a Dihode Coherent with a wavelength of 487.91 nm, and a diameter of 100 μm. For olivine was taken one acquisition, for 60 seconds with 5 measurements. For plagioclases, it was reduced to 1 acquisition, for 30 seconds with 3 measurements.

4.9. MICROPROBE ANALYSIS

Major element determination in minerals and melt inclusions were obtained through a microprobe JEOL JXA 8900 (figure 4.6) available at the Geoscience center (GZM), George-August University of Göttingen, Germany.

We measured minerlas and melt inclusions in thin sections and mounted in Epoxy blocks. Additionally, we used a defocused beam to analyze melt inclusions, glass and plagioclases. Likewise, we used a focused beam to measure olivine and pyroxene composition. Voltage and current were set at 15 kV and 1.5x10^{-8} A respectively. Beam diameter was set at 5 or 10 μm based on the target size as well. For instance, melt inclusions were usually measured with 5μm-diameter beam but larger crystal were measured by the 10μm-diameter beam.

Finally, in order to quantify composition, the following standards were used wollastonite (SiO_2 and CaO); forsterite (MgO); albite (Na_2O); hematite (FeO); anortite (Al_2O_3); rutile (TiO_2); sanidine (K_2O); rhodonite (MnO); halite (Cl); and topazium (F).

4

4.10. SECONDARY ION MASS SPECTROSCOPY (SIMS)

Ion probe analysis were performed to determine minor elements in minerals and melt inclusions, as well as volatiles (CO_2, H_2O, F and Cl). We used a CAMECA IMS 4f with Cs microbean ion source with pumping to produce Cs^+ ions at 2x10^{-8} Torrs of vacuum. Ion probe analysis were carried out at the Great Institute, School of Geosciences, University of Edinburgh, United Kingdom.

The melt inclusions had a free exposed glassy phase of almost 45x45 μm^2 in order to measure correctly minor elements. The analysis were performed in three steps. In the first step was measured only CO_2 and it lasted four hours for twelve melt inclusions. The next step lasted four hours for other twelve melt inclusions where H_2O, F, Cl, Li and B were measured. In the last step, it was measured traces elements and rare earth elements during eight hours.

Figure 4.6: Electron Micro Probe (EMPA) in Geoscience center (GZM) , George-August University of Göttingen. The picture shows the vacuum chamber where we introduced holders and thin sections for analysis.

5

RESULTS

5.1. SAMPLES

There were four samples representing two lavas, one from the Navidad eruption (NV18, NV19, NV24) and the other from the Lonquimay stratocone (H4). The Navidad lava samples (NV18, NV19, NV24) were collected from the lava front of unit Navidad 1 (figure 5.1), which corresponds to the last stage of the Navidad eruption. This lava is melanocratic with a porphyritic texture. Plagioclase is the most common phase, while olivine is scarce. Lonquimay lava sample (H4) was collected from unit Lonquimay 4 (figure 5.1) , which corresponds to a Holocene eruption. This lava is also melanocratic and porphyritic, with the same crystalline degree as the Navidad lava. Moreover, the main phenocryst phase is plagioclase, and olivine is scarce.

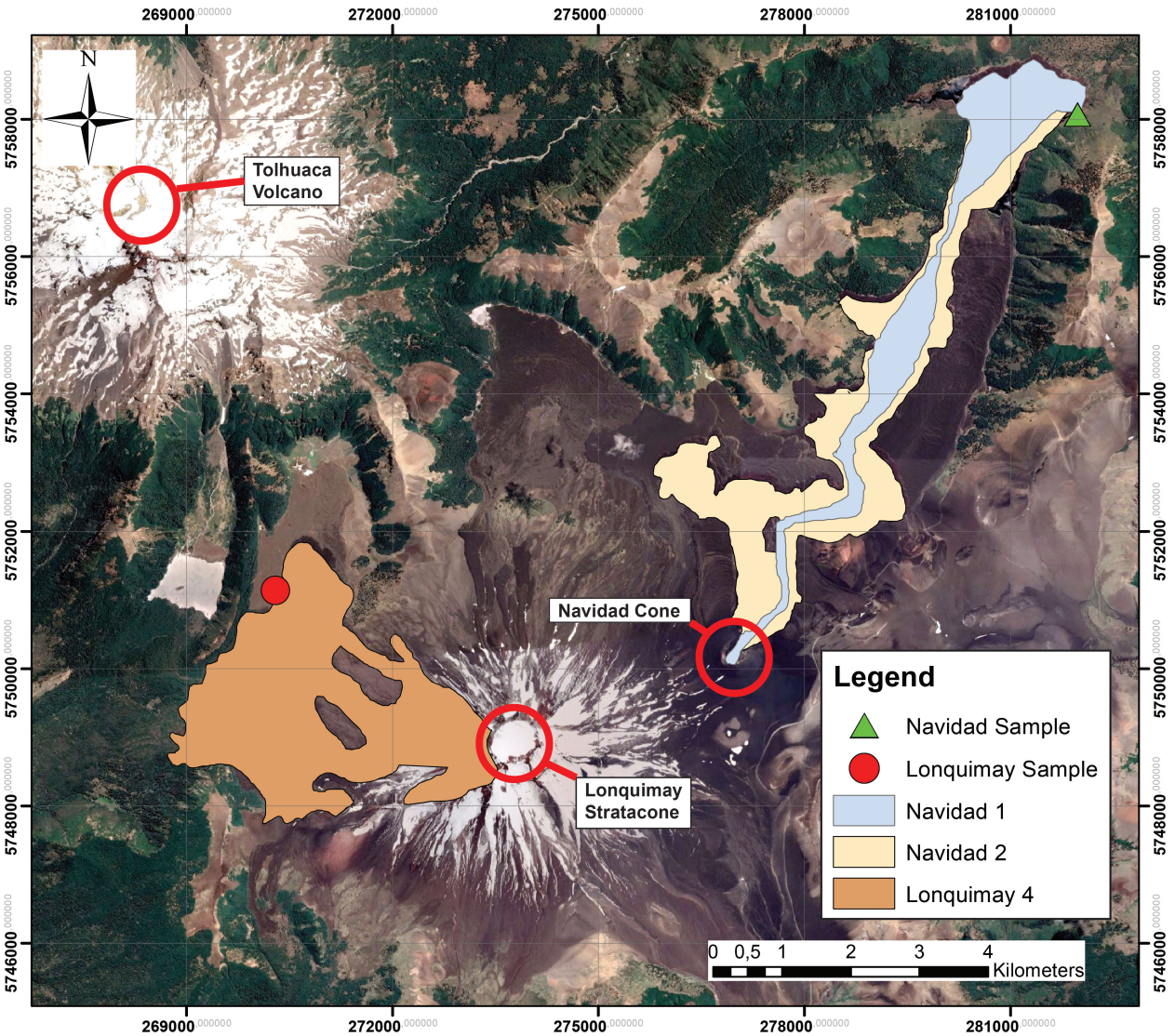

Figure 5.1: Location of samples collected at LVC. Navidad lava is represented by a green triangle located on the upper-right side of the map. Lonquimay lava is represented by a red circle located at the middle-left side. Navidad and Lonquimay units are based on Moreno et al. (1989)[55] and Gilbert et al. (2014)[30].

5.2. MINERALOGY

The Navidad lava is composed of feldspar, clinopyroxene, olivine and in lesser amounts opaque minerals (ülvospinel). We observe two types of feldspars, whose phenocrysts and microcrystals have a labradorite and bytownite composition and an andesine and labradorite composition, respectively (figure 5.2a). The phenocrysts commonly exhibited alternating zoned textures that varied between Ca-richer and Ca-poorer bands. Feldspar-hosted MIs - which were not studied in this thesis because they were recrystallized - are found in Na-rich feldspars with a sieve texture. High-K feldspars are completely absent, but a small amount of K_2O is incorporated into the labradorite and bytownite structures in quantities below 4 wt.% (figure 5.2a).

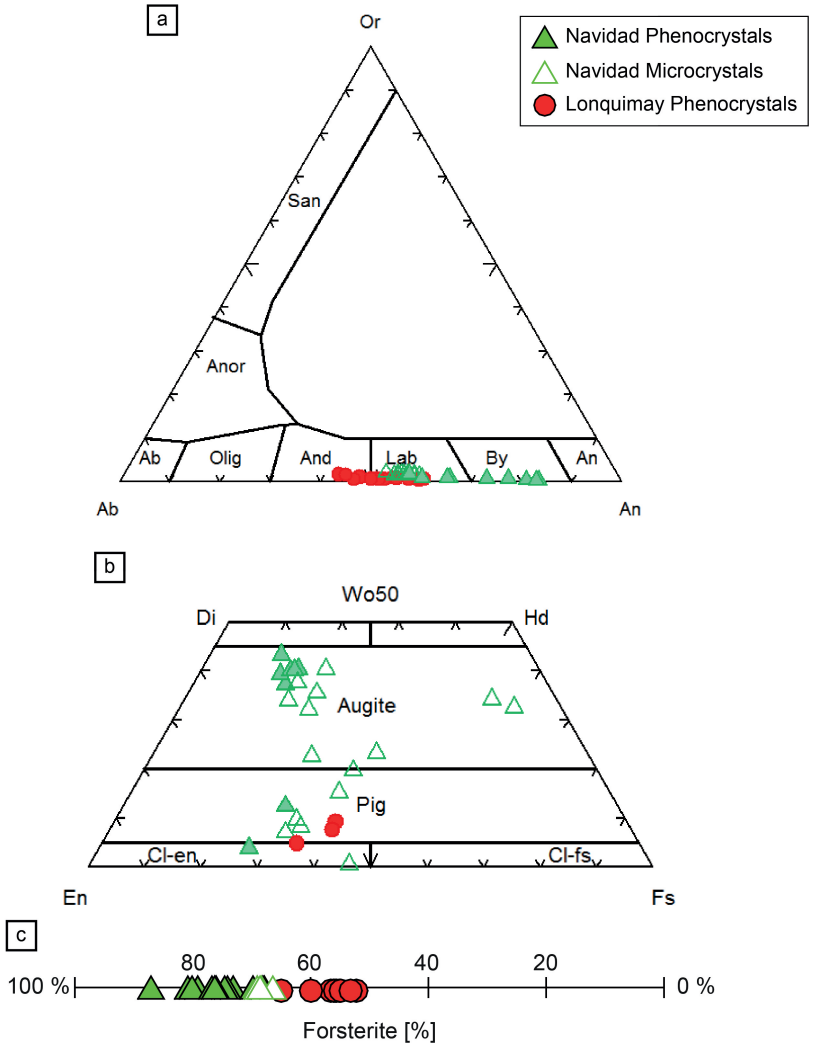

Figure 5.2: Mineral classification diagrams. a) Plagioclase classification diagram, showing small amounts of K and plagioclase ranging from andesine to bytownite. Navidad phenocrysts are more anortitic in composition. b) pyroxene classification quadrilateral (Morimoto et al., 1988), showing a great range of Ca in pyroxene; it is also important to note that the vast part of phenocrystals plot in Mg-rich areas. c) Fo diagram showing olivine from Lonquimay (fayalite-rich) and Navidad (Fo-rich).

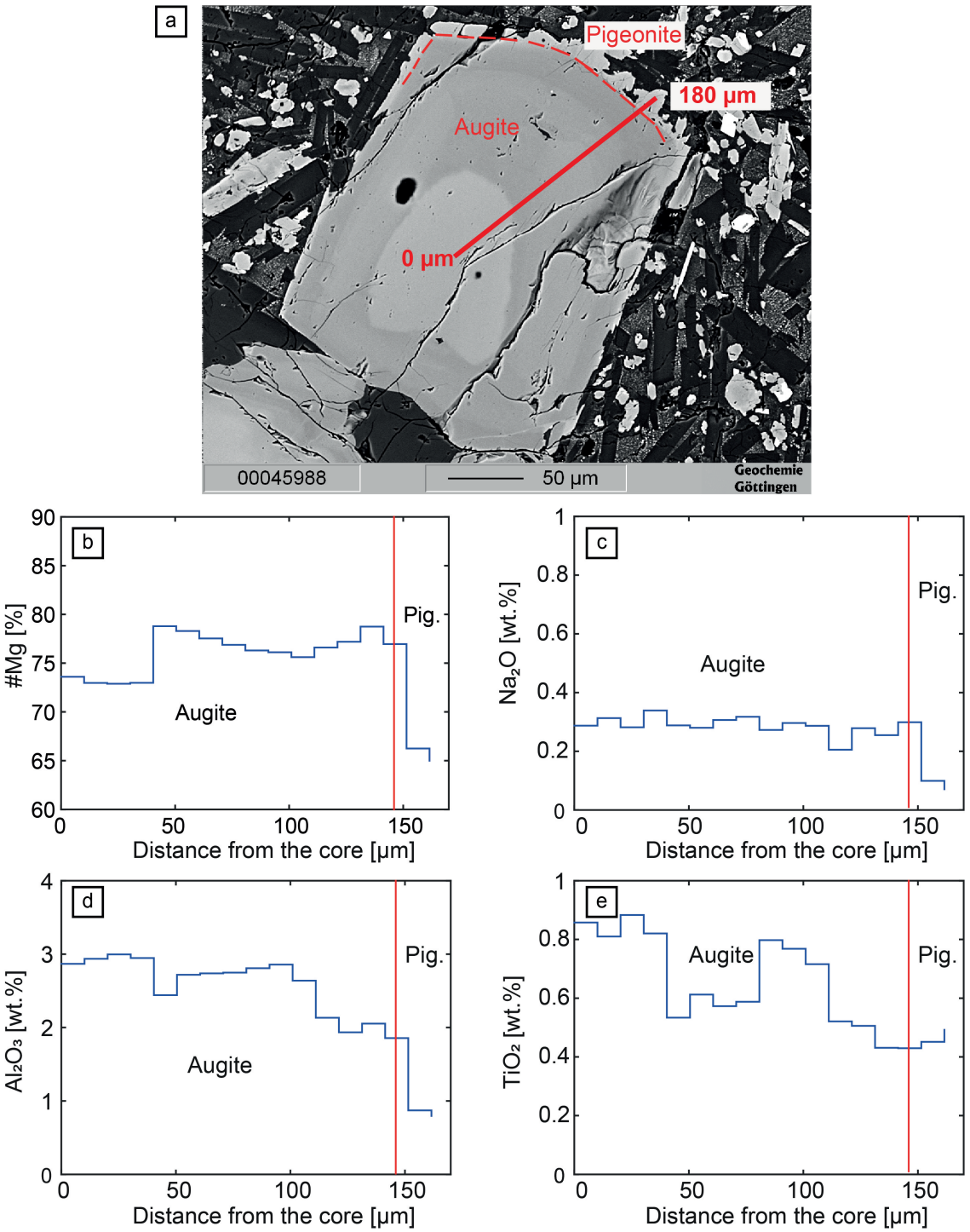

Figure 5.3: Zoned clinopyroxene. a) EMPA image, with marked zonation between pigeonite and augite; augite is also zoned, although to a minor extent. b) #Mg variation from augite to pigeonite. c) Na_2O contents, showing an almost constant concentration. d) Al_2O3 trend, showing a smooth decrease of this oxide in pigeonite. e) Variation of TiO_2 (in white).

In contrast, the overall clinopyroxene composition is more scattered. Clinopyroxenes have an augite composition with high-Fe and high-Mg, as well as a high-Mg pigeonite, diopside and clinoenstatite composition (figure 5.2b). It is common to find zoned phenocrysts, whose average composition varies sharply in Ca more than in #Mg extending outward (figure 5.3b). Some phenocrysts have pigeonite rims on augite cores (figure 5.3a), and zoned clinopyroxene incorporated into small amounts of Al_2O_3 (below 3 wt.%) that steadily decrease toward the rim. This pattern is also observable for other minor elements, such as Na_2O (figure 5.3 c and d). The scatter composition is not only restrained to phenocrysts but it is common in microcrystals as well. However, it is constrained to Mg-richer phases such as clinoenstatite, Mg-rich pigeonite and Mg-rich augite (figure 5.2b). On the other hand, olivine displays a wide range of compositions. Smaller crystals (SIZE) contained more Fe^{2+} in their structure, showing a compositional variation from Fo_{67} to Fo_{77}. The phenocrysts, have compositions between Fo_{70} to Fo_{90} (figure 5.2c). Unlike the Fo variation in olivine, the majority of olivine exhibit a decrease in #Mg toward the rim (figure 5.4 c), where sometimes it is possible to observe pigeonite recrystallization (figure 5.4 b). Additionally, only a few olivine grains have orthopyroxene cores, with the same pattern of decrease in Fo. High Fo olivine contains several MIs, which are the focus of this research.

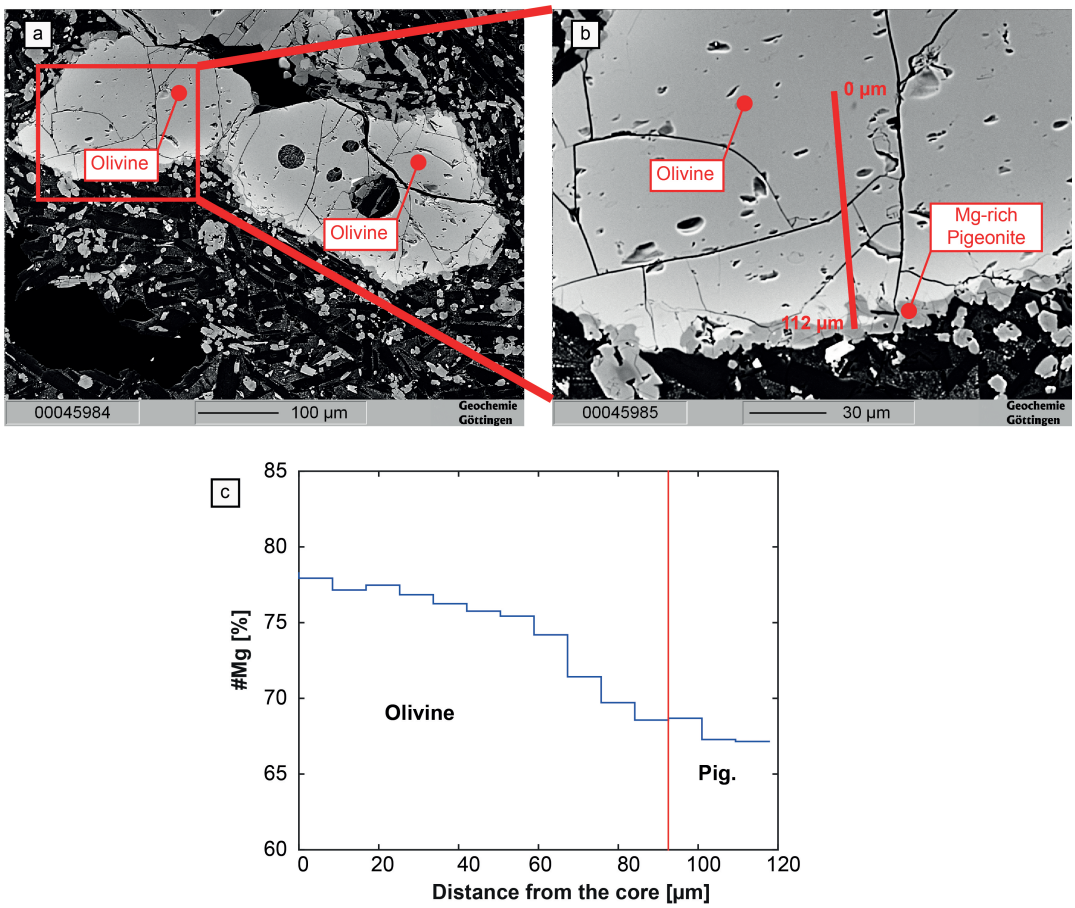

Figure 5.4: Olivine Zonation. Some olivines show a pigeonitic rim, with Fo decreasing toward the rim. a) Olivine pair with pigeonitic rim. b) zoom of a), showing that the olivine was not in equilibrium with the surrounding melt. c) Diagram showing the #Mg zonation in olivine.

Lonquimay lavas (H4) have the same mineralogy as the Navidad lava, although we could ob-

serve some differences in composition and size of the minerals. Regarding size, plagioclase crystals have diameters no-greater than 500 vm and olivine and clinopyroxene hardly ever reached 200μm in diameter. The plagioclase crystals have a euhedral habit with compositions ranging between andesine and labradorite (figure 5.2 a). Unlike the Navidad lava, feldspars do not show evidence of zoning and their composition is constant, with a lack of K-rich feldspar (figure 5.2 a). Clinopyroxene has a homogeneous pigeonitic composition, with higher contents of $MgSiO_3$ (figure 5.2 b). Olivine compositions range between Fo_{50} and Fo_{65} (figure 5.2c). As for the Navidad lava, olivine-hosted melt inclusions from Lonquimay stratocone lavas are the focus of this study.

5.3. MELT INCLUSIONS

Melt inclusions (MIs) are observed in every mineral phase of each sample (stratocone and Navidad), although not every MI is suitable to be studied. In this study, we described a total of 270 MIs, which can be classified into two main groups. The first group, which definitely outnumbered the second group, is composed of recrystallized MIs with shrinking bubbles and daughter minerals (figure 5.5 a). Additionally, it was common in Group 1 to find some black recrystallized MIs (figure 5.5 b), trapped in plagioclase and clinopyroxene. The second group is the glassy bubble bearing melt inclusions (GBb-MIs) which, unlike recrystallized melt inclusions, they are concentrated in olivine and were unusual in plagioclase and clinopyroxene (figure 5.5 c and d). As the name suggests, the MIs are composed of a glassy phase with one or more bubbles and proportionally negligible daughter minerals - which are most likely inherited crystals. They have an ellipsoidal to rounded shape, with most grains having diameters of roughly 20 to 30 μm, and some MI diameters reaching 100 μm. They also seemed to not belong to a melt inclusion assemblage (MIA), but rather occur as isolated MIs.

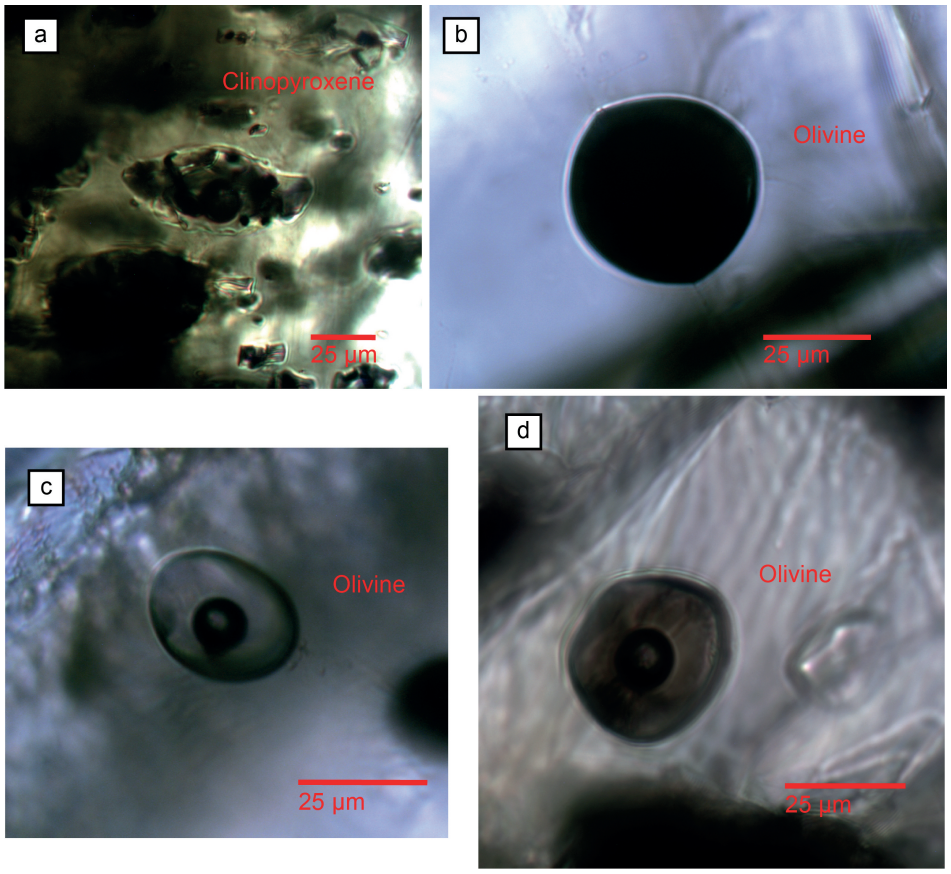

Figure 5.5: Different melt inclusions found in both samples. a) Melt Inclusions (MIs) in clinopyroxene (NV19). Minerals for both samples usually contained several recrystallized melt inclusions, with the occurrence of one or more bubbles. b) Black recrystallized MIs are less common than a), although they are found in almost all mineral phases. c) MI in olivine from the Navidad cone (GBbMI) compared to MIs (GBbMI) found in Lonquimay olivines. d) Olivine-hosted MI from Lonquimay lavas. They appear darker than olivine-hosted MIs from Navidad cone.

In order to measure CO_2 and water in MIs, microthermometry experiments were performed on Group 1 olivine-hosted MIs. Unfortunately, it was not possible to rehomogenize any of the recrystallized MIs.

Electron microprobe analysis performed at the University of Göttingen, Germany, determined the content of major elements in minerals and MIs. The obtained chemical compositions were corrected due to several possible error sources. For example, some glasses had anomalous Al_2O_3, $Fe^{2+}O$ and CaO concentrations due to the measurement of host minerals while the electron microprobe analyzed the glassy phase. Additionally, we needed to account for PEC processes and apply the correction for Fe-loss —described and corrected by Danyushevsky et al. (2000)[17] and Danyushevsky et al.(2011)[18] using Petrolog software—due to the possibility that there is no equilibrium between MIs and their host phase. The equilibrium is assessed taking into account the $K_D = 0.3 \pm 0.03$ empirically determined by Roeder and Emslie (1973)[73]. There are few MIs in equilibrium, but the majority of them show some degree of PEC. The Lonquimay olivine-hosted MIs displayed a greater degree of PEC than the Navidad MIs (figure 5.6).

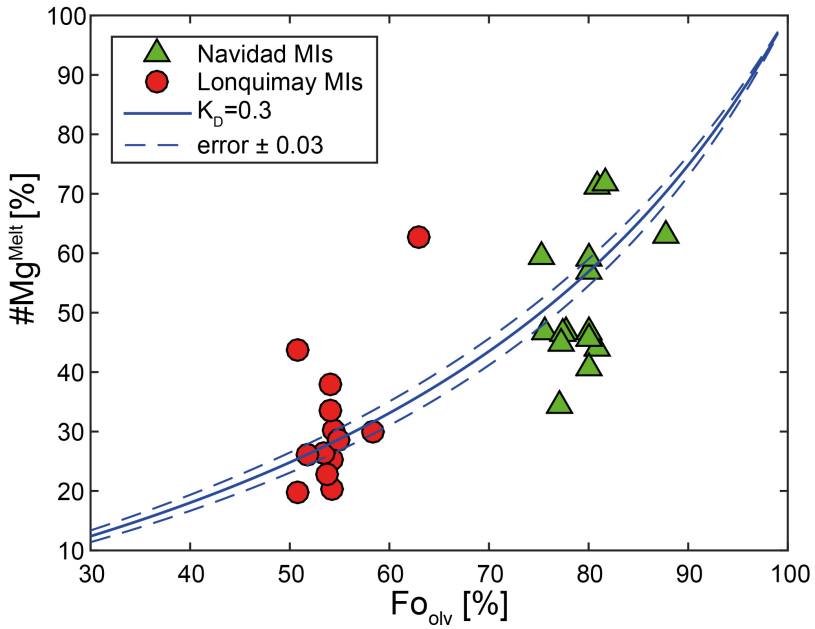

Figure 5.6: #Mg of MI vs Fo of olivine host. MIs closer to the blue line of $K_D = 0.3$ are supposed to be in equilibrium with their host.

In order to calculate the degree of PEC and correct the composition of MIs, we need to determine the oxygen fugacity of the system. We set the QFM oxidation state in Petrolog software to vary in the range between QFM and QFM-2 —to better resemble a less oxidized environment. We used a Fe^{3+}/Fe^{2+} ratio (5.1) following the procedure of Kress and Charmichel (1988)[45] and the QFM model (5.2) based on Myers and Eugster (1983)[56]. The calculated Fe^{3+}/Fe^{2+} ratios were 0.53 and 0.51 for Navidad and Lonquimay lavas, respectively.

$$ln[\frac{X^{liq}_{Fe^{3+}}}{X^{liq}_{Fe^{2+}}}] = 0.232 ln(fO_2) - \frac{\Delta H}{RT} + \frac{\Delta S}{R} - \frac{1}{RT}\sum \Delta W_i X_i \tag{5.1}$$

$$log(fO_2) = -\frac{24441.9}{T} + 8290 \tag{5.2}$$

Albeit a value of $K_D = 0.3$ should be used to assess MI-olivine equilibrium and to correct MIs in Petrolog, we used a value of K_D modified by Toplis (2005)[84], which has the advantage of incorporating modifications caused by either MIs or the olivine composition.

Once the correction is applied, every MI seems to be in equilibrium with its host. The correction shows an important decrease of #Mg in the Lonquimay MI, and an increase in Navidad MIs (figure 5.7). It is also important to note that Navidad MIs had more important corrections than Lonquimay MIs, with almost every Lonquimay MI experiencing a certain degree of PEC.

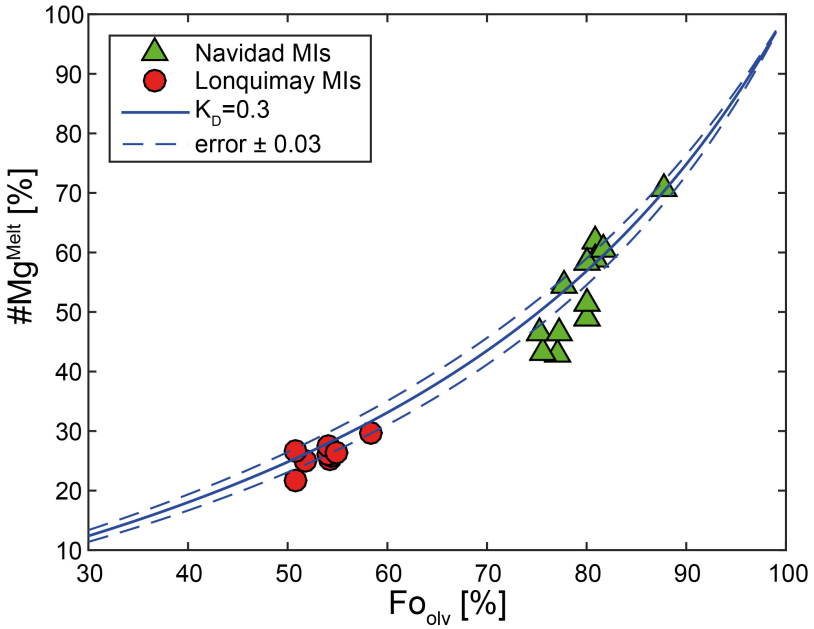

Figure 5.7: #Mg of MI vs Fo of olivine host after the Petrolog calculation. MIs that shifted closer to the blue line are now in equilibrium with their hosts.

5.4. MELT INCLUSION MAJOR ELEMENTS

The Navidad MIs have a less evolved composition than the Lonquimay MIs. Navidad MI compositions straddle the boundary between basalt and basalt trachyandesite, also reaching the trachyandesitic field. Their SiO_2 content ranges from 52 wt.% to roughly 60 wt.%. The amount of alkalis is between 4 to 8 wt.%. Lonquimay MIs are more evolved, but they also plot in the andesitic-basaltic field. Moreover, the compositional trend ends in the trachydacitic field, with a silica content of 65 wt.%. Despite the fact that there is a clear trend of more evolved compositions, the alkalis increases with fluctuation in a rage of 1.5 and 2.5 wt.% . For instance, more primitive MIs with a basaltic-andesitic composition experienced an increase in alkalis with an increase in silica, but once they approach dacitic and trachydacitic compositions, they lost alkalis. Finally, the alkali content increases again until MIs reach trachydacitic compositions (figure 5.8.

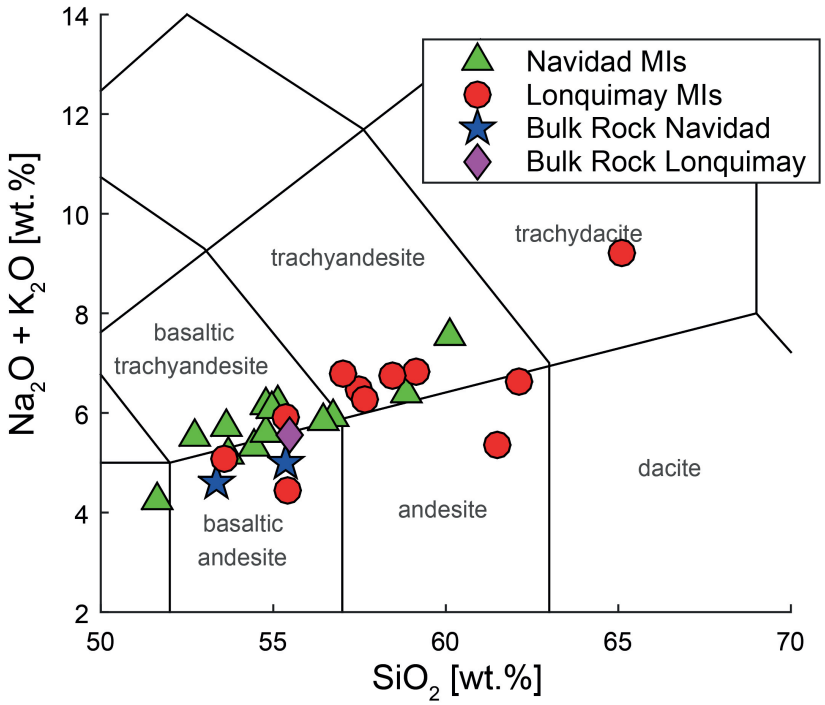

Figure 5.8: Total Alkalis Diagram (TAS, Le Bas et al. (1984)) showing that MIs compositions roughly follow a trachytic trend to end in an area of more evolved compositions. Navidad MIs are less evolved than Lonquimay MIs, although their trend is less scattered than the one of Lonquimay.

Harker diagrams suggest that there has been fractional crystallization of minerals such as plagioclases, augite and olivine. Regarding Navidad lavas, Harker diagrams of SiO_2, MgO and CaO show the unequivocal crystallization of olivine and augite. These diagrams show no evidence of coupled crystallization of olivine and plagioclase but do provide insight on plagioclase + augite and augite + olivine crystallization. Likewise, Lonquimay MIs show the same behavior as Navidad MIs. They also follow crystallization trends for minerals previously shown. Harker diagrams for SiO_2, MgO and CaO show olivine and pigeonite crystallization. Also, CaO, Al_2O_3 and SiO_2 did the same for plagioclase and pigeonite. The trends follow theoretical paths. For example, figure 5.9 b shows a sharp decrease of MgO when SiO_2 increases, associated with olivine crys-

tallization, followed by a change in slope when crystallization of olivine stops and augite begins to crystallize. This pattern clearly shows the instability of olivine with a high SiO_2 content.
The content of major elements, such as K_2O and Na_2O, increases in MIs when the melt becomes more evolved. For K_2O (figure 5.10 a and b) versus MgO, the trend remains usually constant. However, when between 6 wt.% MgO and 1.5 wt.% MgO, and MgO content goes below 1 wt.%, then K_2O increases roughly exponentially. Moreover, this increase is steeper in Lonquimay MIs than that in Navidad. Although K_2O does not increase as much and as quickly as MgO, it is steady for both volcanoes, i.e. the concentrations increase at the same rate during the whole increase of K_2O. However, as expected, Lonquimay MIs have greater contents of K_2O than those from Navidad.

Conversely, Na_2O displays a dissimilar behavior in both volcanoes. While the increase is gradual in Navidad MIs as MgO decreases, Lonquimay MIs exhibit a steep trend only starting at 2 wt.% MgO with a 3 wt.% of Na_2O and ending at 0.7 wt.% of MgO with about 8 wt.% of Na_2O. This behavior is not observable for the Na_2O versus SiO_2 diagram, where both sets of MIs show the same increment trend, although high-silica Lonquimay MIs had abnormally low concentrations of Na_2O (figure 5.10 c and d).

The variation of the TiO_2 vs MgO diagram (figure 5.10 e and f) shows a steady increase of Navidad MIs as the melt evolved. This pattern is sharper in the Harker diagram than the MgO plot. In addition, titanium dioxide has more scatter in the MgO diagram than in the Harker diagram, but this scatter is also observable in high-silica MIs. Lonquimay MIs also show a distinct increase similar to Navidad MIs in the MgO diagram. However, there are some abnormal data with a slightly greater content of TiO_2 in MgO depleted MIs, which plot slightly off the main trend. In the Harker diagram, Lonquimay MIs seem to have a smaller rate of increase than Navidad MIs as silica increases although the concentration of TiO_2 is higher in Lonquimay MIs. Additionally, it is worth mentioning that high-silica MIs have an abnormal behavior for TiO_2. This abnormal behavior of high silica MIs from the Lonquimay lava is observable for both K_2O and Na_2O.

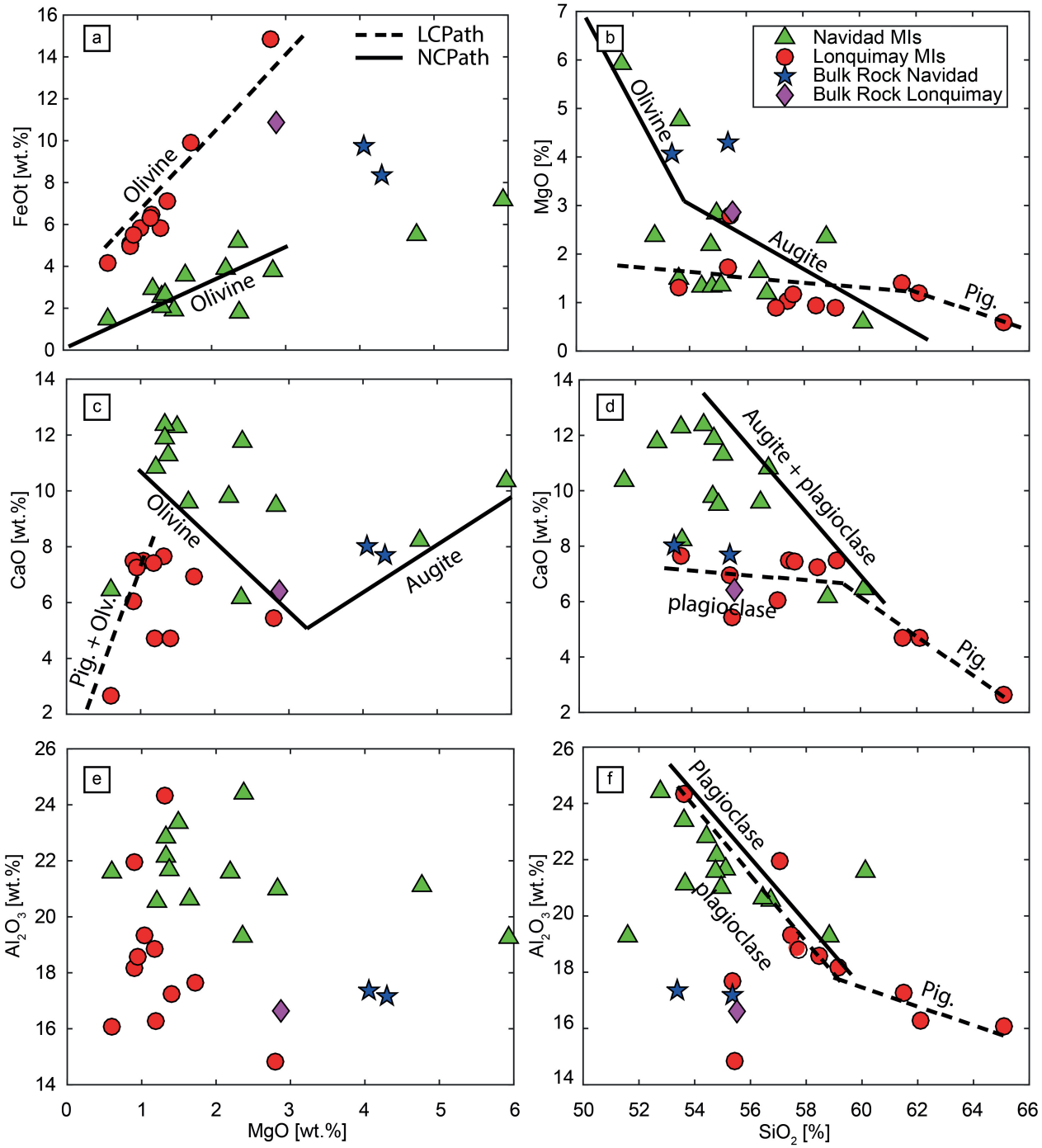

Figure 5.9: Harker diagrams for major incompatible elements in MIs. Incompatible elements increase as magma evolves. At very low amounts of MgO, the rate of increment is steeper. Bulk rock composition tends to be the average of MIs compositions in every diagram. More evolved Lonquimay MIs show anomalously scattered compositions. Every plot shows the variation of major oxides with respect to MgO (left diagrams) or SIO_2 (right diagrams).

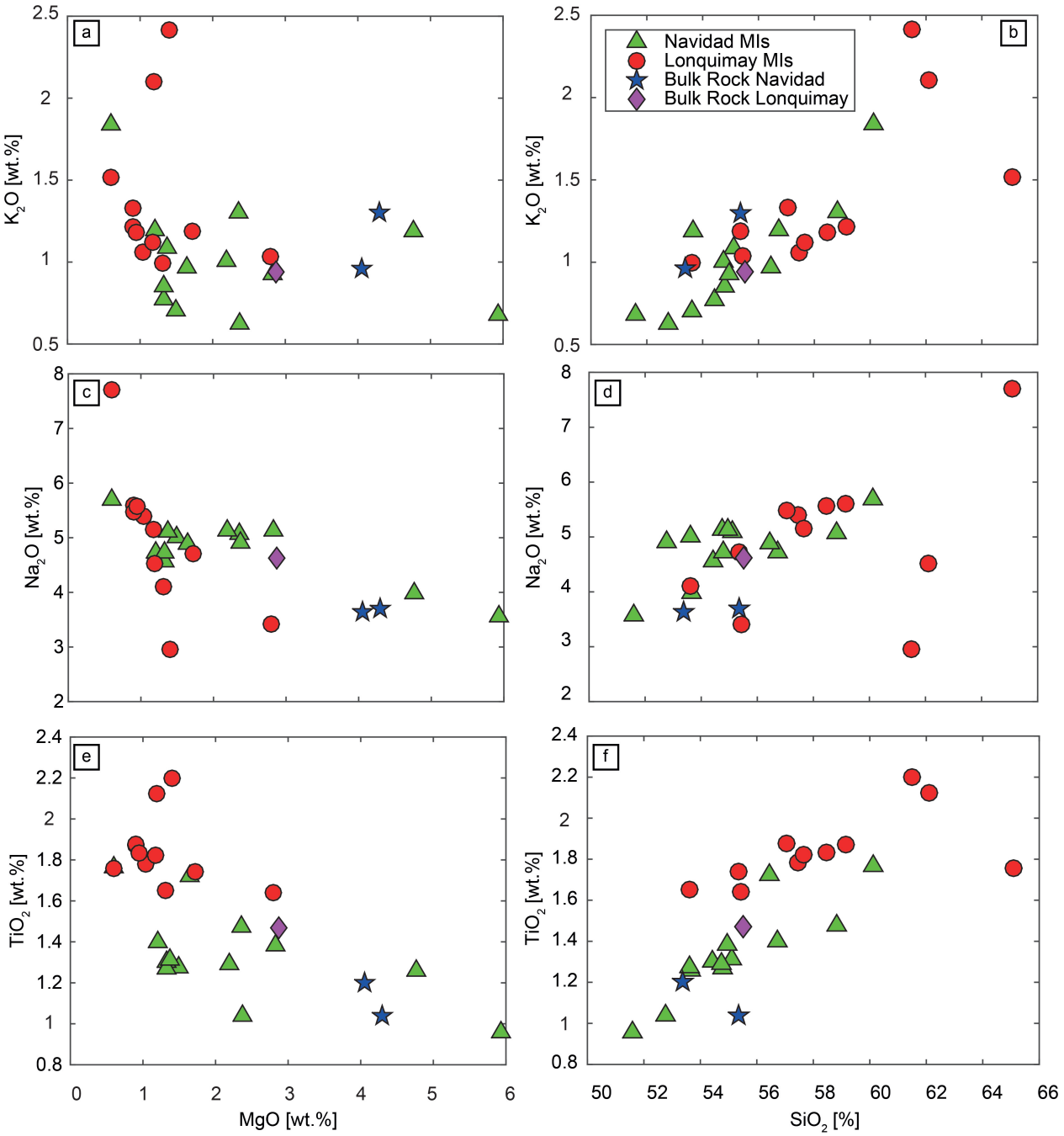

Figure 5.10: Harker diagram for major elements in MIs. Every plot shows major oxide variations vs either MgO (left diagrams) or SIO_2 (right diagrams). We can observe the crystallization trend of the main mineral phases, which in our study are plagioclase, augite and olivine. MIs compositions are in constrast with their bulk rock composition.

5.5. MELT INCLUSION MINOR ELEMENTS

The number of MIs analyzed for trace elements is noticeably smaller than the number analyzed for major elements, primarily because not all MIs had the necessary diameters to fulfill the beam-size requirement. Therefore, only 9 MIs from a total of 24 were measured for trace elements.

5.5.1. WATER AND CARBON DIOXIDE

Water and CO_2 are the most common volatiles in volcanic system. Therefore, the study of volatiles is fundamental for understanding the complexity of a magmatic system. As previously mentioned, measurements were done by ion microprobe and Raman spectroscopy.

Seven melt inclusions from Navidad lava were suitable for analysis and only two from the Lonquimay lava. The results show that Navidad MIs contain a scarce amount of water between 0.1 to 0.24 wt.% of the total mass. Its average composition (n=7) is 0.13 ± 0.04 wt.%. Along with other incompatible elements, water increases as magma evolves but this increment, which increased the water content by only 0.05 wt.%, is almost negligible in our MIs. Although we do not have much data for water content from Lonquimay MIs, it is possible to observe an inverse behavior when compared to Navidad MIs. Water decreased as Lonquimay MIs evolved, and this drop is considerable, changing from 0.15 wt.% to 0.01 wt.%. Navidad MIs are also water-poor(figure 5.11), with an average content (n=2)of 0.08 ± 0.09 wt.%.

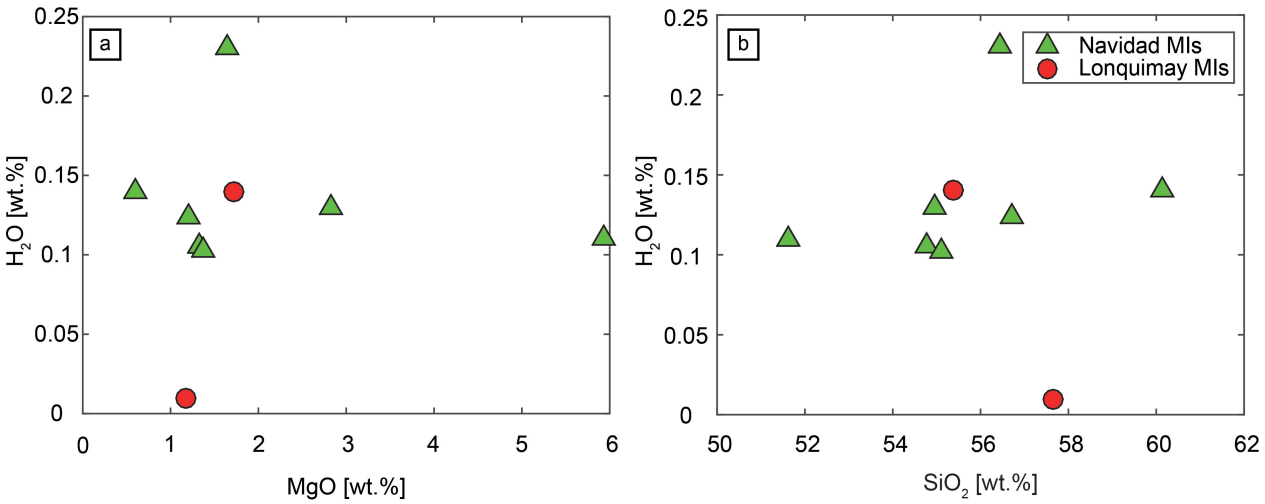

Figure 5.11: Amount of water in Navidad and Lonquimay MIs. Water increased as MgO decreased and SiO_2 increased, showing an enrichment while MIs became more evolved.

Results of carbon dioxide measurements in the melt are different than those for water, with carbon dioxide content being in the range of worldwide volcanic systems. The maximum amount of CO_2 within the glassy phase of MIs does not exceed 1400 ppm. Results show that Navidad MIs contain more CO_2 than Lonquimay MIs. The richest CO_2 Navidad MIs exceeds the highest Lonquimay values by 1000 ppm. CO_2 content in Navidad MIs increases as the melt evolves but the increase is quicker with respect to MgO than SiO_2. Moreover, the former seems to follow

an exponential curve while the latter follows a straight line. As was the case for the water, there is a MI that has an anomalous concentration of CO_2 with respect to the main trend. This MI is more abundant in CO_2 than the richest of the data along the main trend but this gap is not significant. As is shown in figure 5.12, the difference between the CO_2-richest Navidad MI and the anomalous one is not larger than 100 ppm. In contrast to water, Lonquimay MIs seem to show an increase in CO_2 content as the melt evolved —we reported a sharp decrease of water for Lonquimay MIs in the above paragraph. This increase could not be predicted due to the lack of data, but it seems to be as steep as the Navidad trends (figure 5.12).

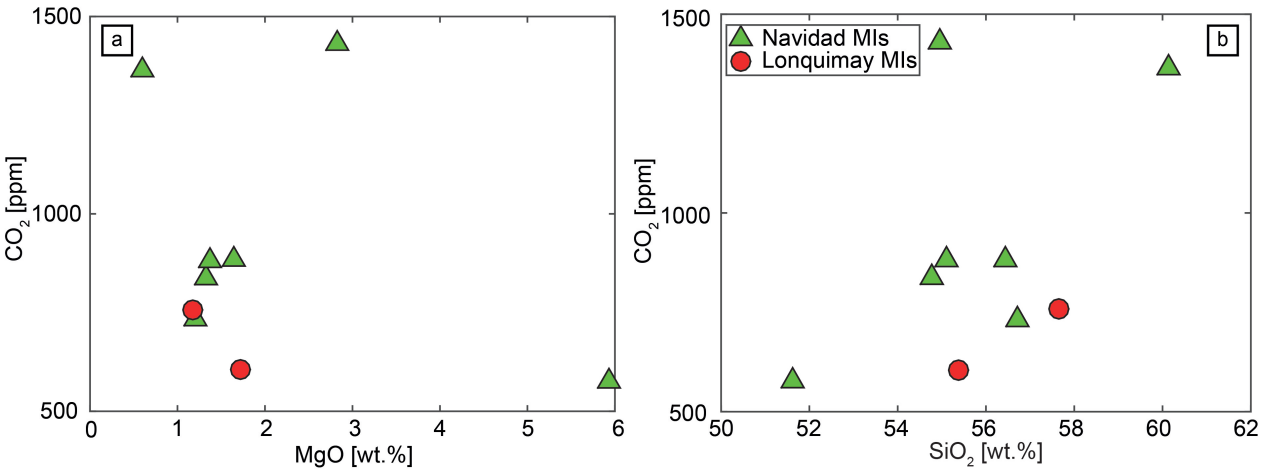

Figure 5.12: Carbon dioxide composition and variation as magma evolved. CO_2 increased quickly, although one data point (NV19.O.07) seemed far away from the main trend.

Melt Inclusion	CO_2 in melt [ppm]	CO_2 in bubble [ppm]	CO_2 total [ppm]	% CO_2 in bubble
NV18.O.AK.MI_01	813	70.5	**883.5**	**8.7**
NV19.O.19.MI_02	1293	136.6	**1429.6**	**8.7**
NV19.O.13.MI_01	492	83.4	**575.4**	**15**
NV19.O.07.MI_01	1300	65	**1365**	**5.5**

Table 5.1: Carbon dioxide calculated from bubbles within Navidad MIs. The total amount of CO_2 in the bubbles represents between 5 to 15 % of the total CO_2 in MIs. The methodology used for this calculation is based on Esposito et al. (2011)[25] and Steele-MacInnis et al. (2012)[81].

Some MIs may concentrate great amounts of volatiles, such as water and CO_2, in their shrinking bubble as Esposito et al. (2011) have previously reported, and the volatiles can be observed and quantified by Raman spectroscopy. Raman analysis of our samples did not show any evidence of water within MIs bubbles (figure 5.13). Furthermore, several were completely empty, suggesting that the total water content for Lonquimay and Navidad MIs is represented only by the water inside the glassy phase. In contrast, we detected carbon dioxide in several MIs bubbles. Navidad MI bubbles with carbon dioxide considerably outnumbered those in Lonquimay MIs. Moreover,

from the total amount of bubbles analyzed, just one Lonquimay MI had carbon dioxide within the bubble (figure 5.13). The Raman spectroscopy data show the two Fermi diads for Navidad MIs with a $\Delta_1 = 102.12$, and two MIs show a Fermi diad of $\Delta_2 = 103.88$. Using the densimeter proposed by Lamadrid at al. (2018) (equation 5.3), Δ_1 gave a negative density which is physically impossible hence we calculated the amount of CO_2 in the bubble with Δ_2. Finally, using both data obtained by ion microprobe and Raman spectroscopy, it was possible to observe that the amount of carbon dioxide in the bubbles of our MIs represents only 5 to 15 % of the total content. The total carbon dioxide average compositions of the MIs are (n=7) 957.8 ± 319 ppm and (n=2) 681.5 ± 108 ppm in Navidad and Lonquimay, respectively.

$$\rho = 0.354812\Delta - 36.42055 \tag{5.3}$$

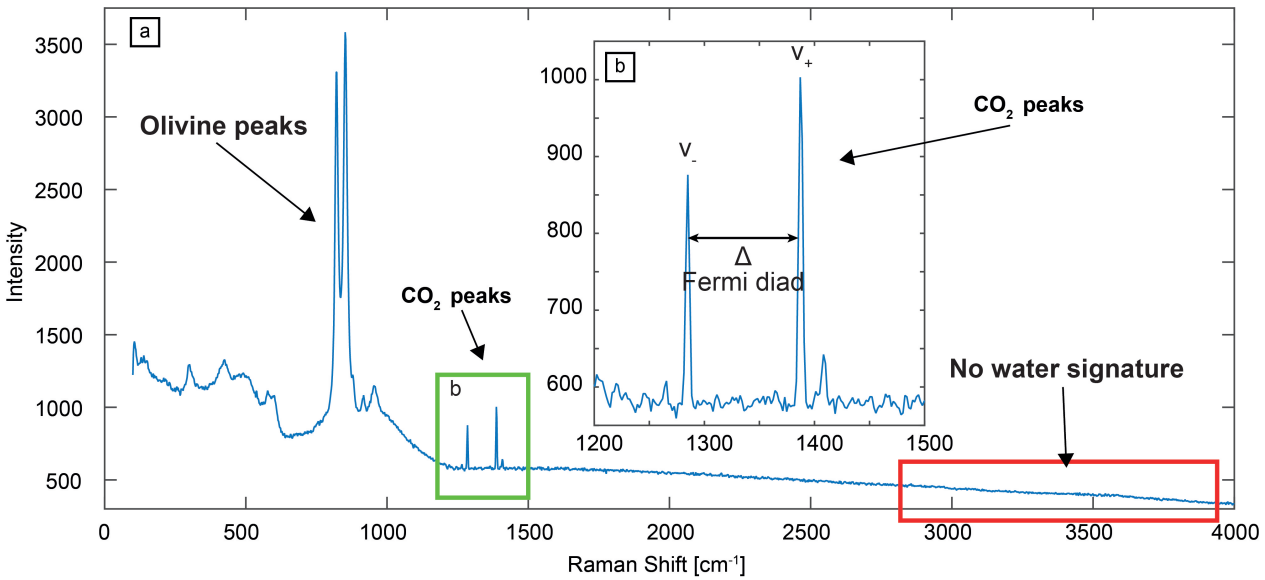

Figure 5.13: Raman spectrum of Navidad MI (NV18.O.AK.MI-01) that showed the presence of peaks for CO_2 but not for water. The calculated Fermi diad for this spectrum is 103.88.

5.5.2. HALOGENS

During the 1988-90 Navidad eruption, several authors have documented an important fluorine degassing event from the Navidad cone. An anomalous concentration of fluorine in soils and rivers, as a result of the eruption, caused the sudden death of cattle close to the eruptive center.

Navidad MIs show high concentrations of fluorine and chlorine. The average chlorine content (n=7) is 905 ± 135.5, with a maximum of 1094 ppm and a minimum of 704 ppm. Chlorine content in MIs also increases as SiO_2 increases. Fluorine in Navidad MIs is also high, with an average concentration (n=7) of 568 ± 264 ppm, a maximum of 1054 ppm and a minimum of 204 ppm. Fluorine increases as the magma evolved as well. Both fluorine and chlorine show a positive correlation with each other, i.e. when fluorine or chlorine increase, the other increases as well (figure 5.14).

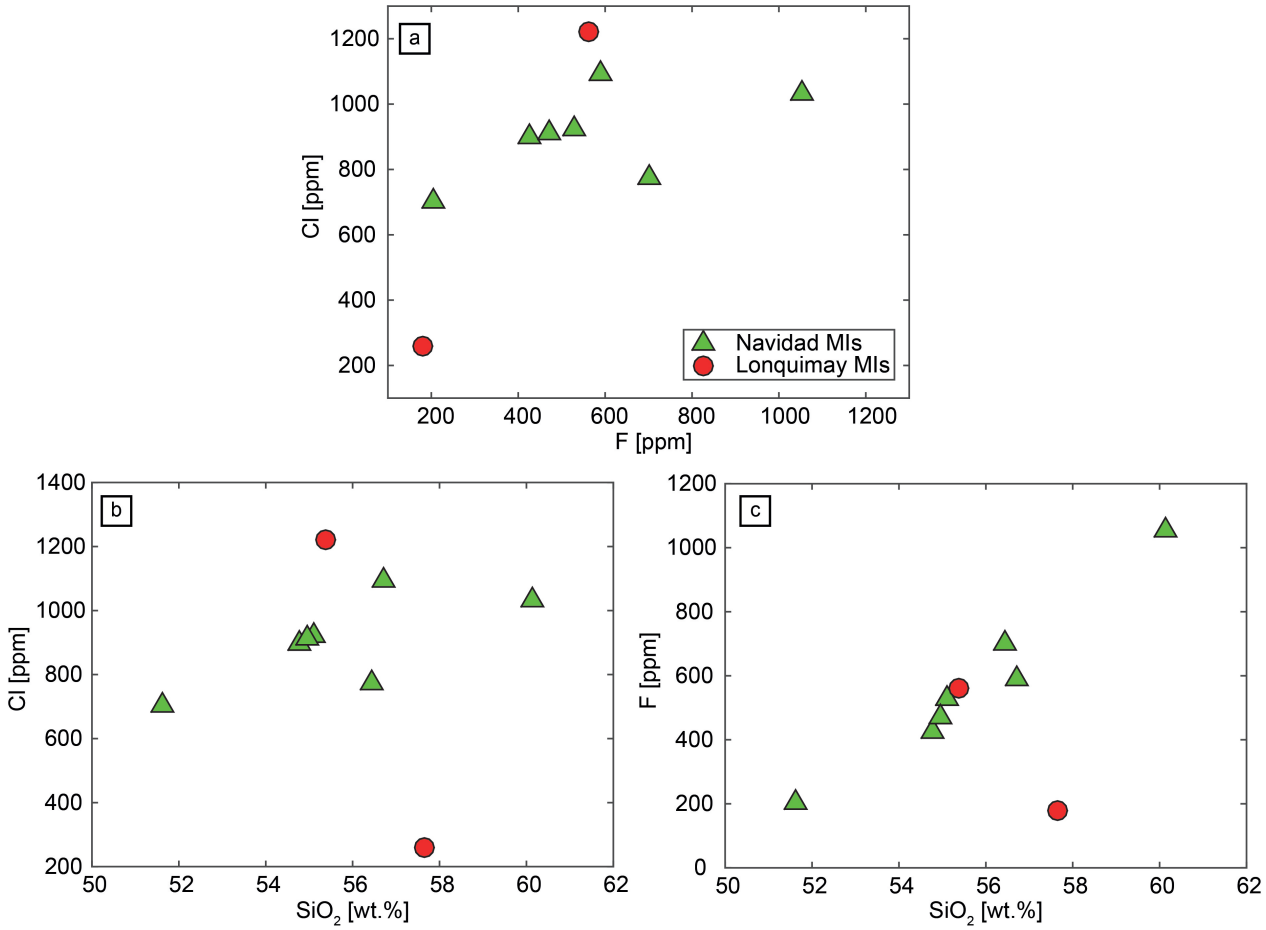

Figure 5.14: Fluorine and chlorine concentrations in Navidad and Lonquimay MIs correlate positively between each other. Both elements increase as magma evolves, but only in the case of Navidad samples.

Although there is only a small amount of data, Lonquimay MIs contain variable chlorine concentrations, with an average (n=2) of 739.5 ± 680 ppm, a maximum of 1220 ppm and a minimum of 259 ppm. Fluorine content is lower than that found in Navidad MIs, with an average (n=2) of 371.5 ± 271 ppm, a maximum of 563 ppm and a minimum of 180 ppm. Although there is a clear positive correlation between chlorine and fluorine (figure 5.14 a), this is not observed for more

evolved magma . Unlike Navidad MIs, Lonquimay MIs have a clear negative correlation between halogen elements and SiO_2. Furthermore, the negative correlation is steeper for chlorine than fluorine (figure 5.14 b and c), which is completely in contrast with the halogen behavior in Navidad MIs.

5.5.3. TRACE AND RARE EARTH ELEMENTS

Navidad MIs are enriched in incompatible elements compared to the primitive mantle. Multi-element diagrams show that large ion lithophile elements (LILEs) are more abundant than high field strength elements (HFSEs), displaying a trend reflective of subduction zones. Rb, K and Sr are the most enriched elements; Sr content in MIs is quite similar in every MI. Additionally, a strong depletion of Nb is observed, which is greater than the Nb depletion of the Navidad lavas bulk rock. Intermediate elements, such as Ce, Nd and Zr, have a broad area of enrichment. The Navidad bulk rock content seems to represent the average of the Navidad MIs content, with the exception of Nb, Sr and Ti. As previously stated, Navidad MIs have a strong depletion of Nb and Ti compared to the Navidad bulk rock (figure 5.15). On the other hand, Lonquimay MIs as well as Navidad MIs are more enriched than the primitive mantle, with Ba and K being the most enriched elements. Light elements are more enriched than heavy elements, which suggests that the data reflect a subduction zone setting. Lonquimay MIs show the same Nb depletion in contrast to the Navidad bulk rock data. The enrichment in Sr is normal for subduction zone rocks, although we can observe a slight depletion of Zr compared to other elements. Navidad MIs also show a slight enrichment in Sm and Ti. Finally, although Lonquimay data are fewer than that from Navidad, they seem to follow the same trend, and are very similar when compared to the Lonquimay bulk rock data (figure 5.15).

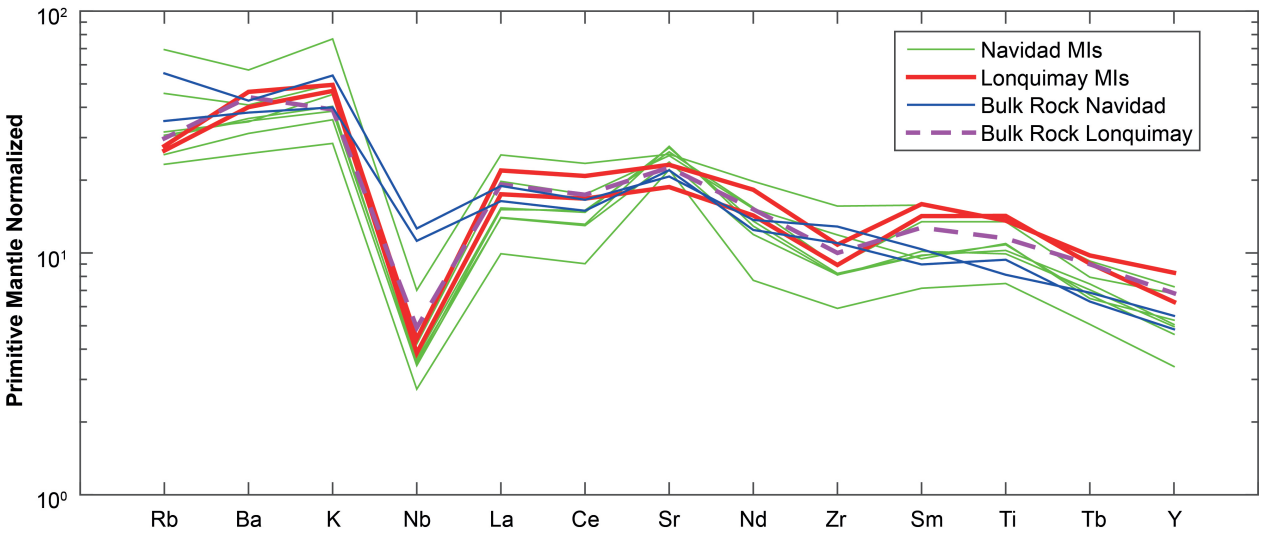

Figure 5.15: Multi-element diagram that showed enrichment of incompatible elements compared to the primitive mantle. We can observe a higher enrichment of LILE with respect to HFSE. The Nb negative anomaly stands out in the diagram as well as the Sr positive anomaly in Navidad MIs.

Regarding REE, the data show that heavy rare earth elements (HREEs) are 5 times more depleted than light rare earth elements (LREEs). Navidad MIs are the most enriched, with a negative Eu

anomaly similar to the Navidad bulk rock, a negative anomaly in Lu and a positive one in Yb. It is noteworthy that some MIs show a positive anomaly of Nd (figure 5.16). Lonquimay MIs are surprisingly more enriched than Navidad MIs, with slightly positive and negative Eu anomalies and a higher amount of HREE when compared to the Lonquimay bulk rock (figure 5.16).

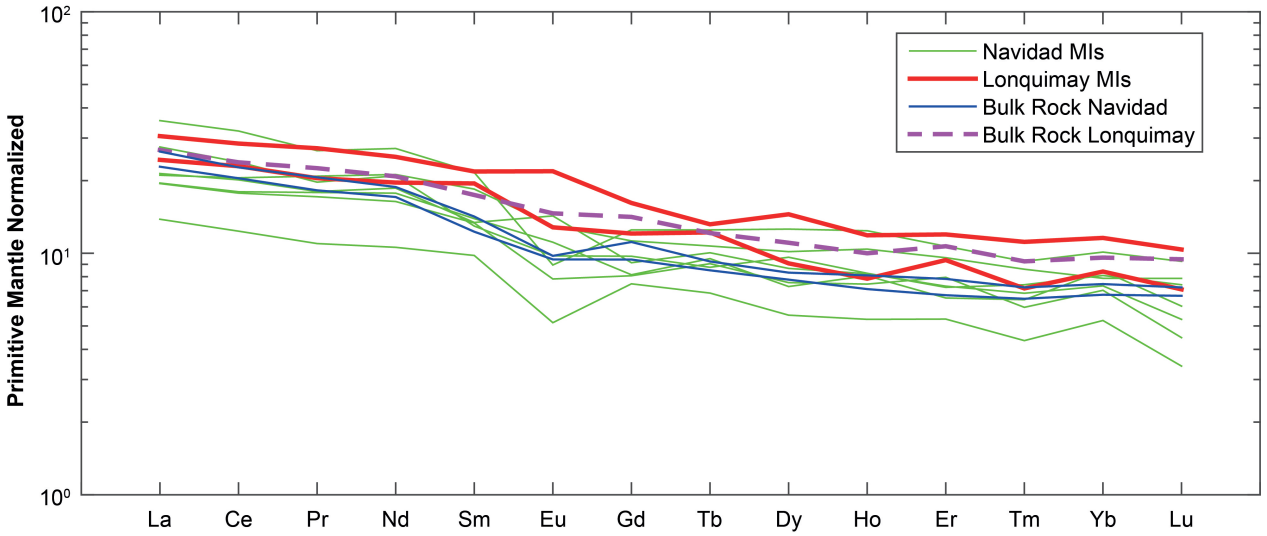

Figure 5.16: Rare earth element diagram, showing the slight enrichment of LREE over HREE. The Eu negative anomaly in Navidad MIs stood out among the others.

6

Discussion

6.1. ARE LONQUIMAY AND NAVIDAD LAVAS WATER DEPLETED?

MIs are widely accepted as a reliable representation of the original composition of the magma. This also applies to water composition. However, several researchers have shown water undergoes processes of equilibrium that modify the original water composition, thus, MIs can gain and lose water as the melt, which surrounds MI hosts, is exposed to a lower water fugacity (Lloyd et al. (2013)[50]; Portnyagin et al. (2008)[68]; Gaetani et al. (2012)[29]; Cannatelli et al. (2016)[12]). Results from this study show that MIs are water depleted. In order to properly interpret water content in MIs from this study, and unequivocally determine that magma from the LVC was water depleted at its source, we need to determine if the MIs did not undergo any re-equilibrium processes that may have modified their volatile content.

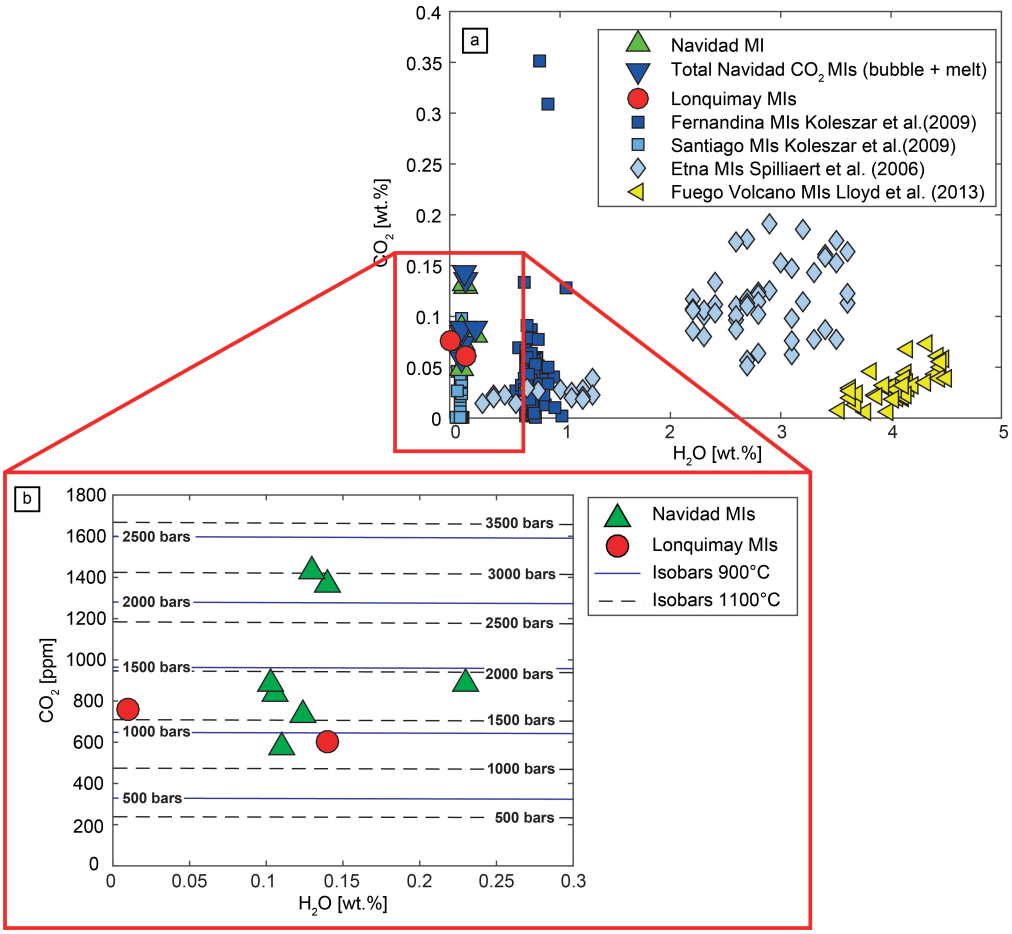

Figure 6.1: Water versus carbon dioxide diagram. a) Navidad and Lonquimay MIs have less water content compared to olivine-hosted MIs from other volcanic system. Lonquimay and Navidad MIs have the same water content as magma from hot spot environments, such as Santiago volcano located in Galapagos island (Koleszar et al. (2009) [44]). b) Navidad and Lonquimay CO_2 and water content. Isobars were calculated by means of the software Volatile Calc, by Newman and Lowenstern (2002)[60]. The richest and poorest CO_2 MIs have a calculated entrapment temperature of 1100 °C using the olivine-melt thermometer of Putirka (2008)[69]. Entrapment pressures are estimated by using the dotted lines. The lowest entrapment pressure for Navidad MIs is above 1 kbar and the highest is close to 3 kbars. Lonquimay MIs have entrapment pressures close to 1 kbar.

Basaltic arc volcanoes from the same tectonic setting as Navidad and Lonquimay have a surprisingly narrow range of water content of 4 wt.%, with s.d. ranging from 2 to 6 wt.%, measured in olivine-hosted MIs (Plank et al. (2013)[66]). Moreover, Etna and Fuego volcanoes have a ~ 3 wt.% and ~ 4 wt.% of water (Lloyd et al. (2013)[50];Spilliaert et al.(2006)[80]). On the other hand, ocean island basalts and mantle plume magmas have water amounts of 0.5 to 1.5 wt.%, while mid-ocean ridge basalts have 0.3 to 0.5 wt.% of water (Dixon et al. (2002)[22]; Edmonds and Wallace (2017)[24]). The Navidad and Lonquimay olivine-hosted MIs from this study are depleted in water, not exceeding 0.3 wt.%, which means they record the driest magma from arc volcanoes worldwide. The values of water concentration of our MIs is more similar to those from mid ocean ridge basalts or mantle plumes. For instance, water contents in MIs for Santiago volcano in the Galapagos islands is similar to the water content in Navidad and Lonquimay MIs (figure 6.1 a), but Santiago volcano is located in a very different tectonic setting (Koleszar et al.(2009)[44]).

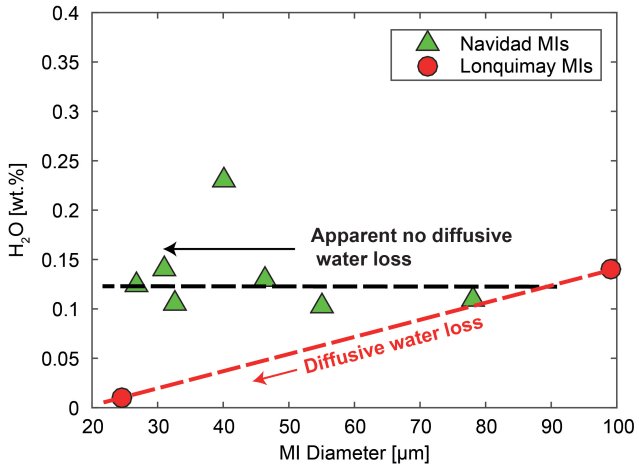

Figure 6.2: Water variation diagram vs MI long-axis diameter. Non-solid black lines represent Navidad trend that does not vary with the diameter, and non-solid red line resembles the Lonquimay water variation trend that varies as long-axis is modified. Positive correlations are likely linked to diffusive water loss (Cabral et al.(2014)[10].

The possible causes for the water depletion in Navidad and Lonquimay MIs could be mainly due to: 1) water loss; 2) degassing of the system; and 3) a water-depleted magma source. In pioneering studies in the past, researchers considered MIs as isolated systems, capable of representing the original magma compositions (Roedder 1979[71]). Nowadays, it is an accepted concept that MIs, especially those that are olivine-hosted, do not behave as closed systems and could lose or gain water through diffusion of H^+ (Gaetani et al. (2012)[29]). The variation of water (gain or loss) can reach 4 wt.% (Gateani et al. 2012[29];Lloyd et al. 2013[50]). Unraveling whether MIs have suffered re-equilibrium by water loss or not is a convoluted matter. Water diffusion in MIs is controlled by several variables, with one of them being the size of the melt inclusion. When MIs have not suffered water diffusion, there are no differences in the water amount whether it is a larger or a smaller MI. Nonetheless, smaller MIs lose water more quickly than larger ones. Therefore, during the process of losing water, larger MIs seem to have more water than smaller ones, as can be observed in plots of water vs MIs size (Cabral et al.(2014)[10]). In figure 6.2, we show that water concentration in Navidad MIs does not vary with MI size. This might point

out that Navidad MIs have not experienced any water loss. Another possible explanation of those trends is a complete water re-equilibration with the surrounding environment (i.e. the host). Nonetheless, Lonquimay MIs do show a positive correlation between water content and MIs size, suggesting that, for the Lonquimay stratocone, MIs may have been modified by water loss and therefore the measured water content does not represent the original amount in the magma.

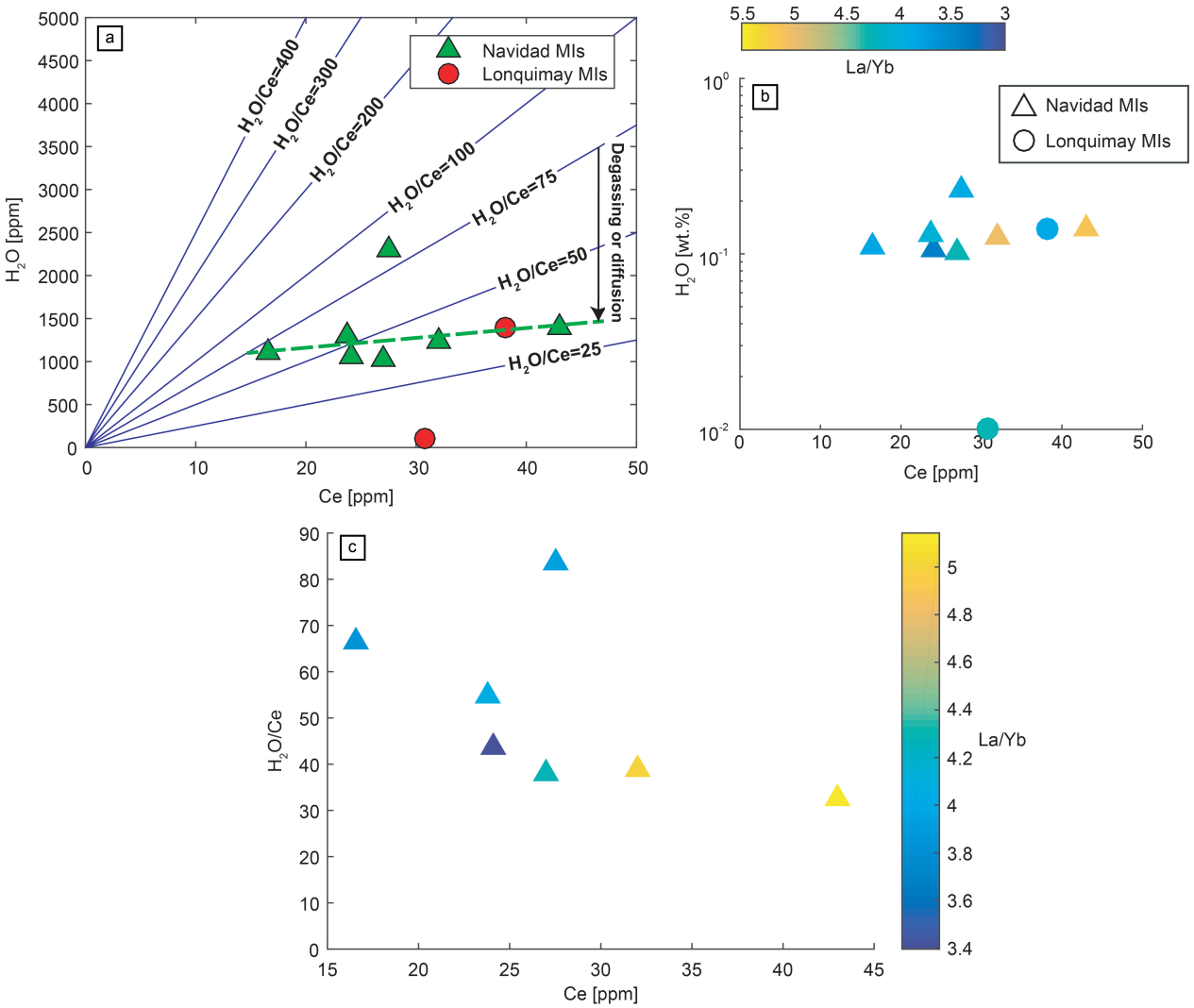

Figure 6.3: Water and Ce variation diagram. Navidad and Lonquimay lavas have H_2O/Ce equal to 14 and 110, respectively. Navidad MIs do not have a positive correlation among the data. Lonquimay MIs have a positive correlation, but with a shift from the main lines. On the other hand, c) shows that the variation of H_2O/Ce depends mainly on Ce, since H_2O remains almost constant in Navidad MIs. We did not plot Lonquimay MIs in this graph, as they do not show any important variation.

Another proxy to assess water diffusion in MIs is the correlation between water and Ce. These two species share similar partition coefficients that allow them to have a coupled behavior (Hartley et al.(2015)[36]). Thus, as magma becomes more evolved, the H_2O/Ce ratio remains constant until water and magma separate. However, Navidad MIs display a decoupled behavior for H_2O

and Ce: as Navidad MIs raise its Ce content, water remains almost unchanged 6.3, i.e. Navidad MIs have a non-positive correlation between H_2O and Ce. This lack of positive correlation could be caused by either water loss, through diffusion, or a Ce compatible behavior due to a high oxidation state of the magma. We can discard a Ce problem because we have not found any geochemical evidence for a highly oxidized magma. Ce has two oxidation states, Ce^{3+} and Ce^{4+}, but Ce^{4+} is compatible with mineral phases such as zircon (Trail et al. (2012)[85]; Neal and Taylor (1989)[59]), so Ce^{4+} can be incorporated more easily into minerals than in the melt. Hence, we would expect to observe an anomaly in normalized REE and $Ce/Ce^* < 1$ ($Ce/\sqrt{La_N xPm_N}$), but there is no such anomaly in the REE diagram for our samples 5.16 and every Navidad MIs has $Ce/Ce^* > 1$, implying that there is a less oxidized magma and an incompatible Ce behavior. Therefore, Ce behaves as it is expected and water loss through diffusion might be the most probable process . Lonquimay MIs do not show a clear trend, although in 6.3 they seem to have a positive trend, as H_2O/Ce varies a lot, suggesting a lack of clear tendency associated more to degassing processes than only diffusion.

Experimental data shows that more depleted magma (low La/Yb) may have higher H_2O/Ce values (Hartley et al. (2015)[36]), but as we can observe in figure 6.4 a, the negative trend between La/Yb ratios and H_2O/Ce ratios suggest that for Navidad MIs , high La/Yb MIs have less H_2O/Ce than enriched MIs. Additionally, Navidad MIs with high La/Yb contain the highest amount of Ce, showing a normal Ce enrichment trend. Thus, highLa/Yb and Ce-rich MIs might have lost a considerable amount of water, while lowLa/Yb and Ce-poor MIs might have either preserved its water content or lost only a small amount. Likewise, if degassing is indeed the cause of water loss, the H_2O/Ce ratios would not correlate with any of the incompatible elements. Nevertheless, the H_2O/Ce decrease in our data is strongly controlled by the Ce increase (figure 6.3 c), which means that the water degassing process is unlikely. Furthermore, the final water content after degassing, would be more scattered than what is shown by our data, (Koleszar et al. (2009)[44] which displays a $H_2O - Ce$ trend relatively flat. We suggest that the H_2O/Ce decrease shown by our data is more likely linked to a PEC water loss, such as water diffusion, than a water degassing process. Either fractional crystallization or magma mixing could explain a change in the H_2O/Ce ratio although Hartley et al. (2015)[36] suggest that neither magma mixing nor fractional crystallization may explain the H_2O/Ce ratios because each of both options would maintain a constant ratio. The H_2O content in Navidad MIs show a slight decrease, likely due to Ce, since degassing of water would have a more scattered decrease (figure 6.3 c). Therefore, we conclude that the low water content in Navidad MIs might be explained by a water loss through H^+ diffusion.

Hartley et al. (2015)[36] reconstructed the original water composition of MIs in a representative Iceland volcano by using H_2O/Ce values (H_2O/Ce=180) obtained from multiple studies. Although there is a lack of similar studies for LVC and the SVZ, we applied the same methodology, well aware of the possible errors associated with this approach. We could not use in our recalculations data from the literature for other arc volcanoes, such as those from the Cascades and Guatemala (figure 6.4 c and d), because there is no indication that Navidad MIs could have the same amount of water. We selected our highest H_2O/Ce ratio (82.14), which most likely represents the original H_2O/Ce trend, and we estimated a maximum water loss of 0.2 wt.% for Navidad MIs, with a new water mean of 0.2276 wt.% with σ= 0.0676 wt.% (figure 6.5 b). The highest H_2O/Ce ratio obtained for Navidad MI is very interesting, as it is lower than numerous

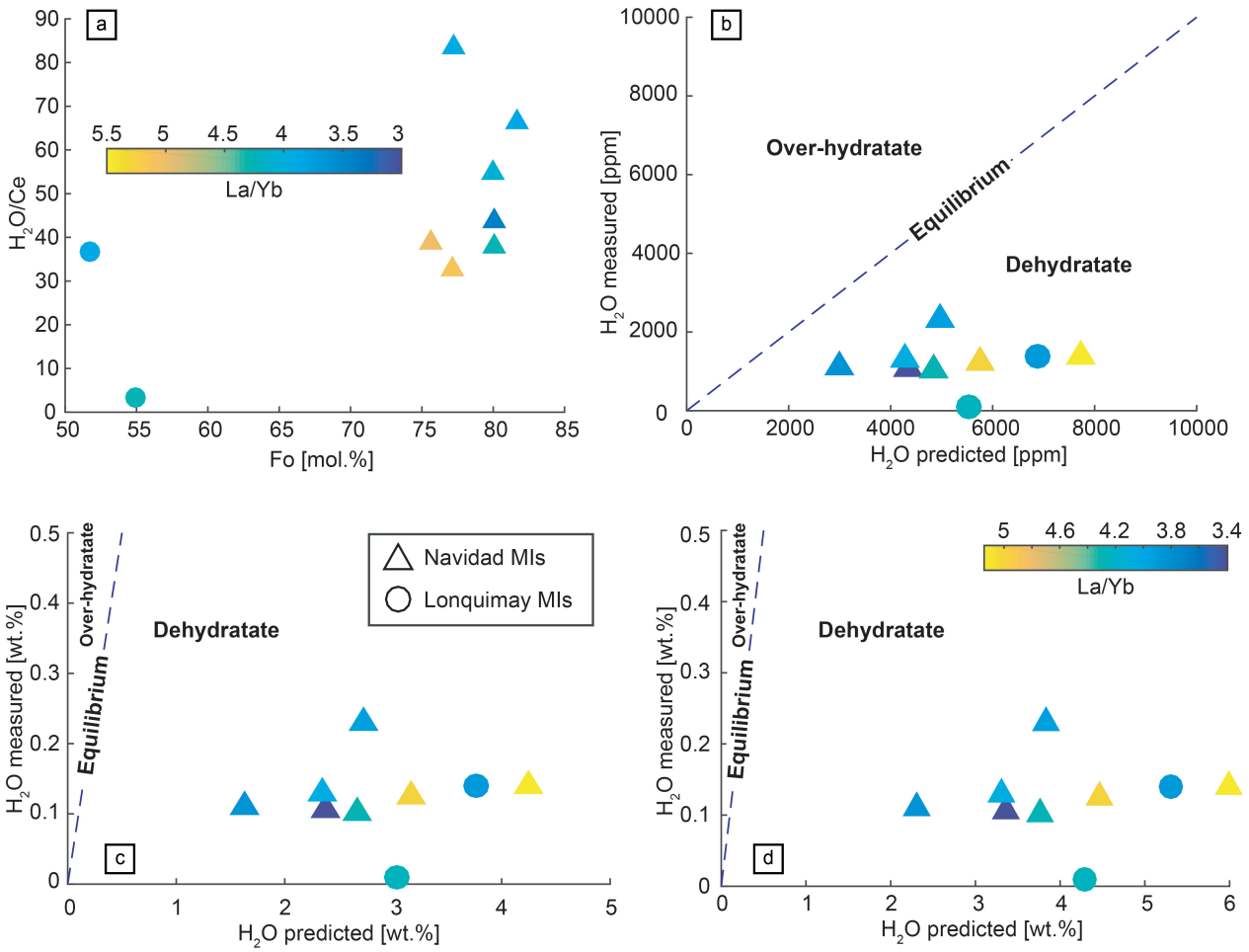

Figure 6.4: a) H_2O/Ce vs Fo content and La/Yb variation, showing a similar Fo content with different H_2O/Ce ratios for Navidad MIs and a lower H_2O/Ce ratio for Lonquimay MIs. b) Estimated H_2O content, calculated using $H_2O/Ce = 180$, where Ce is assumed to be a known quantity, which represents the theoretically amount of water versus the measured H_2O. The value 180 is taken from Icelandic volcanoes (Hartley et al.(2015)[36]). MIs that plot below the non-solid line most likely have experienced a loss of water, while MIs that plot over the line are overhydrated. MIs that plot on the line represent the original H_2O/Ce ratio. c) Same diagram as b), but with a H_2O/Ce ratio of 988, which represents the Cascades volcanic chain. The legend put on the upper right part is shared with diagrams b), c) and d). d) Same diagram as b) and c), but with a H_2O/Ce ratio of 1393, representing Guatemalan volcanoes. Among them, we can find Fuego volcano. The color bar of La/Yb is shared with diagrams b), c) and d).

arc volcano values in the literature (Cooper et al. (2012)[16]) and it is even smaller than the driest magmas such as OIB. Moreno and Gardeweg (1989)[55] described that during the Navidad eruption, a 5km-high plume expelled water vapor into the atmosphere, as the main proof of a degassing event. The water degassing event likely occurred after H_2O was trapped within MIs, and therefore Navidad MIs might partly represent the original water content of magma, which most likely had a depleted source.

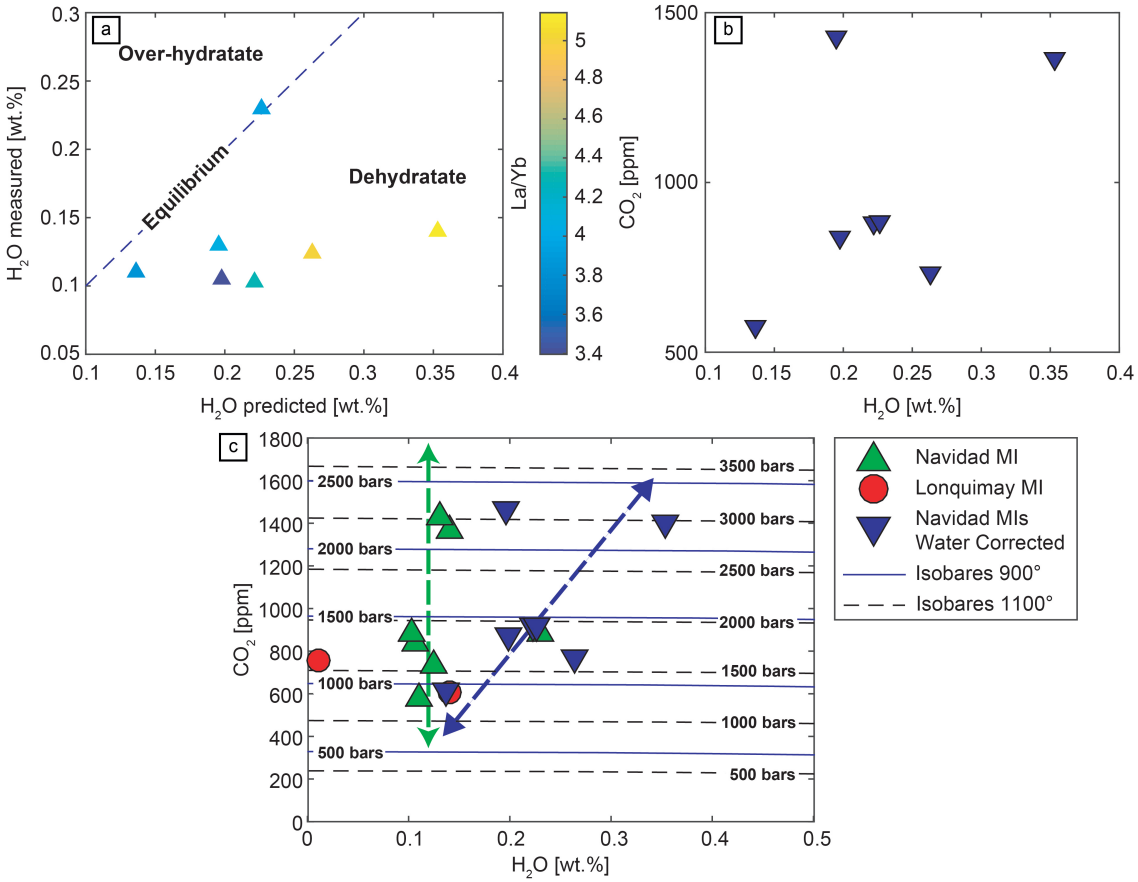

Figure 6.5: a) Navidad MIs corrected by H_2O/Ce ratio of 82.14 which is the highest ration in Navidad MIs. Although MIs recover almost the double of their water, the corrected water keep being negligible. b) Corrected Navidad MIs on a plot water and CO_2. c) Comparison between non-corrected and corrected Navidad MIs on a plot with isobars calculated by means of VolatileCalc (Newman and Lowenstern (2002)[60]. Green dot line represent the main trend of non-corrected Navidad MIs which is similar to open system degassing and blue dot line represent the main trend of water corrected Navidad MIs which might resemble a closed system degassing.

The lowest entrapment pressure for an MI can be estimated using Henry's law. Independent of water content, we determined that the lowest entrapment pressure is over 750 bars (figure 6.1 b and figure 6.5 c). Studies on $H_2O - CO_2$ solubility show there is a dependence on pressure (Wallace et al. (2005)[87]; and citations therein) such that at 750 bars, magma may contain between 2 and 3 wt.% of water, which is way higher than the water content of Navidad MIs. Therefore, neither water degassing nor water diffusion have significantly affected the original water content of Navidad MIs, suggesting that the Navidad magma had a water-depleted origin.

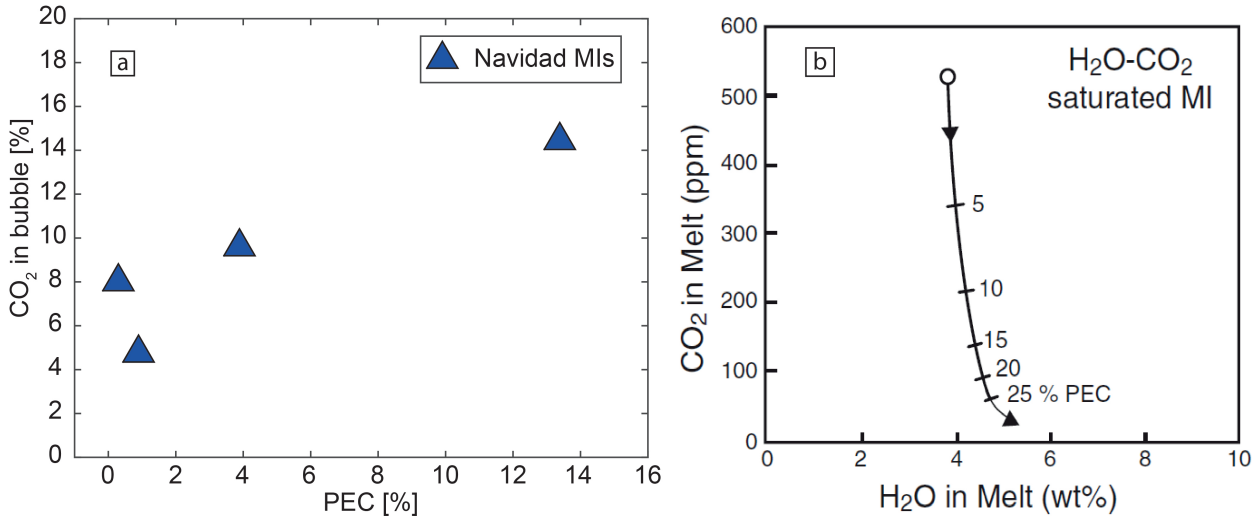

Figure 6.6: a) This picture shows a positive relation between PEC and CO_2; b) CO_2 and H_2O variation as a fucntion of PEC, modified from Steele-MacInnis (2011)[81].

6

Recent studies have determined that bubbles of MIs can contain between 40% to 90% of the total CO_2 (Moore at al. (2015)[54], Cannatelli et al. (2016)[12], Esposito et al. (2018)[26]). Raman spectroscopy data of Navidad MIs show a maximum of 15% of CO_2 within the bubble, with the vast majority of CO_2 measured in the melt (up to 1400 ppm), in contrast with previous studies. We discarded a sample due to possible carbon coating contamination, as figure 6.7 shows a clear correlation among CO_2 and various incompatible elements and not a scattered one, which would be the result of contamination. Another explanation linked the post entrapment crystallization with the amount of CO_2 in the bubble. Steele-MacInnis et al. (2011)[81] suggested that the post-entrapment crystallization process can modify the amount of CO_2 in the bubble of a MI, so they developed a numerical model that predicts a CO_2 decrease from the melt into the bubble as PEC degree increases. A greater PEC degree in MIs leads to a larger amount of CO_2 that migrates into the bubble (figure 6.6); the opposite happens when the PEC is smaller. Our data show a PEC degree of up to 13.4 %, which is related to the highest amount of CO_2 in the bubble, and. smaller PEC degrees correlate with lower CO_2 concentrations in the bubble (table 6.1). Additionally, Moore et al.(2015)[54] determined that the CO_2 diffusion coefficient is greater when the MI has a greater water content and temperature. In water depleted melts with colder glass temperatures, such as those represented by our olivine-hosted MIs, the CO_2 flux from the melt into the bubble is hindered, leading toa very small amount of CO_2 migrating into Navidad MI bubbles.

Carbon dioxide is the second most abundant species in volcanic systems after water. It is well known that it behaves as an incompatible element. Moreover, it exsolves before water. Researchers have linked CO_2 to Nb, as was done with H_2O and Ce, to understand its behavior within magmas (Saal et al. (2002)[75]; Hauri et al. (2018)[38]). This relationship gives insight on degassing processes and source compositions and it can be applied to water in order to deepen the understanding of water depletion. The mean CO_2/Rb,CO_2/Ba and CO_2/Nb ratios of Lonquimay and Navidad MIs were 44.39 ± 15.67, 3.71 ± 1.02 and 341.99 ± 101.29, respectively. In figure 6.7, the relationship among those elements and CO_2 remains relatively constant. Rb, Ba

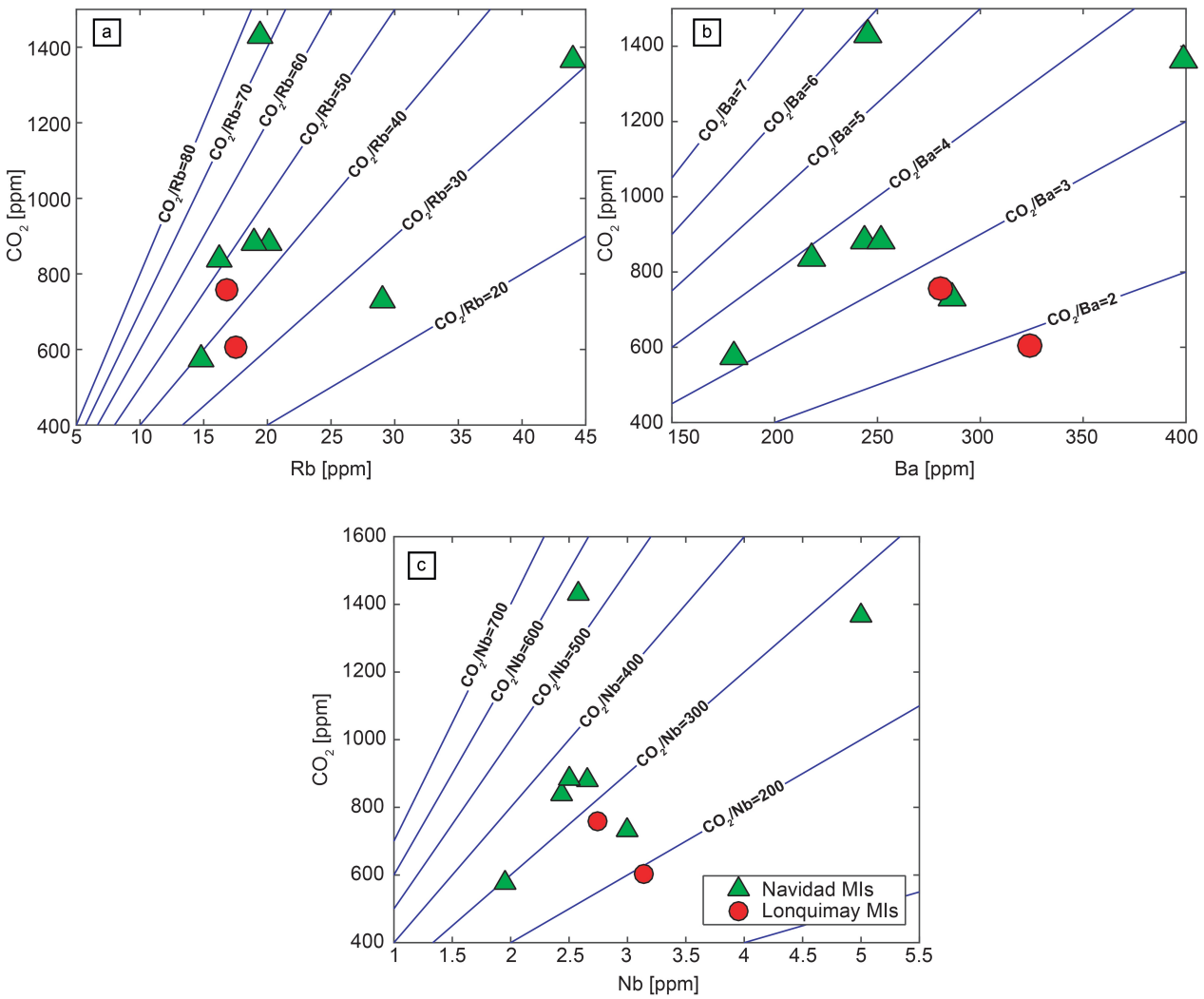

Figure 6.7: a) Plot of CO_2 vs Rb, where the ratio follow a roughly constant slope; b) CO_2 vs Ba, with more scattered ratios; and c) CO_2 vs Nb with an almost constant slope close to 300, which is a value very similar to MORB.

and Nb are highly incompatible elements but, unlike CO_2, they remain within the melt. Consequently, figure 6.7 a), b) and c) may suggest that CO_2 has not been lost during trapping into a MIs, and thus represents a correlation without degassing. In fact, a marked positive correlation of those elements can be linked to undegassed MIs (Saal et al. (2002)[75]; Matthews et al. (2017)[51]; Hauri et al. (2018)[38]). Furthermore, an opposite trend, i.e. a negative correlation, has been widely interpreted as a degassing process (Koleszar et al. (2009)[44]; Salem et al. (2019)[76]). Interestingly, CO_2/Rb and CO_2/Ba in Navidad MIs have lower values than Icelandic volcanoes, which is in agreement with the tectonic setting where we may expect a larger amount of Rb and Ba due to the slab contribution and small fusion rates. Nonetheless, CO_2/Nb is similar to the value found by Hauri et al. (2018)[38] of 391. This may be explained since the subducting slab did not contribute additional CO_2 to the system and and the amount of Nb is similar. The former is supported by the fact that the CO_2/Nb ratio and Nb content fit in the DMM field of Mironov et al. (2015)[53]. Conversely, the plot of H_2O vs. CO_2 shows a degassing path for Navidad MIs (figure 6.5 c and 6.1 b)) similar to the one described by Dixon et al. (1995)[21] d. However, whether H_2O MIs are corrected by water diffusion or not, they display a degassing path. Furthermore, non-corrected Navidad MIs seem to follow an open system degassing path and corrected MIs reflect closed system degassing. Additionally, Navidad MIs display a variability in CO_2 content that Wallace (2005)[87] suggested as proof of subtle degassing. These results contrast sharply with the positive trend of CO_2 with Rb, Ba and Nb that reflect an undegassing process 6.7. The abovementioned arguments make it more difficult to explain whether a depletion is caused by degassing or diffusion of water, but both can be related to each other when degassing is affecting an already water-depleted magma. Gaetani et al. (2012)[29] reported that water depleted MIs undergoing a degassing process may be easily mistaken for MIs undergoing a diffusion process caused by the olivine H^+ permeability. When Navidad MIs were corrected with the highest H_2O/Ce ratio, the increase in water was insignificant, in agreement with Gaetani et al.(2012)[29]. The previous result strongly suggests that Navidad MIs are formed by a water-depleted magma. Lonquimay MIs seem to have lost an important part of their water content through degassing and therefore it is not possible to precisely assess the real water content of the Lonquimay stratocone magma.

Melt Inclusion	CO_2 in melt [ppm]	CO_2 in bubble [ppm]	Bubble CO_2 in MI [%]	Bubble volume in MI [%]	PEC [%]
NV18.O.AK_MI_01	813	71	8.7	4.0	0.3
NV19.O.19_MI_02	1293	137	8.7	6.3	3.9
NV19.O.13_MI_01	492	83	15	4.6	13.4
NV19.O.07_MI_01	1300	65	5.5	3.8	0.9

Table 6.1: Carbon dioxide calculated from bubbles in Navidad MIs. The total amount of CO_2 in bubbles is between 5 to 15 % of the total CO_2. The methodology used to make these calculations is based on Esposito et al. (2011)[25] and Steele-MacInnis et al. (2011)[81].

Our samples of Navidad lavas represent the last phase of the eruption, so one may think that this is the reason why the magma that formed Navidad lavas is water depleted. However, at the time of MI trapping, neither CO_2 nor fluorine had exsolved from the melt, suggesting that the

source of the depletion is at greater depths. Additionally, olivine form and habit show a high crystallization temperature and slow cooling rate which indicates that the entrapment of these minerals did not occur during the eruption. Therefore, although Navidad lavas represent the last eruptive stage of the eruption, its olivine-hosted MIs are reliable chemical recorders that can be used to assess the pre-eruptive volatile content in the source magma.

6.2. ANOMALOUS HIGH HALOGEN CONCENTRATION

A recompilation of data by Webster et al. (2018)[90] and Aiuppa et al. (2009)[1] (an cites therein) show basaltic andesites and andesites in subduction zones have compositions ranging from 50 to 900 ppm and 100 to 8500 ppm for F and Cl, respectively. Both Navidad and Lonquimay MIs have average Cl and F concentrations within the reported range, with only one MI with F concentrations above the reported limit. Kendrick et al. (2017)[41] show that OIB and MORB have values of Cl/K close to 0.06, while both Lonquimay and Navidad MIs show values far higher (0.16 ± 0.03 and 0.11 ± 0.10 for Navidad and Lonquimay, respectively). These ratios show high values for Cl, three times higher than mantle values, although higher K content MIs show lower ratios. A common and useful approach to explain the origin of the high Cl content at Lonquimay and Navidad is to consider the F/Cl ratio following Kendrick et al. (2018)[43]. Our F/Cl ratios are close to the value for the mantle, although there is little enrichment in Cl, which might be explained by the contribution of the subducting slab to the volatile content as MIs seem to plot towards the seawater line (figure 6.9 a). Our results also rule out continental or oceanic crust contamination, as we should expect either lesser amounts of Cl or higher values of F if the continental crust was the source. Moreover, Polanco (2010)[67], based on Pb, Nd and Sr isotope measurements in whole rocks, determined that continental crust contribution is minor at the LVC (figure 6.9 a), as also shown by the high negative anomaly of Nb (figure 5.16)(Rollinson (2014)[74]). We suggest that the halogens source may be the mantle itself with contributions from the subducting slab (figure 6.9 a), as Cl/K and F/Nd remain constant regardless of Cl degassing and little Nd enrichment of Navidad MIs. Two Navidad MIs have ratios that could represent input from either oceanic or continental crust, since their high fluorine content and low Cl/K_2O ratios suggest a minor crustal influence on the halogens composition. Therefore, the halogen sources may likely be the mantle with a subducting slab contribution, and according to Kendrick et al. (2011)[42], halogen and noble gasses can be easily released into the mantle without major lower continental crust contamination.

Petrography of Navidad lava samples reveal the presence of apatite, which is an important mineral since it incorporates volatiles such as OH, Cl and F into its structure and it might be useful to constraint those volatiles (Palma et al. (2019)[62]; Webster and Piccoli (2015)[89]). Robbiano (2017)[70] reported the presence of fluorapatite associated with Fe oxides and within olivine-hosted MIs from Navidad cone. This fluorapatite has no Cl in its structure, and it might be classified as a mantle magmatic apatite (O'Reilly et al.(2000)[61]). Its composition would not affect the Navidad magma fluorine composition because it would be itself the origin of fluorine. Now, whether it was crystallized from the magma or not, it is not entirely clear, but the original total fluorine content would be modified and the F/Cl ratios might vary, suggesting there has been continental crust contamination. Apatite was also found in Lonquimay lavas (Polanco (2010)[67]).

The ratios of F/Cl range from 0.2 to 1.02, with the mode close to 0.5 (figure 6.9). González-Ferrán et al. (1989)[35] measured fluorine in tephra as a proxy for plume gas values. They measured a value of 1638 ppm of F in a lava block, F/Cl ratios ranging from 0.5 to 2, a value of 180 ppm of F in tephra 2km from the crater and 3400 ppm of F in tephra 11 km from the crater , determining that the finest and furthest tephra samples recorded the highest concentration of dissoluble fluorine.Araya et al. (1990)[2] and Araya et al. (1993)[3] reported fluorosis in cattle

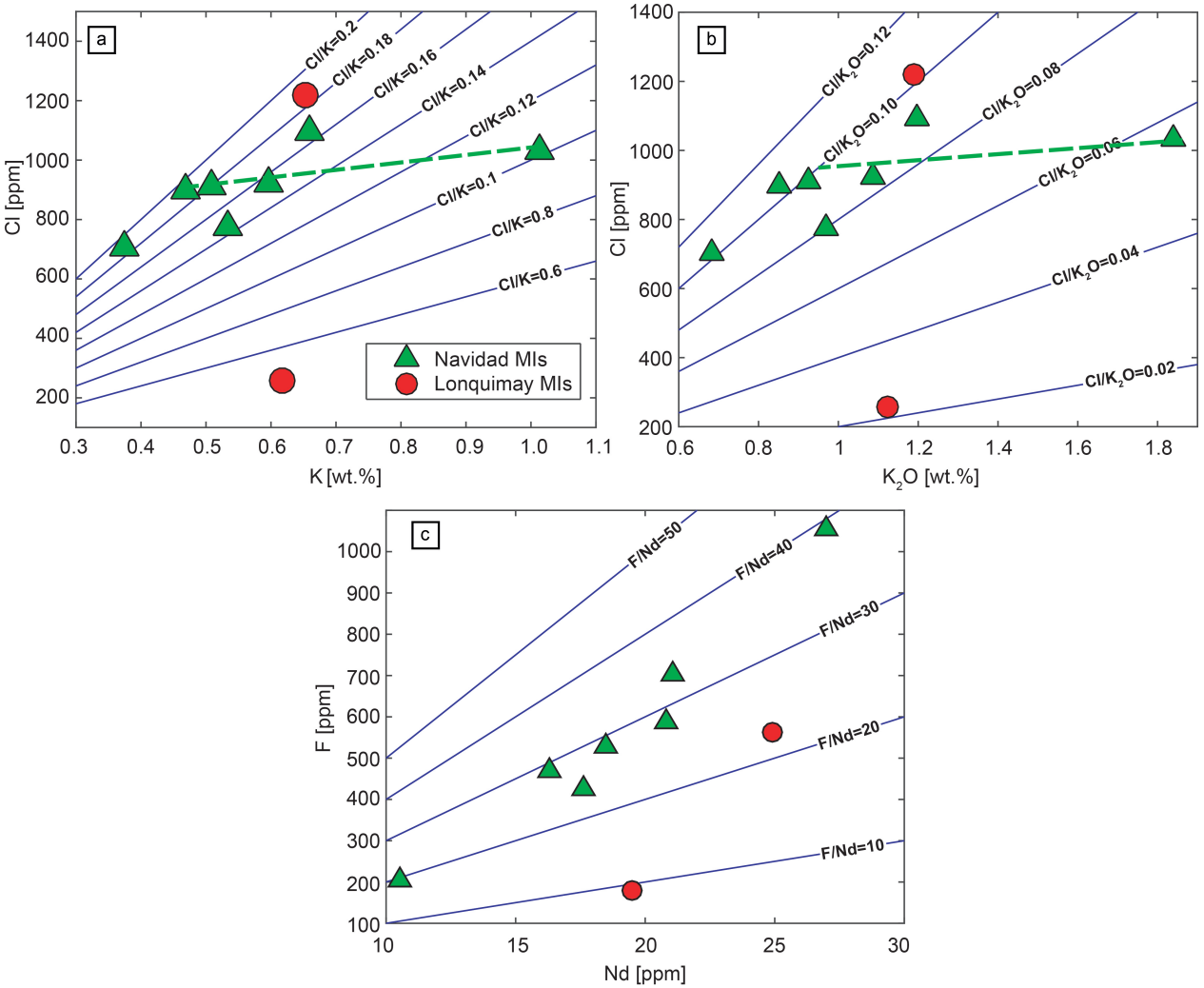

Figure 6.8: Halogens are usually coupled to other incompatible elements. Cl is paired to either K or Nb and F to Nd. a) Cl vs K plot shows an initial ratio of 0.18 that suddenly decreases to 0.1, which represent a Cl degassing process. b) Cl vs K_2O, showing a similar decrease as a). The ratio Cl/K_2O of 0.06 represents MORB compositions, and the MIs are therefore highly enriched. c) F vs Nd shows a non-degassing process but a highly incompatible behavior. Similar to Cl, F is enriched compared to MORB values.

close to the LVC which they linked to the 1988-1990 Navidad cone eruption. Immediately after the eruption, they measured 315 ppm of F in grass (Araya et al. (1990)[2]) and two years after the eruption ended, they measured 6.9 to 34 ppm of F (Araya et al.(1993))[3]Etna volcano in Italy is famous for similarly emitting huge amounts of fluorine into the atmosphere as HF (Francis et al. (1998)[28];Bellomo et al. (2007)[4]). During the 2001 eruption, Etna released volcanic ash that had a leached F concentration ranging between 15 and 476 ppm, adding roughly 85% of F to top soils and vegetation (Bellomo et al. (2007)[4]. Concentrations of F recorded by the 2001-eruption olivine-hosted MIs are closer to 940 ppm (Collins et al. (2009)[14]; Metrich et al. (2004)[52]), similar to the Navidad MIs.

If we were to compare Etna volcano with the Navidad cone, we would encounter several similarities. Based on soluble F on foliage, Etna erupted the same amount during the 2001 eruption as the Navidad cone erupted in 1988-90. The amount of F measured in volcanic ash though differs considerably, as Navidad volcano has roughly 7 times more F in volcanic ash than Etna in 2001. However, Navidad ash data are not as accurate as we think. Two values of soluble F have been published, one measured on coarse ash close to the crater (180 ppm) and the other on fine ash at a considerable distance from the crater (3400 ppm) (González-Ferrán et al. (1989)[35]). Witham et al. (2005)[91] in their review discussed the methodology applied to leaching volcanic ash. They concluded that soluble F in the finest-sized ash located furthest from the crater might be overestimated, and not representative either of the plume nor the magma. Fine ash has a higher surface area for F to attach to than bigger blocks. In addition, fine ash may travel larger distances than coarse ash, which extends the time that particles interact with fluorine gas. Another source of problems is the lack of the water proportion used in the leaching process. We must acknowledge the latter since different water ratios may generate discrepancies in the results when measuring soluble elements (Witham et al. (2005)[91]). Unfortunately, it is not possible to extract this information from Gonzaléz-Ferrán et al.(1989)[35], as the authors do not mention any detail about the methods used for the leaching process. A better and more reliable method is to use the F/Cl ratios, which can better represent the relationship between both gases within the plume (Witham et al.(2005)[91]). Lower ratios are similar to Cl non-degassed ones found for Navidad MIs, but higher ratios in Gonzaléz-Ferrán et al.(1989)[35] might be influenced by the problem of overestimating the fluorine content. Therefore, the highest values in Gonzaléz-Ferrán et al.(1989)[35] are not comparable to our olivine-hosted Navidad MIs values, and lower values are expected to be similar to those found in MIs. Lower F/Cl ratios in the Navidad plume are similar to the Navidad magma, thereby suggesting that a roughly 500ppm-fluorine-bearing magma was erupted from the Navidad Cone. Interestingly, MIs from the 2001 eruption at Etna have surprisingly similar ratios as the Navidad MIs ($F/Cl = 0.58$) (Metrich et al. (2004)[52]). Regardless of the average fluorine composition of the magma (500ppm) or the volcanic ash (3400ppm), the Navidad eruption produced a high fluorine concentration on foliage and fluorosis in cattle, making the mere presence of F in magma enough to be a hazard for the surrounding population and environment.

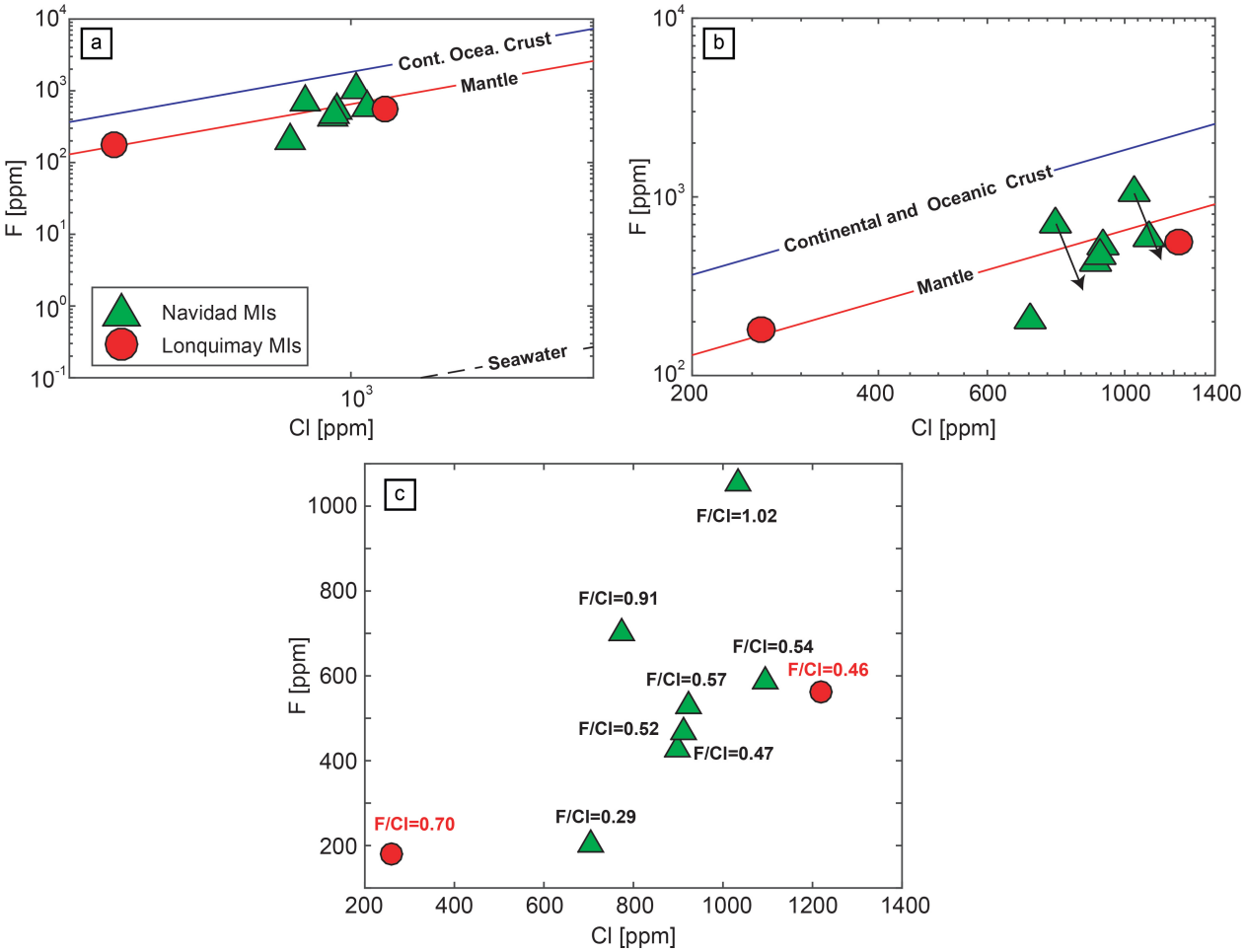

Figure 6.9: F and Cl variations. a) Logarithmic plot of F vs Cl, which shows values for MIs that are almost over the mantle ratio, with a slight contribution from seawater. b) Zoom of a), where it is easy to notice the slight contribution of seawater and the closeness of MIs to mantle ratios. MIs indicated with arrows are those that have experienced a Cl degassing. c) Linear plot of F vs Cl, where it is also shown the specific ratio of every MI. Lonquimay MIs are in red , while Navidad MIs are in black.

6.3. PRESSURE-RELEASE MELTING AS AN EXPLANATION TO WATER DEPLETION

Arc magmas tend to be enriched in water, with a common composition of 4 wt.% (Plank et al. (2013)[66]). Water depleted arc magmas are rare and in the literature, only one example is available, the Gallungung volcano in Indonesia. The water content in olivine-Fo_{91-88}-hosted MIs from Gallungung range from 0.21 to 0.34 wt.%. In addition, Cl concentrations are up to 700 ppm, reflecting melting with slab fluid enrichment, and CO_2 content is up to 750 ppm (Sisson and Bronto (1998)[78]). In comparison, Navidad MIs have similar values for water, Cl and CO_2 when they are corrected (see values above). Additionally, MgO in Gallungung volcano MIs is approximately 4 wt.%, similar to Navidad MIs, where it varies from 1 to 6 wt.%. Sisson and Bronto (1998)[78], based on work performed by Davies and Stevenson (1992)[19] and Draper and Johnston (1992)[23] on anhydrous high-Mg-Mariana-like basalts and low-K Cascade basalts with very low pre-eruptive H_2O, determined that the water depleted MIs in Gallungung volcano are formed at high temperature in shallow sub-crustal levels. They suggest that a process of mantle upwelling and pressure-release melting of hot peridotites may be an explanation for those phenomena. Similarly, pressure-release melting could be a possible explanation for Navidad-MI water depletion. Pérez-Flores et al. (2017)[64] determined "a local extension at the Lonquimay releasing bend structure within the LOFS and/or locally low lithospheric pressure" which promotes the ascent of melts (Pérez-Flores et al. (2016)[63] and cites therein). These structures might decompress the sub-cortical mantle, promoting a mantle upwelling that may allow water-depleted magma to reach the surface.

7

CONCLUSIONS

7.1. CONCLUSIONS

In this study, we petrographically described and analyzed olivine-hosted melt inclusions (MIs) belonging to Lonquimay and Navidad lavas. We measured and determined major and minor elements, as well as volatiles and REE through Electron Microprobe, Raman spectroscopy, and Secondary Ion Mass Spectroscopy, respectively. Lonquimay and Navidad lavas are basaltic-andesitic in composition and are composed of olivine, clinopyroxene, plagioclase and ulvospinel. Olivines from Navidad lavas are higher in Fo than olivines from Lonquimay olivine. Melt inclusions are basaltic to trachy-andesitic in composition, with Navidad MIs being more primitive and having lower K_2O contents than Lonquimay MIs. REE patterns resembled those from arc volcanism.

On the other hand, both Lonquimay and Navidad MI presented water depletion compared to arc volcanic MIs worldwide. Furthermore, their water content resembled more to mantle plume volcanism than arc magmas. Nonetheless, it was not demonstrated that Lonquimay MI water content resembled the original as long as many authors have reported water loss from olivine-hosted melt inclusion. In addition, it was not possible to assess water degassing in Lonquimay MI since there were few data. Conversely, it was shown that water depletion in Navidad MIs resembled the original MI water content. Thus, it was corrected Navidad MIs for water diffusion through Ce content and this correction pointed out to negligible water diffusion. In the same way, it was assessed that water degassing was also negligible. Hence, Navidad MI had a water depleted source.

Both Lonquimay and Navidad MIs show water depletion compared to arc volcanic MIs worldwide. Furthermore, their water content more resembled that of mantle plume volcanism than arc magmas. Nonetheless, we could not assess that Lonquimay MI water content represented the original content, as it may have been affected by water loss, a process that many authors have reported as common for olivine-hosted MIs. In addition, it was not possible to assess water degassing processes for Lonquimay magma, since we have limited data. Conversely, we show that Navidad MIs did not experience any water diffusion or degassing processes and therefore represent the pre-eruptive volatile content of the Navidad magma, which had a depleted water source. The CO_2 content in the magma was estimated from Navidad and Lonquimay MIs by using Raman spectroscopy (in the bubble phase) and Secondary Ion Mass Spectroscopy (in the glass phase). Even if Lonquimay MIs show poor statistics (few points), their composition show high CO_2 contents and a pressure entrapment of at least 1000 bars (about 3 km). Navidad MIs show CO_2 contents ranging from 500 ppm to 1400 ppm, representing minimum entrapment pressures, from 1000 bars to roughly 3000 bars (8-10km). CO_2, Ba, Rb and Nb plots show an incompatible behavior of CO_2 and a process of non-degassing. However, this is in contrast with the CO_2 and H_2O plot, where the trend can be interpreted as open system degassing. Recent studies have suggested that water diffusion in water depleted magmas may be confused with volatile degassing processes (Gaetani et al. (2012)[29]; Moore et al. (2015)[54]), which led us to the conclusion that our trends of CO_2 and H_2O contents reflect a water-depleted magma source.

So, how can arc volcanos have a water depleted source? The answer is convoluted and obscure. Moreover, data worldwide suggest that Navidad MIs may represent the driest magma

ever recorded in the Southern Volcanic Zone. Although our data are similar to another volcano, Galunggung in Indonesia, which has a water depleted source with water contents between 0.21-0.38 wt.% and CO_2 contents up to 750 ppm (Sisson et al. (1998)[78]), the tectonic setting is different. The abovementioned studies on Galunggung volcano propose a mantle upwelling source as the cause for magma water depletion. We suggest that this is possible in the LVC, where local extension has been documented (Pérez-Flores et al. (2017)[64]; Pérez-Flores et al. (2016)[63]), and specific to the Navidad eruption, small scale mantle upwelling may have favored the rising of extraordinary water-depleted magma.

The environmental impact of the Navidad eruption was disastrous, causing the death of cattle close to the LVC area due to the high fluorine content. Araya et al. (1990)[2] and Araya et al. (1993)[3] reported fluorosis in cattle as well as high fluorine concentrations in forage. González-Ferrán (1989)[35] measured soluble fluorine concentrations in volcanic ash as high as 3000 ppm, one of the highest contents ever measured in volcanic areas. Nevertheless, Navidad MIs contain about 500 ppm of F on average, similar to the normal ranges among arc volcanoes (Aiuppa et al. (2009)[1]; Webster et al. (2018)[90]). We should mention that the values previously published for F contents in forage, soils and ash during and after the Navidad eruption are either overestimated or not representative. The determination of F content in the magma for the Navidad eruption made in this study is common for volcanic arc centers. We suggest that the consequence of the Navidad eruption, regarding fluorosis and cattle death, might be linked to fluorine composition that are not abnormal in subduction settings, and therefore should represent a risk to be mitigated in volcanic areas such as the LVCAs a suggestion for future studies, olivine-hosted MIs in Navidad tephra and earlier eruptive stages should be analyzed in order to collect more evidence on the low water content of magma for the Navidad eruption. Additionally, we suggest a comparison between Navidad and other units of the LVC by using olivine-hosted MIs compositions for Lonquimay lavas to assess more precisely the volatile budget throughout the eruptive history of the LVC.

BIBLIOGRAPHY

[1] A. Aiuppa, D. Baker, and J. Webster. Halogens in volcanic systems. *Chemical Geology*, 263 (1-4):1–18, 2009.

[2] O. Araya, F. Wittwer, A. Villa, C. Ducom, et al. Bovine fluorosis following volcanic activity in the southern andes. *Veterinary Record*, 126(26):641–642, 1990.

[3] O. Araya, F. Wittwer, and A. Villa. Evolution of fluoride concentrations in cattle and grass following a volcanic eruption. *Veterinary and human toxicology*, 35(5):437–440, 1993.

[4] S. Bellomo, A. Aiuppa, W. D'Alessandro, and F. Parello. Environmental impact of magmatic fluorine emission in the mt. etna area. *Journal of Volcanology and Geothermal Research*, 165(1-2):87–101, 2007.

[5] A. Bénard, K. Koga, N. Shimizu, M. Kendrick, D. Ionov, O. Nebel, and R. J. Arculus. Chlorine and fluorine partition coefficients and abundances in sub-arc mantle xenoliths (kamchatka, russia): implications for melt generation and volatile recycling processes in subduction zones. *Geochimica et Cosmochimica Acta*, 199:324–350, 2017.

[6] D. Bernini, M. Wiedenbeck, D. Dolejš, and H. Keppler. Partitioning of halogens between mantle minerals and aqueous fluids: implications for the fluid flow regime in subduction zones. *Contributions to Mineralogy and Petrology*, 165(1):117–128, 2013.

[7] E. Besoaín, G. Sepúlveda, and A. Sadzawka. La erupción del volcán lonquimay y sus efectos en la agricultura. *Agricultura Técnica (Chile)*, 52:354–358, 1992.

[8] R. J. Bodnar and J. J. Student. *Melt Inclusions in Plutonic Rocks*, chapter Melt Inclusions in Plutonic Rocks: Petrography and Microthermometry, pages 1–26. Mineralogical Association of Canada, 2006.

[9] Y. Bottinga and D. F. Weill. Densities of liquid silicate systems calculated from partial molar volumes of oxide components. *American Journal of Science*, 269(2):169–182, 1970.

[10] R. A. Cabral, M. G. Jackson, K. T. Koga, E. F. Rose-Koga, E. H. Hauri, M. J. Whitehouse, A. A. Price, J. M. Day, N. Shimizu, and K. A. Kelley. Volatile cycling of h2o, co2, f, and cl in the himu mantle: A new window provided by melt inclusions from oceanic hot spot lavas at mangaia, cook islands. *Geochemistry, Geophysics, Geosystems*, 15(11):4445–4467, 2014.

[11] V. Campos. *Memoria de Título: Análisis Comparativo de las ErErupcion del Cono Navidad de 1988-1990 y del Volcán Calbuco de 2015.* 2016.

[12] C. Cannatelli, A. Doherty, R. Esposito, A. Lima, and B. D. Vivo. Understanding a volcano through a droplet: A melt inclusion approach. *Journal of Geochemical Exploration*, 171:4 – 19, 2016. ISSN 0375-6742. doi: https://doi.org/10.1016/j.gexplo.2015.10.003. URL http://

www.sciencedirect.com/science/article/pii/S0375674215300789. Fluid and Melt inclusions.

[13] J. Cembrano and L. Lara. The link between volcanism and tectonics in the southern volcanic zone of the chilean andes: a review. *Tectonophysics*, 471(1-2):96–113, 2009.

[14] S. Collins, D. Pyle, and J. Maclennan. Melt inclusions track pre-eruption storage and dehydration of magmas at etna. *Geology*, 37(6):571–574, 2009.

[15] M. A. Contreras Vargas. DinÁmica de flujos de lava histÓricos de los volcanes lonquimay y villarrica, andes del sur, chile. Master's thesis, University of Chile, 2013.

[16] L. B. Cooper, D. M. Ruscitto, T. Plank, P. J. Wallace, E. M. Syracuse, and C. E. Manning. Global variations in h2o/ce: 1. slab surface temperatures beneath volcanic arcs. *Geochemistry, Geophysics, Geosystems*, 13(3), 2012.

[17] L. Danyushevsky, F. Della-Pasqua, and S. Sokolov. Re-equilibration of melt inclusions trapped by magnesian olivine phenocrysts from subduction-related magmas: petrological implications. *Contributions to Mineralogy and Petrology*, 138(1):68–83, 2000.

[18] L. V. Danyushevsky and P. Plechov. Petrolog3: Integrated software for modeling crystallization processes. *Geochemistry, Geophysics, Geosystems*, 12(7), 2011.

[19] J. H. Davies and D. J. Stevenson. Physical model of source region of subduction zone volcanics. *Journal of Geophysical Research: Solid Earth*, 97(B2):2037–2070, 1992.

[20] D. B. Dingwell, N. Bagdassarov, G. Bussod, and S. L. Webb. Magma rheology. 1993.

[21] J. E. Dixon, E. M. Stolper, and J. R. Holloway. An experimental study of water and carbon dioxide solubilities in mid-ocean ridge basaltic liquids. part i: calibration and solubility models. *Journal of Petrology*, 36(6):1607–1631, 1995.

[22] J. E. Dixon, L. Leist, C. Langmuir, and J.-G. Schilling. Recycled dehydrated lithosphere observed in plume-influenced mid-ocean-ridge basalt. *Nature*, 420(6914):385, 2002.

[23] D. S. Draper and A. D. Johnston. Anhydrous pt phase relations of an aleutian high-mgo basalt: an investigation of the role of olivine-liquid reaction in the generation of arc high-alumina basalts. *Contributions to Mineralogy and Petrology*, 112(4):501–519, 1992.

[24] M. Edmonds and P. J. Wallace. Volatiles and exsolved vapor in volcanic systems. *Elements*, 13(1):29–34, 2017.

[25] R. Esposito, R. Bodnar, L. Danyushevsky, B. De Vivo, L. Fedele, J. Hunter, A. Lima, and N. Shimizu. Volatile evolution of magma associated with the solchiaro eruption in the phlegrean volcanic district (italy). *Journal of Petrology*, 52(12):2431–2460, 2011.

[26] R. Esposito, K. Badescu, M. Steele-MacInnis, C. Cannatelli, B. De Vivo, A. Lima, R. J. Bodnar, and C. E. Manning. Magmatic evolution of the campi flegrei and procida volcanic fields, italy, based on interpretation of data from well-constrained melt inclusions. *Earth-Science Reviews*, 2018.

[27] A. Fall, B. Tattitch, and R. J. Bodnar. Combined microthermometric and raman spectroscopic technique to determine the salinity of h2o–co2–nacl fluid inclusions based on clathrate melting. *Geochimica et Cosmochimica Acta*, 75(4):951–964, 2011.

[28] P. Francis, M. R. Burton, and C. Oppenheimer. Remote measurements of volcanic gas compositions by solar occultation spectroscopy. *Nature*, 396(6711):567, 1998.

[29] G. A. Gaetani, J. A. O'Leary, N. Shimizu, C. E. Bucholz, and M. Newville. Rapid reequilibration of h2o and oxygen fugacity in olivine-hosted melt inclusions. *Geology*, 40(10):915–918, 2012.

[30] D. Gilbert, A. Freundt, S. Kutterolf, and C. Burkert. Post-glacial time series of explosive eruptions and associated changes in the magma plumbing system of lonquimay volcano, south central chile. *International Journal of Earth Sciences*, 103(7):2043–2062, 2014.

[31] D. Giordano, C. Romano, D. Dingwell, B. Poe, and H. Behrens. The combined effects of water and fluorine on the viscosity of silicic magmas. *Geochimica et Cosmochimica Acta*, 68(24):5159–5168, 2004.

[32] D. Giordano, J. K. Russell, and D. B. Dingwell. Viscosity of magmatic liquids: a model. *Earth and Planetary Science Letters*, 271(1-4):123–134, 2008.

[33] R. Goldstein and T. Reynolds. *Systematics of Fluid Inclusions in Diagenetic Minerals*. Society for Sedimentary Geology, 1994.

[34] O. González and M. Vergara. Reconocimiento geológico de la cordillera de los andes entre los paralelos 35 y 38 s: Instituto geológia, universidad de chile. *Santiago*, 24, 1962.

[35] O. González-Ferrán. La erupcion del volcan lonquimay 1988 y su impacto en el medio ambiente, chile. *Revista Geofísica*, 31:39–107, 1989.

[36] M. E. Hartley, D. A. Neave, J. Maclennan, M. Edmonds, and T. Thordarson. Diffusive overhydration of olivine-hosted melt inclusions. *Earth and Planetary Science Letters*, 425:168–178, 2015.

[37] E. Hauri. Sims analysis of volatiles in silicate glasses, 2: isotopes and abundances in hawaiian melt inclusions. *Chemical Geology*, 183(1-4):115–141, 2002.

[38] E. H. Hauri, J. Maclennan, D. McKenzie, K. Gronvold, N. Oskarsson, and N. Shimizu. Co2 content beneath northern iceland and the variability of mantle carbon. *Geology*, 46(1): 55–58, 2018.

[39] W. Hildreth and S. Moorbath. Crustal contributions to arc magmatism in the andes of central chile. *Contributions to mineralogy and petrology*, 98(4):455–489, 1988.

[40] Y. Kawakami, J. Yamamoto, and H. Kagi. Micro-raman densimeter for co 2 inclusions in mantle-derived minerals. *Applied spectroscopy*, 57(11):1333–1339, 2003.

[41] M. Kendrick, C. Hémond, V. Kamenetsky, L. Danyushevsky, C. W. Devey, T. Rodemann, M. Jackson, and M. Perfit. Seawater cycled throughout earth's mantle in partially serpentinized lithosphere. *Nature Geoscience*, 10(3):222, 2017.

[42] M. A. Kendrick, M. Scambelluri, M. Honda, and D. Phillips. High abundances of noble gas and chlorine delivered to the mantle by serpentinite subduction. *Nature Geoscience*, 4(11): 807, 2011.

[43] M. A. Kendrick, M. Scambelluri, J. Hermann, and J. A. Padrón-Navarta. Halogens and noble gases in serpentinites and secondary peridotites: Implications for seawater subduction and the origin of mantle neon. *Geochimica et cosmochimica acta*, 235:285–304, 2018.

[44] A. Koleszar, A. Saal, E. Hauri, A. Nagle, Y. Liang, and M. Kurz. The volatile contents of the galapagos plume; evidence for h2o and f open system behavior in melt inclusions. *Earth and Planetary Science Letters*, 287(3-4):442–452, 2009.

[45] V. Kress and I. S. Carmichael. Stoichiometry of the iron oxidation reaction in silicate melts. *American Mineralogist*, 73(11-12):1267–1274, 1988.

[46] V. C. Kress and I. S. Carmichael. The compressibility of silicate liquids containing fe 2 o 3 and the effect of composition, temperature, oxygen fugacity and pressure on their redox states. *Contributions to Mineralogy and Petrology*, 108(1-2):82–92, 1991.

[47] H. Lamadrid, L. Moore, D. Moncada, J. Rimstidt, R. Burruss, and R. Bodnar. Reassessment of the raman co2 densimeter. *Chemical Geology*, 450:210–222, 2017.

[48] R. A. Lange and I. S. Carmichael. Densities of na2o-k2o-cao-mgo-feo-fe2o3-al2o3-tio2-sio2 liquids: new measurements and derived partial molar properties. *Geochimica et Cosmochimica Acta*, 51(11):2931–2946, 1987.

[49] A. Lavenu and J. Cembrano. Compressional-and transpressional-stress pattern for pliocene and quaternary brittle deformation in fore arc and intra-arc zones (andes of central and southern chile). *Journal of Structural Geology*, 21(12):1669–1691, 1999.

[50] A. S. Lloyd, T. Plank, P. Ruprecht, E. H. Hauri, and W. Rose. Volatile loss from melt inclusions in pyroclasts of differing sizes. *Contributions to Mineralogy and Petrology*, 165(1):129–153, 2013.

[51] S. Matthews, O. Shorttle, J. F. Rudge, and J. Maclennan. Constraining mantle carbon: Co2-trace element systematics in basalts and the roles of magma mixing and degassing. *Earth and Planetary Science Letters*, 480:1–14, 2017.

[52] N. Métrich, P. Allard, N. Spilliaert, D. Andronico, and M. Burton. 2001 flank eruption of the alkali-and volatile-rich primitive basalt responsible for mount etna's evolution in the last three decades. *Earth and Planetary Science Letters*, 228(1-2):1–17, 2004.

[53] N. Mironov, M. Portnyagin, R. Botcharnikov, A. Gurenko, K. Hoernle, and F. Holtz. Quantification of the co2 budget and h2o–co2 systematics in subduction-zone magmas through the experimental hydration of melt inclusions in olivine at high h2o pressure. *Earth and Planetary Science Letters*, 425:1–11, 2015.

[54] L. R. Moore, E. Gazel, R. Tuohy, A. S. Lloyd, R. Esposito, M. Steele-MacInnis, E. H. Hauri, P. J. Wallace, T. Plank, and R. J. Bodnar. Bubbles matter: An assessment of the contribution of vapor bubbles to melt inclusion volatile budgets. *American Mineralogist*, 100(4):806–823, 2015.

[55] H. Moreno and M. C. Gardeweg. La erupción reciente en el complejo volcánico lonquimay (diciembre 1988), andes del sur. *Andean Geology*, 16(1):93–117, 1989.

[56] J. t. Myers and H. Eugster. The system fe-si-o: Oxygen buffer calibrations to 1,500 k. *Contributions to Mineralogy and Petrology*, 82(1):75–90, 1983.

[57] J. Naranjo, R. Sparks, M. Stasiuk, H. Moreno, and G. Ablay. Morphological, structural and textural variations in the 1988–1990 andesite lava of lonquimay volcano, chile. *Geological Magazine*, 129(6):657–678, 1992.

[58] J. A. Naranjo and H. Moreno. Actividad explosiva postglacial en el volcán llaima, andes del sur (38 45's). *Andean Geology*, 18(1):69–80, 1991.

[59] C. R. Neal and L. A. Taylor. A negative ce anomaly in a peridotite xenolith: Evidence for crustal recycling into the mantle or mantle metasomatism? *Geochimica et Cosmochimica Acta*, 53(5):1035–1040, 1989.

[60] S. Newman and J. B. Lowenstern. Volatilecalc: a silicate melt–h2o–co2 solution model written in visual basic for excel. *Computers & Geosciences*, 28(5):597–604, 2002.

[61] S. Y. O'Reilly and W. Griffin. Apatite in the mantle: implications for metasomatic processes and high heat production in phanerozoic mantle. *Lithos*, 53(3-4):217–232, 2000.

[62] G. Palma, F. Barra, M. Reich, V. Valencia, A. C. Simon, J. Vervoort, M. Leisen, and R. Romero. Halogens, trace element concentrations, and sr-nd isotopes in apatite from iron oxide-apatite (ioa) deposits in the chilean iron belt: Evidence for magmatic and hydrothermal stages of mineralization. *Geochimica et Cosmochimica Acta*, 246:515–540, 2019.

[63] P. Pérez-Flores, J. Cembrano, P. Sánchez-Alfaro, E. Veloso, G. Arancibia, and T. Roquer. Tectonics, magmatism and paleo-fluid distribution in a strike-slip setting: Insights from the northern termination of the liquiñe–ofqui fault system, chile. *Tectonophysics*, 680:192–210, 2016.

[64] P. Pérez-Flores, E. Veloso, J. Cembrano, P. Sánchez-Alfaro, M. Lizama, and G. Arancibia. Fracture network, fluid pathways and paleostress at the tolhuaca geothermal field. *Journal of Structural Geology*, 96:134–148, 2017.

[65] P. Pérez-Flores, G. Wang, T. Mitchell, P. Meredith, Y. Nara, V. Sarkar, and J. Cembrano. The effect of offset on fracture permeability of rocks from the southern andes volcanic zone, chile. *Journal of Structural Geology*, 104:142–158, 2017.

[66] T. Plank, K. A. Kelley, M. M. Zimmer, E. H. Hauri, and P. J. Wallace. Why do mafic arc magmas contain 4 wt% water on average? *Earth and Planetary Science Letters*, 364:168–179, 2013.

[67] E. Polanco. *Volcanoestratigrafía, geoquímica y peligro volcánico del volcán Lonquimay (38º30'S), Andes del Sur (Chile)*. PhD thesis, Facultad de Geología, Universidad de Barcelona, 2010.

[68] M. Portnyagin, R. Almeev, S. Matveev, and F. Holtz. Experimental evidence for rapid water exchange between melt inclusions in olivine and host magma. *Earth and Planetary Science Letters*, 272(3-4):541–552, 2008.

[69] K. D. Putirka. Thermometers and barometers for volcanic systems. *Reviews in mineralogy and geochemistry*, 69(1):61–120, 2008.

[70] F. Robbiano. Estudio geoquímico del magma a través de inclusiones vítreas: El caso del cono navidad, ix región de la araucanía, chile. Master's thesis, University of Chile, 2017.

[71] E. Roedder. Origin and significance of magmatic inclusions. *Bull. Mineral*, 1979.

[72] E. Roedder. *Volume 12: Fluid inclusions*. Mineralogical Society of America, 1984.

[73] P. Roeder and R. Emslie. Olivine-liquid equilibrium. *Contributions to mineralogy and petrology*, 29(4):275–289, 1970.

[74] H. R. Rollinson. *Using geochemical data: evaluation, presentation, interpretation*. Routledge, 2014.

[75] A. E. Saal, E. H. Hauri, C. H. Langmuir, and M. R. Perfit. Vapour undersaturation in primitive mid-ocean-ridge basalt and the volatile content of earth's upper mantle. *Nature*, 419(6906): 451, 2002.

[76] L. Salem, M. Edmonds, R. Corsaro, and J. Maclennan. Carbon dioxide in geochemically heterogeneous melt inclusions from mount etna, italy. *Geochemistry, Geophysics, Geosystems*, 2019.

[77] P. Sanchez-Alfaro, M. Reich, G. Arancibia, P. Pérez-Flores, J. Cembrano, T. Driesner, M. Lizama, J. Rowland, D. Morata, C. A. Heinrich, et al. Physical, chemical and mineralogical evolution of the tolhuaca geothermal system, southern andes, chile: insights into the interplay between hydrothermal alteration and brittle deformation. *Journal of Volcanology and Geothermal Research*, 324:88–104, 2016.

[78] T. Sisson and S. Bronto. Evidence for pressure-release melting beneath magmatic arcs from basalt at galunggung, indonesia. *Nature*, 391(6670):883, 1998.

[79] H. C. Sorby. On the microscopical, structure of crystals, indicating the origin of minerals and rocks. *Quarterly Journal of the Geological Society*, 14(1-2):453–500, 1858. ISSN 0370-291X. doi: 10.1144/GSL.JGS.1858.014.01-02.44. URL http://jgs.lyellcollection.org/content/14/1-2/453.

[80] N. Spilliaert, P. Allard, N. Métrich, and A. Sobolev. Melt inclusion record of the conditions of ascent, degassing, and extrusion of volatile-rich alkali basalt during the powerful 2002 flank eruption of mount etna (italy). *Journal of Geophysical Research: Solid Earth*, 111(B4), 2006.

[81] M. Steele-Macinnis, R. Esposito, and R. J. Bodnar. Thermodynamic model for the effect of post-entrapment crystallization on the h2o?co2 systematics of vapor-saturated, silicate melt inclusions. *Journal of Petrology*, 52(12):2461–2482, 2011. doi: 10.1093/petrology/egr052. URL http://dx.doi.org/10.1093/petrology/egr052.

[82] M. Suarez and C. Emparan. *Hoja Curacautin. Region de la Araucania y del Bio Bio. Escala 1:250.000.* Servicio Nacional de Geologia y Mineria, Chile, 1997.

[83] R. Thiele, A. Lahsen, H. Moreno, J. Varela, M. Vergara, and F. Munizaga. Estudio geológico regional a escala 1: 100.000 de la hoya superior y curso médio del rio biobío. *ENDESA-Departamento de Geología y Geofísica, Universidad de Chile. Informe Inédito*, 1987.

[84] M. Toplis. The thermodynamics of iron and magnesium partitioning between olivine and liquid: criteria for assessing and predicting equilibrium in natural and experimental systems. *Contributions to Mineralogy and Petrology*, 149(1):22–39, 2005.

[85] D. Trail, E. B. Watson, and N. D. Tailby. Ce and eu anomalies in zircon as proxies for the oxidation state of magmas. *Geochimica et Cosmochimica Acta*, 97:70–87, 2012.

[86] C. A. Vergara Saéz. PetrogÉnesis de los centros eruptivos del complejo volcÁnico lonquimay (cvl), ix regiÓn de la araucanÍa. Master's thesis, University of Chile, 2010.

[87] P. J. Wallace. Volatiles in subduction zone magmas: concentrations and fluxes based on melt inclusion and volcanic gas data. *Journal of volcanology and Geothermal Research*, 140 (1-3):217–240, 2005.

[88] P. J. Wallace, V. S. Kamenetsky, and P. Cervantes. Melt inclusion co2 contents, pressures of olivine crystallization, and the problem of shrinkage bubbles. *American Mineralogist*, 100 (4):787–794, 2015.

[89] J. D. Webster and P. M. Piccoli. Magmatic apatite: A powerful, yet deceptive, mineral. *Elements*, 11(3):177–182, 2015.

[90] J. D. Webster, D. R. Baker, and A. Aiuppa. Halogens in mafic and intermediate-silica content magmas. In *The Role of Halogens in Terrestrial and Extraterrestrial Geochemical Processes*, pages 307–430. Springer, 2018.

[91] C. S. Witham, C. Oppenheimer, and C. J. Horwell. Volcanic ash-leachates: a review and recommendations for sampling methods. *Journal of volcanology and Geothermal Research*, 141(3-4):299–326, 2005.

A

APPENDIX A: MICROPROBE PICTURES

A

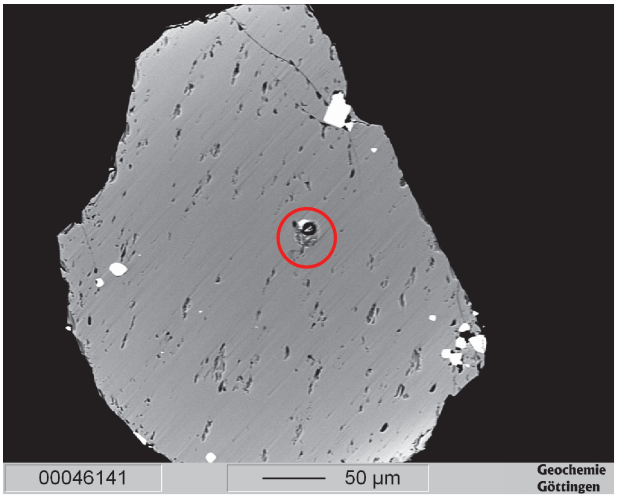

NV18.O.AI_MI_01

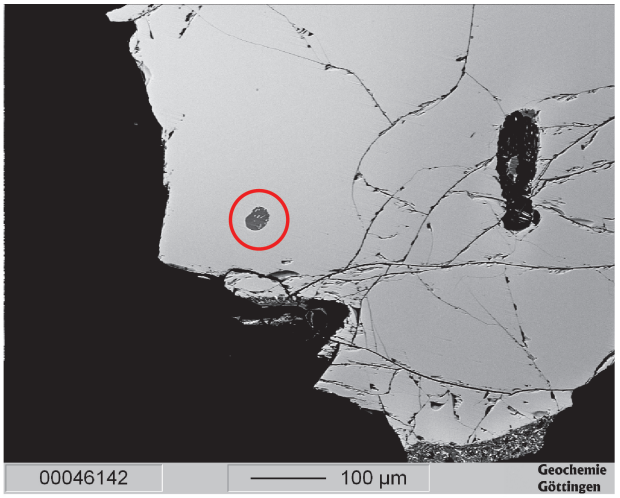

NV19.O.07_MI_01

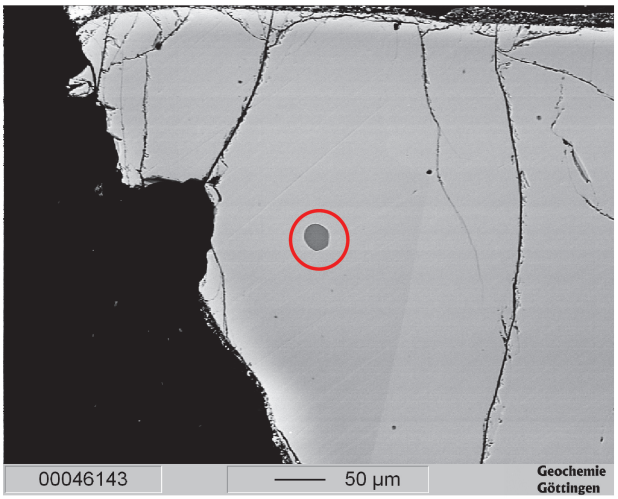

NV19.O.03_MI_01

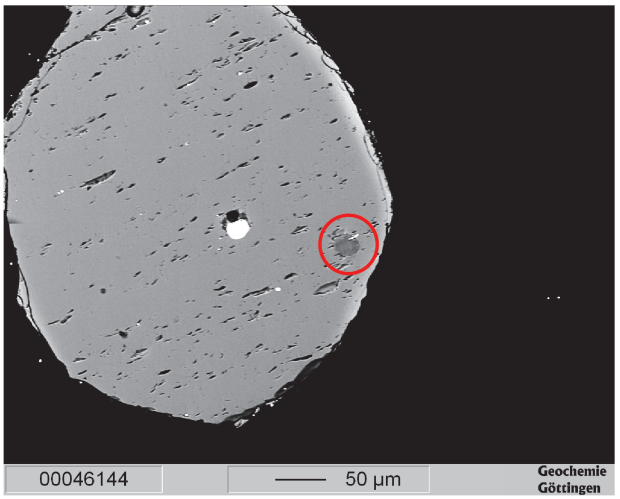

NV19.O.27_MI_01

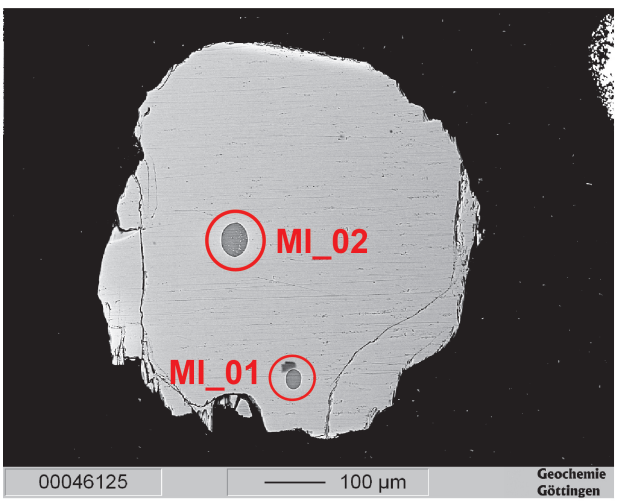

NV19.O.25_MI_01 and MI_02

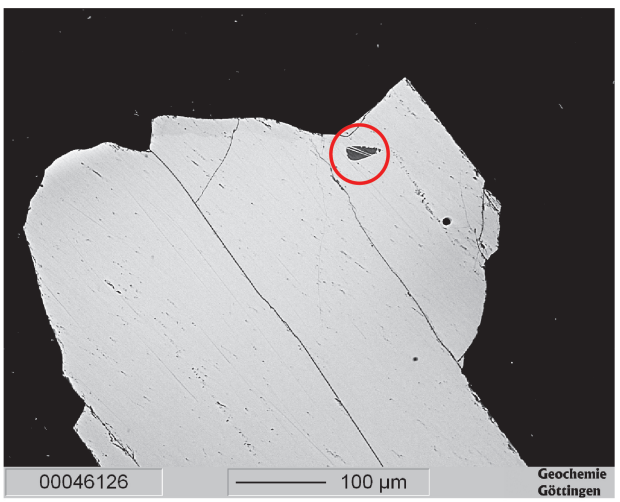

NV19.O.20_MI_01

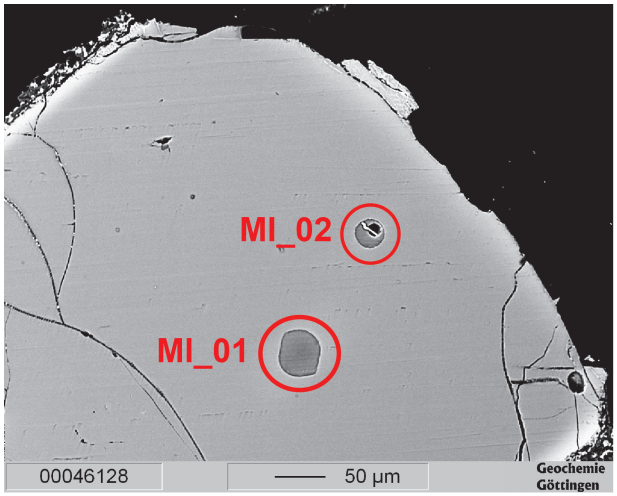

NV19.O.19_MI_01 and MI_02

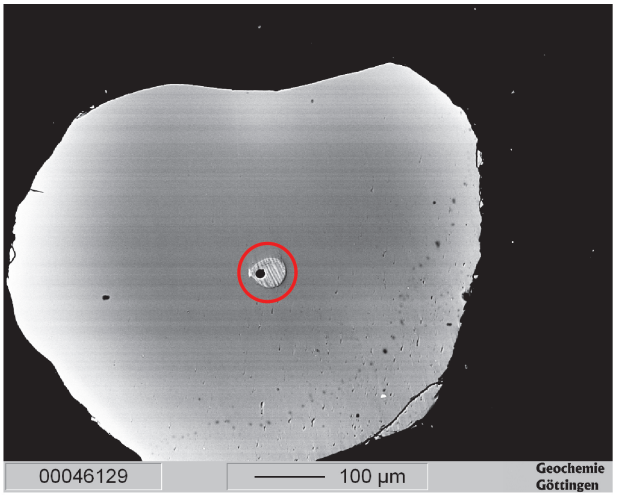

NV18.O.12-13_MI_01

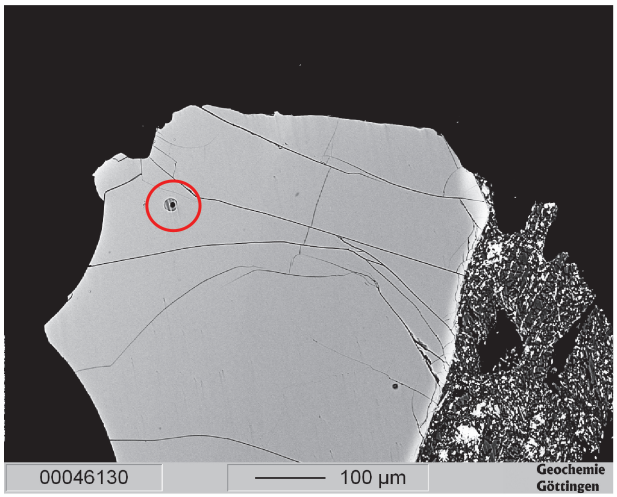

NV18.O.AK_MI_01

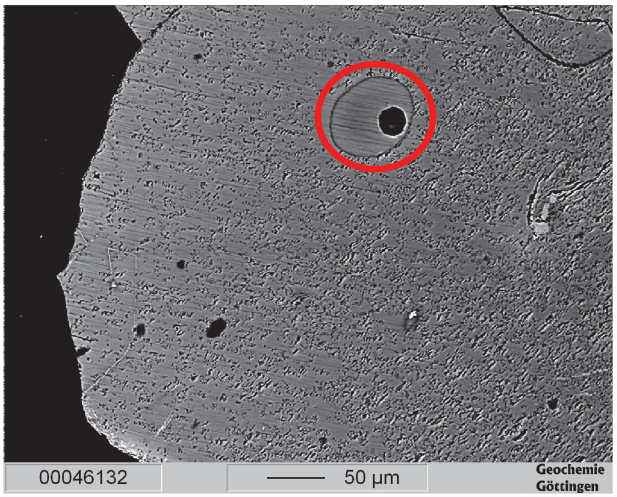

NV19.O.13_MI_01

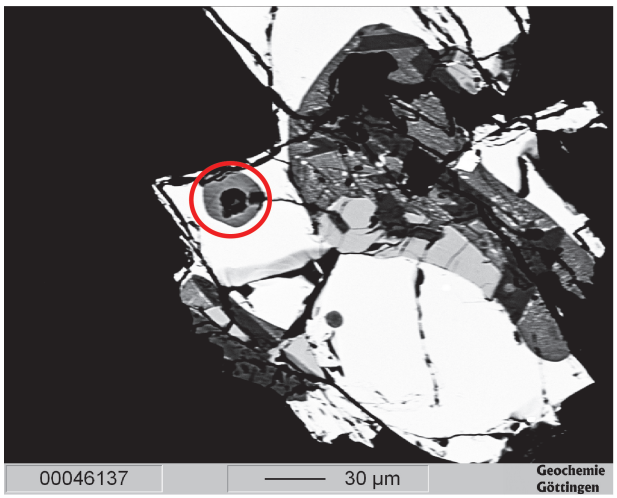

H4.PL.AH_MI_01

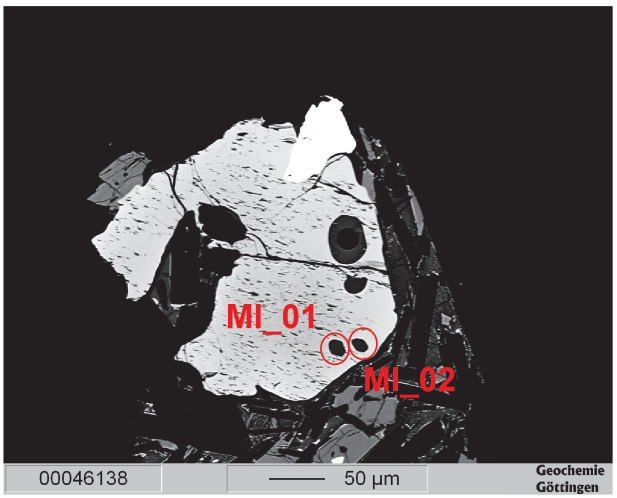

H4.O.21_14_MI_01 and MI_02

A

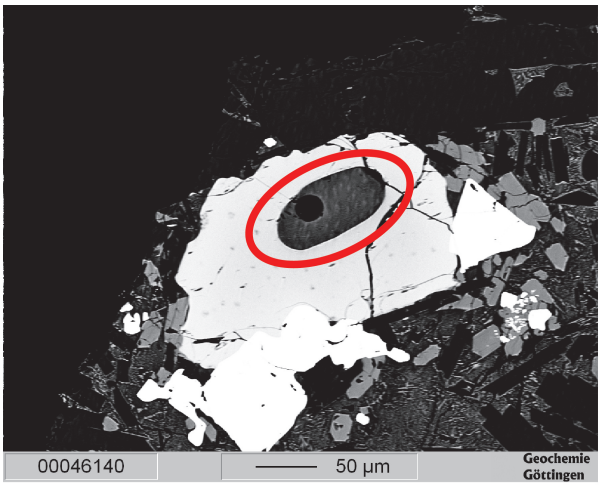

H4.O.27_MI_01

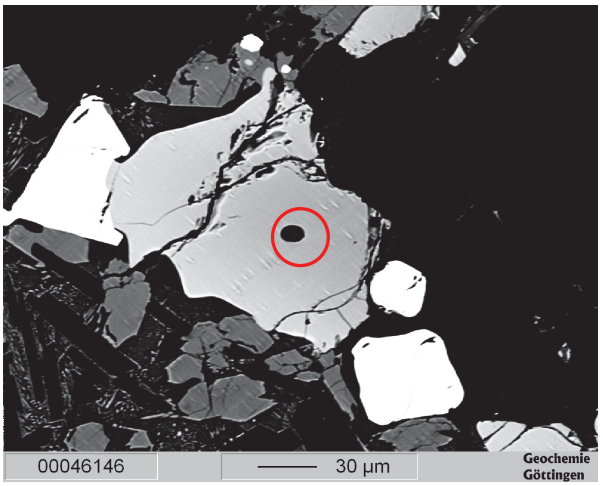

H4.PL.85_MI_01

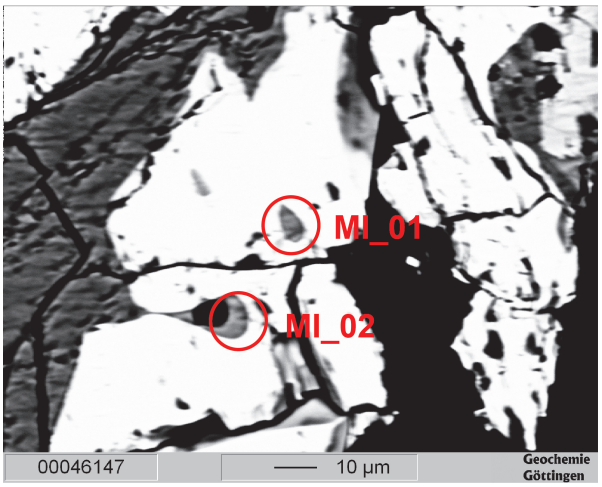

H4.PL.55_MI_01 and MI_02

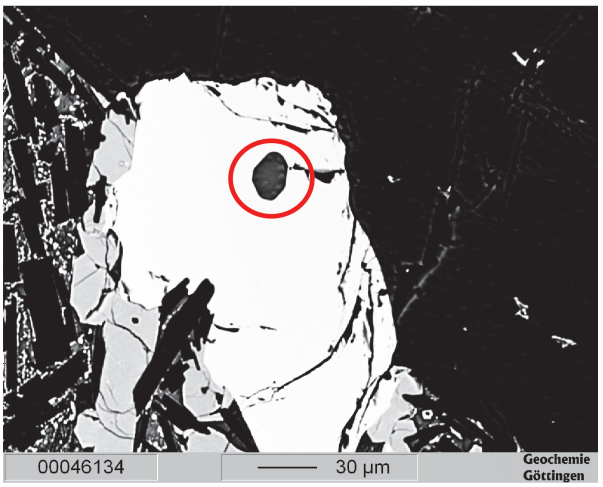

H4.PL.AN_MI_01

H4.O.24_MI_01

H4.O.16_MI_01

B

APPENDIX B: DATA TABLES

SAMPLE	Na2O [%]	MgO [%]	Al2O3 [%]	TiO2 [%]	CaO [%]	Cl [%]	SiO2 [%]	MnO [%]	FeO [%]	Total [%]	Fo [%]
NV18_22_Ol_01	-	36.79	0.04	0.05	0.19	-	37.78	0.34	21.97	97.17	74.91
NV18_Compoline_ol_cpx	-	36.16	-	-	0.2	-	37.79	0.34	21.62	96.12	74.89
NV18_14_ol_zona	-	36.06	-	-	0.21	-	37.8	0.42	25.49	99.98	71.61
NV18_14_79_ol	-	34.64	-	0.05	0.34	-	37.72	0.4	26.56	99.71	69.93
NV18_Right_oliv_03	-	35.75	-	-	0.2	-	37.65	0.41	25.15	99.16	71.71
NV19_01_ol	-	39.95	-	-	0.41	-	39.54	0.35	19.99	100.24	78.08
NV24_01_ol	-	34.99	-	-	0.18	-	37.73	0.48	26.61	99.99	70.10
NV24_22_oli_desint	-	35.77	-	-	0.19	-	37.72	0.46	26.15	100.29	70.92
NV24_ol_core	-	34.96	-	-	0.19	-	37.51	0.48	26.65	99.79	70.05
NV24_Ol_tiny_01	-	35.83	0.04	-	0.18	-	37.72	0.48	26	100.25	71.07
NV24_Ol_tiny_02	-	35.44	0.03	-	0.19	-	37.57	0.43	26.82	100.47	70.20
NV24_Ol_tiny_03	-	34.17	-	-	0.23	-	37.24	0.49	27.98	100.11	68.53
NV24_Ol_tiny_04	0.04	35.28	-	-	0.18	-	37.8	0.5	26.37	100.17	70.46
Host Olivines											
NV19_O_25_host	-	42.28	-	-	0.19	-	38.96	0.3	18.22	99.95	80.53
NV19_O_20_host	-	38.47	-	-	0.17	-	37.76	0.36	21.96	98.72	75.75
NV19_O_19_host	-	41.48	-	-	0.19	-	38.3	0.29	18	98.25	80.42
NV18_O_12-13_host	-	47.98	-	-	0.14	-	40.77	0.17	11.58	100.63	88.08
NV19_O_18_host	-	41.86	-	-	0.19	-	38.74	0.29	18.15	99.22	80.44
NV18_O_AK_host	-	40.11	-	-	0.18	-	38.18	0.33	20.53	99.33	77.69
NV19_O_13_host	-	41.94	-	-	0.2	-	38.06	0.25	16.3	96.75	82.10
H4_O_AN_host	-	26	-	-	0.23	-	34.92	0.75	37.09	98.99	55.55
H4_O_24_host	-	23.69	-	0.05	0.33	-	35.29	0.83	39.58	99.77	51.62
H4_O_16_host	-	25.48	-	-	0.23	-	35.34	0.79	38.13	99.96	54.37
H4_O_AZ_01_host	-	29.1	-	-	0.2	-	35.42	0.59	29.62	94.93	63.66
H4_PL_AH_ol_host	-	27.3	0.03	0.05	0.22	0.01	35.01	0.62	33.95	97.2	58.91
H4_O_21-14_host	-	25.85	0.03	0.04	0.24	-	35.6	0.76	37.88	100.38	54.89
H4_O_23_host	-	24.84	0.4	-	0.22	0.02	33.8	0.83	37.52	97.63	54.14
H4_O_27_host	0.05	24.3	-	0.05	0.22	-	34.7	0.83	39.34	99.49	52.41
Nv18_O_AI_host	-	42.05	0.04	-	0.16	-	38.33	0.25	17.25	98.07	81.29
NV19_O_03_host	-	39.21	0.03	-	0.19	-	38.24	0.34	21.97	99.97	76.09
Nv19_O_27_host	-	39.84	-	-	0.18	-	37.77	0.33	19.66	97.77	78.32
NV19_O_07_host	-	40.44	-	-	0.19	-	38.92	0.35	20.86	100.76	77.56
NV18_O_AQ_host	-	40.64	-	-	0.17	-	38.92	0.33	20.59	100.64	77.87
H4_PL_85_ol_host	-	25.98	-	0.05	0.21	-	35.19	0.79	37.74	99.96	55.10
H4_PL_55_ol_host	-	25.82	-	-	0.26	-	35.32	0.81	38.11	100.32	54.71

Table B.1: Electron Microprobe analysis of olivines from Lonquimay and Navidad samples.

80

SAMPLE	Na2O [%]	MgO [%]	Al2O3 [%]	K2O [%]	TiO2 [%]	CaO [%]	SiO2 [%]	FeO [%]	Total [%]
H4_PL_11_01	5.13	0.07	29.34	0.16	-	11.12	53.33	0.71	99.86
H4_PL_11_02	4.4	0.08	30.91	0.11	-	12.26	51.43	0.65	99.84
H4_PL_11_03	4.47	0.08	30.07	0.07	-	12	52.63	0.6	99.92
H4_PL_20_01	5.3	0.08	30.14	0.12	-	10.08	53.54	0.6	99.86
H4_PL_20_02	5.72	0.09	29.03	0.18	-	9.49	54.66	0.68	99.85
H4_PL2_20_01	5.28	0.11	30.19	0.11	-	10.58	53.1	0.53	99.9
H4_PL_04_01	5.15	0.08	30.77	0.09	-	10.38	52.98	0.49	99.94
H4_PL_04_02	5.09	0.07	31.55	0.09	-	9.84	52.71	0.51	99.86
H4_PL_04_03	4.44	0.09	32.25	0.09	-	10.96	51.52	0.58	99.93
H4_PL2_04_01	5.52	0.1	29.6	0.1	-	10.02	54.02	0.58	99.94
H4_PL_15_01	4.63	0.11	30.17	0.11	-	10.35	53.97	0.44	99.78
H4_PL_15_02	5.62	0.11	29.39	0.09	-	8.9	55.44	0.38	99.93
H4_PL_AH_PL01	6.28	0.09	26.61	0.28	-	8.79	56.57	1.14	99.76
H4_PL_85_PL01	6.17	0.11	26.5	0.26	-	9.15	56.7	0.95	99.84
H4_PL_55_PL01	4.48	0.09	31.04	0.12	-	12.01	51.51	0.68	99.93
NV18_plg_14	3	0.11	31.28	0.12	-	14.85	48.72	0.73	98.81
NV18_plg_14_Big	2.1	0.1	32.88	0.06	-	16.39	47.04	0.61	99.18
NV18_plg_MicroCx_01	4.97	0.1	28.23	0.29	-	11.24	53.86	0.94	99.63
NV18_plg_MicroCx_02	4.81	0.1	28.32	0.26	-	11.44	53.21	0.96	99.1
NV18_plg_MicroCx_03	4.99	0.12	28.07	0.28	0.1	11.34	53.75	0.98	99.63
NV18_plg_MicroCx_04	4.89	0.09	28.23	0.29	-	11.37	53.6	1.09	99.56
NV18_plg_MicroCx_05	4.83	0.09	28.02	0.29	0.05	11.46	53.46	1.06	99.26
NV18_plg_MicroCx_06	5.32	0.11	27.56	0.35	0.04	10.91	54.38	0.96	99.63
NV18_plg_14_Zon	3.85	0.1	30.09	0.15	-	13.44	50.84	0.71	99.18
Nv18_14_02_Plg_sieve	2.45	1.12	30.58	0.12	-	15.28	48.05	1.85	99.45
NV18_13_01_plg	1.85	0.12	33.49	0.05	0.07	16.96	46.63	0.73	99.9
NV18_13_02_plg	1.91	0.11	33.46	0.05	0.11	16.9	46.39	0.64	99.57
NV18_AA_zon	3.89	0.11	29.96	0.15	-	13.26	50.95	0.69	99.01
NV18_plg_microCx_plgKg_01	4.68	0.1	28.88	0.26	0.1	12.09	52.35	1	99.46
NV18_plg_microCx_plgKg_02	4.53	0.14	29.05	0.24	0.07	12.23	52.2	0.89	99.35
NV18_plg_microCx_plgKg_04	4.6	0.16	28.68	0.26	-	11.94	52.62	0.97	99.23
NV18_plg_microCx_plgKg_05	5.11	0.1	28.4	0.27	0.07	11.17	53.7	1	99.82
NV24_AA_plg	4.79	0.11	28.73	0.3	-	11.74	52.92	0.67	99.26
NV24_AB_plg	4.76	0.11	28.7	0.29	-	11.83	52.86	0.68	99.23
NV24_ol_plg_ZZ	4.75	0.13	28.62	0.3	-	11.81	53.03	0.78	99.42
NV19_02_plg	4.45	0.11	29.27	0.15	0.07	12.25	52.39	0.71	99.4

Table B.2: Electron Microprobe analysis of plagioclases from Lonquimay and Navidad samples.

81

SAMPLE	Na2O [%]	MgO [%]	Al2O3 [%]	K2O [%]	TiO2 [%]	CaO [%]	SiO2 [%]	MnO [%]	FeO [%]	Total [%]
NV19_Micro_Cpx_01	0.05	24.96	0.11	-	0.05	0.35	35.47	0.65	37.49	99.13
NV19_Micro_Cpx_02	0.52	16.25	3.65	0.16	0.77	7.15	49.26	0.55	21.77	100.08
NV19_AgloCpx_01	0.29	15.43	2.88	-	0.64	21.1	51.29	0.2	7.68	99.51
NV19_CPX_Microlite_02	3.64	8.41	11.08	0.3	0.53	12.53	53.96	0.31	8.46	99.22
NV19_CPX_Microlite_03	0.39	13.9	3.27	0.1	1.15	16.46	50.01	0.42	13.12	98.82
NV19_CPX_Microlite_04	0.29	16.79	2.52	0.04	0.9	10.78	50.78	0.55	16.77	99.42
NV24_Ol_core_px	0.04	25.29	0.9	-	0.42	1.91	53.42	0.48	16.81	99.27
NV18_Compoline_ol_px	0.11	20.7	1.22	-	0.54	6.03	52.11	0.47	17.61	98.79
NV18ZonedCpx	0.26	16.19	2.37	-	0.63	18.03	51.39	0.28	9.97	99.12
NV18_14_80_px	0.3	16.24	2.07	-	0.54	19.28	52.16	0.27	8.8	99.66
NV18_03_zoned	0.34	14.65	3.03	-	0.84	19.37	50.73	0.29	10.17	99.42
NV18_CPx_Carrot_Left	0.4	15.02	2.67	-	0.56	18.98	51.89	0.29	9.33	99.14
NV18_CPx_Carrot_Right	0.3	15.07	2.35	-	0.69	19.4	51.26	0.3	9.86	99.23
NV18_MicroCpx01	0.07	21.91	0.59	-	0.32	3.48	52.64	0.55	19.49	99.05
NV18_MicroCpx02	0.11	20.36	0.79	-	0.35	3.97	53.07	0.56	20.36	99.57
NV18_MicroCpx03	2.05	0.99	11.54	3.81	1.69	4.13	64.71	0.14	8.3	97.36
NV18_MicroCpx04	0.15	20.43	1.03	0.07	0.48	4.69	53.23	0.51	19.57	100.16
NV18_MicroCpx05	0.3	15.13	3.57	-	1.05	17.97	49.65	0.28	10.98	98.93
NV18_MicroCpx06	3.83	8.04	10.92	0.77	0.5	5.08	53.56	0.32	12.02	95.04
NV18_MicroCpx07	1.71	6.26	8.49	2.61	1.41	5.41	57.16	0.29	11.49	94.83
NV18_MicroCpx08	2.41	0.27	13.41	4.69	1.42	1.48	67.31	0.06	3.4	94.45
NV18_MicroCpx09	0.23	16.45	2.88	-	0.94	16.39	50.9	0.29	11.17	99.25
NV18_MicroCpx10	0.28	15.4	1.48	0.03	0.67	15.37	51.92	0.41	13.74	99.3
H4_Pl_AH_Cpx01	0.06	21.07	0.47	-	0.42	2.27	51.49	0.71	20.82	97.31
H4_Pl_85_Cpx_01	0.07	17.89	0.71	0.03	0.65	4.47	51.44	0.81	23.58	99.65
H4_Pl_85_Cpx_02	0.07	18.28	0.71	-	0.44	3.6	51.54	0.86	23.43	98.93

Table B.3: Electron Microprobe analysis of clinopyroxenes from Lonquimay and Navidad samples.

82

SAMPLE	Na2O [%]	MgO [%]	Al2O3 [%]	K2O [%]	TiO2 [%]	CaO [%]	Cl [%]	SiO2 [%]	MnO [%]	FeOt [%]	BaO [%]	Total [%]
NV19_O_55_MI01	4.03	4.75	21.38	1.20	1.27	8.33	0.07	54.06	0.08	5.25	-	100.42
NV18_O_AI_MI_01	4.69	1.17	21.87	0.66	1.19	11.50	0.14	50.91	0.07	4.10	-	96.30
NV19_O_07	5.56	0.50	21.09	1.80	1.73	6.32	0.14	59.15	0.07	2.61	0.07	98.94
NV19_O_03_MI01	4.54	1.11	19.76	1.15	1.35	10.41	0.11	54.73	0.10	3.43	-	96.69
NV19_O_27_MI01	4.45	1.14	22.27	0.75	1.27	12.07	0.10	53.58	0.11	3.53	-	99.26
NV18_O_AQ_MI01	4.15	1.10	28.73	0.94	1.19	9.94	0.13	48.72	0.09	3.46	-	98.45
NV19_O_25_MI_01	4.61	1.18	21.62	0.83	1.24	11.60	0.10	53.78	0.08	3.68	-	98.72
NV19_O_25_MI_02	4.94	1.21	21.00	1.05	1.27	10.94	0.11	53.83	0.08	3.92	-	98.35
NV19_O_20_MI_01	5.04	2.27	19.14	1.29	1.47	6.14	0.13	57.92	0.07	4.26	-	97.73
NV19_O_MI_01	4.94	2.10	20.80	0.97	1.25	9.43	0.09	52.92	0.09	4.36	-	96.95
NV19_O_19_MI_02	4.87	2.71	19.94	0.88	1.31	9.01	0.10	52.78	0.12	5.12	-	96.83
NV18_O_12-13_MI_01	4.68	2.20	23.33	0.60	0.99	11.24	0.10	51.03	0.07	3.52	-	97.75
NV19_O_18_MI_01	3.15	1.26	32.96	0.56	0.90	9.08	0.08	42.93	0.08	4.98	-	95.99
NV18_O_AK_MI_01	4.68	1.49	19.79	0.93	1.65	9.20	0.09	54.67	0.10	5.02	-	97.62
NV19_O_13_MI_01	3.46	5.64	18.70	0.66	0.93	10.03	0.07	49.53	0.11	6.08	-	95.20
H4_PL_AH_MI01	3.85	1.14	22.85	0.93	1.55	7.18	0.15	50.86	0.18	7.15	0.06	95.85
H4_O_21_14_MI_01	5.37	0.93	19.21	1.05	1.77	7.46	0.15	57.64	0.16	7.44	-	101.18
H4_O_21_14_MI_02	5.42	0.70	17.57	1.18	1.81	7.25	0.17	58.00	0.19	7.38	0.18	99.66
H4_O_23_MI_01	4.13	0.80	28.86	1.04	1.45	6.10	0.16	46.79	0.18	6.01	-	95.53
H4_O_27_MI_01	4.43	1.55	16.60	1.12	1.64	6.53	0.15	52.83	0.25	11.76	-	96.84
H4_PL_85_MI01	5.40	0.87	21.64	1.31	1.85	5.96	0.16	56.37	0.10	5.45	0.08	99.12
H4_PL_55_MI01	4.49	1.17	16.16	2.09	2.11	4.68	0.18	61.53	0.15	6.28	0.11	98.84
H4_PL_55_MI02	2.88	1.35	16.78	2.35	2.14	4.58	0.18	59.29	0.13	5.92	0.06	95.60
H4_O_AN_MI_01	4.91	1.07	17.99	1.07	1.74	7.09	0.16	55.37	0.15	7.23	-	96.78
H4_O_24_MI_01	3.74	2.89	16.28	1.14	1.80	5.97	0.16	57.86	0.22	10.04	-	100.10
H4_O_24_MI_02	7.45	0.63	15.52	1.46	1.70	2.56	0.18	64.02	0.16	6.85	-	100.53
H4_O_16_MI_01	5.40	0.80	18.02	1.15	1.78	7.05	0.16	57.38	0.19	7.34	-	99.27
H4_PL_AZ_MI_01	4.15	5.65	18.06	0.87	1.25	4.46	0.13	50.40	0.20	9.03	-	94.21

Table B.4: Electron Microprobe analysis of melt inclusions from Lonquimay and Navidad samples without correction.

83

SAMPLE	Na2O [%]	MgO [%]	Al2O3 [%]	K2O [%]	TiO2 [%]	CaO [%]	SiO2 [%]	MnO [%]	Fe2O3 [%]	FeO [%]	BaO [%]	Fo [%]	FeO_final [%]	H2O [%]	P2O5 [%]
NV19_O_55_MI01	4.03	4.75	21.38	1.2	1.27	8.33	54.06	0.08	2.24	3.01	-	80.9	9.7	-	0.23
NV18_O_AI_MI_01	4.69	1.17	21.87	0.66	1.19	11.5	50.91	0.07	1.75	2.35	-	80.9	8.4	-	0.23
NV19_O_07	5.56	0.5	21.09	1.8	1.73	6.32	59.15	0.07	1.11	1.49	0.07	77.1	9.7	0.14	0.23
NV19_O_03_MI01	4.54	1.11	19.76	1.15	1.35	10.41	54.73	0.1	1.46	1.97	-	75.6	9.7	0.12	0.23
NV19_O_27_MI01	4.45	1.14	22.27	0.75	1.27	12.07	53.58	0.11	1.5	2.03	-	77.8	9.7	-	0.23
NV18_O_AQ_MI01	4.15	1.1	28.73	0.94	1.19	9.94	48.72	0.09	1.48	1.99	-	77.4	8.4	-	0.23
NV19_O_25_MI_01	4.61	1.18	21.62	0.83	1.24	11.6	53.78	0.08	1.57	2.11	-	80.1	9.7	0.11	0.23
NV19_O_25_MI_02	4.94	1.21	21	1.05	1.27	10.94	53.83	0.08	1.67	2.25	-	80.1	9.7	0.1	0.23
NV19_O_20_MI_01	5.04	2.27	19.14	1.29	1.47	6.14	57.92	0.07	1.82	2.44	-	75.3	9.7	-	0.23
NV19_O_MI_01	4.94	2.1	20.8	0.97	1.25	9.43	52.92	0.09	1.86	2.5	-	80	9.7	-	0.23
NV19_O_19_MI_02	4.87	2.71	19.94	0.88	1.31	9.01	52.78	0.12	2.18	2.94	-	80	9.7	0.13	0.23
NV18_O_12-13_MI_01	4.68	2.2	23.33	0.6	0.99	11.24	51.03	0.07	1.5	2.02	-	87.8	8.4	-	0.23
NV19_O_18_MI_01	3.15	1.26	32.96	0.56	0.9	9.08	42.93	0.08	2.12	2.86	-	80	9.7	0.19	0.23
NV18_O_AK_MI_01	4.68	1.49	19.79	0.93	1.65	9.2	54.67	0.1	2.14	2.88	-	77.2	8.4	0.23	0.23
NV19_O_13_MI_01	3.46	5.64	18.7	0.66	0.93	10.03	49.53	0.11	2.59	3.49	-	81.7	9.7	0.11	0.23
H4_PL_AH_MI01	3.85	1.14	22.85	0.93	1.55	7.18	50.86	0.18	3.12	4.03	0.06	58.3	10.9	-	0.33
H4_O_21_14_MI_01	5.37	0.93	19.21	1.05	1.77	7.46	57.64	0.16	3.25	4.19	-	54.2	10.9	0.15	0.33
H4_O_21_14_MI_02	5.42	0.7	17.57	1.18	1.81	7.25	58	0.19	3.22	4.16	0.18	54.2	10.9	-	0.33
H4_O_23_MI_01	4.13	0.8	28.86	1.04	1.45	6.1	46.79	0.18	2.62	3.39	-	53.4	10.9	-	0.33
H4_O_27_MI_01	4.43	1.55	16.6	1.12	1.64	6.53	52.83	0.25	5.13	6.63	-	51.7	10.9	0.14	0.33
H4_PL_85_MI01	5.4	0.87	21.64	1.31	1.85	5.96	56.37	0.1	2.38	3.07	0.08	54.4	10.9	-	0.33
H4_PL_55_MI01	4.49	1.17	16.16	2.09	2.11	4.68	61.53	0.15	2.74	3.54	0.11	54	10.9	-	0.33
H4_PL_55_MI02	2.88	1.35	16.78	2.35	2.14	4.58	59.29	0.13	2.58	3.34	0.06	54	10.9	-	0.33
H4_PL_AN_MI_01	4.91	1.07	17.99	1.07	1.74	7.09	55.37	0.15	3.15	4.07	-	54.9	10.9	0.01	0.33
H4_O_24_MI_01	3.74	2.89	16.28	1.14	1.8	5.97	57.86	0.22	4.38	5.66	-	50.8	10.9	-	0.33
H4_O_24_MI_02	7.45	0.63	15.52	1.46	1.7	2.56	64.02	0.16	2.99	3.86	-	50.8	10.9	-	0.33
H4_O_16_MI_01	5.4	0.8	18.02	1.15	1.78	7.05	57.38	0.19	3.2	4.14	-	53.7	10.9	0.14	0.33
H4_PL_AZ_MI_01	4.15	5.65	18.06	0.87	1.25	4.46	50.4	0.2	3.94	5.09	-	63	10.9	-	0.33

Table B.5: Initial parameters set in Petrolog to correct MIs for PEC and other effects.

SAMP_NO	Fo Host [%]	SiO2 [%]	TiO2 [%]	Al2O3 [%]	Fe2O3 [%]	FeO [%]	MnO [%]	MgO [%]	CaO [%]	Na2O [%]	K2O [%]	P2O5 [%]
NV19_O_55_MI01	80.90	53.67	1.26	21.13	0.24	5.24	0.08	4.76	8.23	3.98	1.19	0.23
NV18_O_AI_MI_01	80.90	53.63	1.27	23.37	0.07	1.85	0.06	1.49	12.29	5.01	0.71	0.25
NV19_O_07	77.10	60.13	1.77	21.58	0.06	1.43	0.06	0.60	6.46	5.69	1.84	0.24
NV19_O_03_MI01	75.60	56.72	1.40	20.54	0.12	2.81	0.11	1.20	10.82	4.72	1.20	0.24
NV19_O_27_MI01	77.80	54.44	1.30	22.82	0.08	1.99	0.11	1.33	12.37	4.56	0.77	0.24
NV19_O_25_MI_01	80.10	54.78	1.27	22.17	0.09	2.45	0.08	1.32	11.89	4.73	0.85	0.24
NV19_O_25_MI_02	80.10	55.12	1.31	21.67	0.11	2.53	0.08	1.36	11.29	5.10	1.09	0.24
NV19_O_20_MI_01	75.30	58.84	1.48	19.28	0.28	4.88	0.08	2.36	6.18	5.08	1.30	0.23
NV19_O_MI_01	80.00	54.77	1.29	21.60	0.19	3.70	0.09	2.20	9.79	5.13	1.00	0.24
NV19_O_19_MI_02	80.00	54.97	1.38	20.99	0.17	3.62	0.12	2.83	9.48	5.13	0.93	0.25
NV18_O_12-13_MI_01	87.80	52.75	1.04	24.42	0.06	1.76	0.07	2.37	11.76	4.90	0.62	0.24
NV18_O_AK_MI_01	77.20	56.44	1.72	20.63	0.17	3.38	0.10	1.64	9.59	4.88	0.97	0.24
NV19_O_13_MI_01	81.70	51.61	0.96	19.27	0.28	6.91	0.12	5.93	10.34	3.56	0.68	0.24
H4_PL_AH_MI01	58.30	53.60	1.65	24.33	0.31	5.53	0.18	1.31	7.64	4.10	1.00	0.35
H4_O_21_14_MI_01	54.20	57.47	1.78	19.33	0.38	5.42	0.15	1.03	7.50	5.40	1.06	0.33
H4_O_21_14_MI_02	54.20	59.15	1.87	18.17	0.35	4.73	0.17	0.90	7.49	5.60	1.22	0.34
H4_O_27_MI_01	51.70	55.37	1.74	17.66	0.78	9.15	0.25	1.72	6.94	4.71	1.19	0.35
H4_PL_85_MI01	54.40	57.03	1.88	21.95	0.31	4.64	0.10	0.90	6.05	5.48	1.33	0.34
H4_PL_55_MI01	54.00	62.11	2.12	16.27	0.49	6.01	0.15	1.18	4.71	4.52	2.10	0.33
H4_PL_55_MI02	54.00	61.48	2.20	17.25	0.49	6.62	0.14	1.40	4.71	2.96	2.42	0.34
H4_PL_AN_MI_01	54.90	57.65	1.82	18.86	0.43	5.86	0.15	1.18	7.43	5.15	1.12	0.35
H4_O_24_MI_01	50.80	55.42	1.64	14.85	1.03	13.81	0.25	2.80	5.45	3.41	1.04	0.30
H4_O_24_MI_02	50.80	65.09	1.76	16.07	0.31	3.83	0.14	0.59	2.65	7.71	1.52	0.34
H4_O_16_MI_01	53.70	58.48	1.83	18.57	0.37	5.13	0.18	0.95	7.26	5.57	1.18	0.34

Table B.6: Melt inclusions major element contents after PEC correction by Petrolog software.

85

SAMPLE	CO2 [ppm]	H2O [%]	Li [ppm]	B [ppm]	F [ppm]	Cl [ppm]	TiO2 [%]	Rb [ppm]	Sr [ppm]	Y [ppm]	Zr [ppm]	Nb [ppm]	Ba [ppm]
NV19_O_07	1300	0.14	15	66	1054	1033	1.63	44	540	33	175	5	399
NV19_O_03_MI01	732	0.12	11	51	589	1094	1.28	29	533	24	133	3	286
NV19_O_25_MI_01	837	0.11	9	30	427	898	1.24	16	582	23	91	2	218
NV19_O_25_MI_02	882	0.1	15	31	529	922	1.27	20	575	23	92	3	244
NV19_O_19_MI_02	1322	0.13	12	31	470	911	1.25	19	501	21	91	3	246
NV18_O_AK_MI_01	813	0.23	14	39	702	773	1.57	19	553	31	100	3	251
NV19_O_13_MI_01	492	0.11	7	24	204	704	0.91	15	466	15	66	2	180
H4_O_27_MI_01	605	0.14	24	45	563	1220	1.55	18	488	38	121	3	324
H4_PL_AN_MI_01	758	0.01	16	11	180	259	1.31	17	395	29	100	3	280

Table B.7: Secondary Ion Mass Spectrometry analysis of trace and minor elements in melt inclusions from Lonquimay and Navidad samples.

SAMPLE	La [ppm]	Ce [ppm]	Pr [ppm]	Nd [ppm]	Sm [ppm]	Eu [ppm]	Gd [ppm]	Tb [ppm]	Dy [ppm]	Ho [ppm]	Er [ppm]	Tm [ppm]	Yb [ppm]	Lu [ppm]
NV19_O_07	18	43	5.4	27	7	1.1	5.4	1	6.8	1.5	3.7	0.5	3.5	0.5
NV19_O_03_MI01	14	32	4	20.8	4.2	1.2	4.2	0.7	5.2	1	2.5	0.4	2.8	0.4
NV19_O_25_MI_01	10	24	3.6	17.6	4.5	1.4	3.5	0.8	3.9	1	2.3	0.3	2.9	0.3
NV19_O_25_MI_02	11	27	3.7	18.5	4.3	1.8	3.9	0.8	4.7	1	2.5	0.4	2.5	0.3
NV19_O_19_MI_02	10	24	3.5	16.3	4.3	1	3.5	0.7	4.1	0.9	2.8	0.3	2.4	0.2
NV18_O_AK_MI_01	11	28	4.2	21.1	6	1.6	4.9	0.9	5.5	1.3	3.3	0.5	2.7	0.4
NV19_O_13_MI_01	7	17	2.2	10.5	3.2	0.6	3.2	0.5	3	0.6	1.8	0.2	1.8	0.2
H4_O_27_MI_01	16	38	5.5	24.9	7.1	2.7	7	1.1	7.8	1.4	4.1	0.6	4	0.6
H4_PL_AN_MI_01	12	31	4.2	19.5	6.3	1.6	5.2	1	4.9	0.9	3.2	0.4	2.9	0.4

Table B.8: Secondary Ion Mass Spectrometry analysis of rare earth elements in melt inclusions from Lonquimay and Navidad samples.

C

APPENDIX C: RAMAN SPECTRA

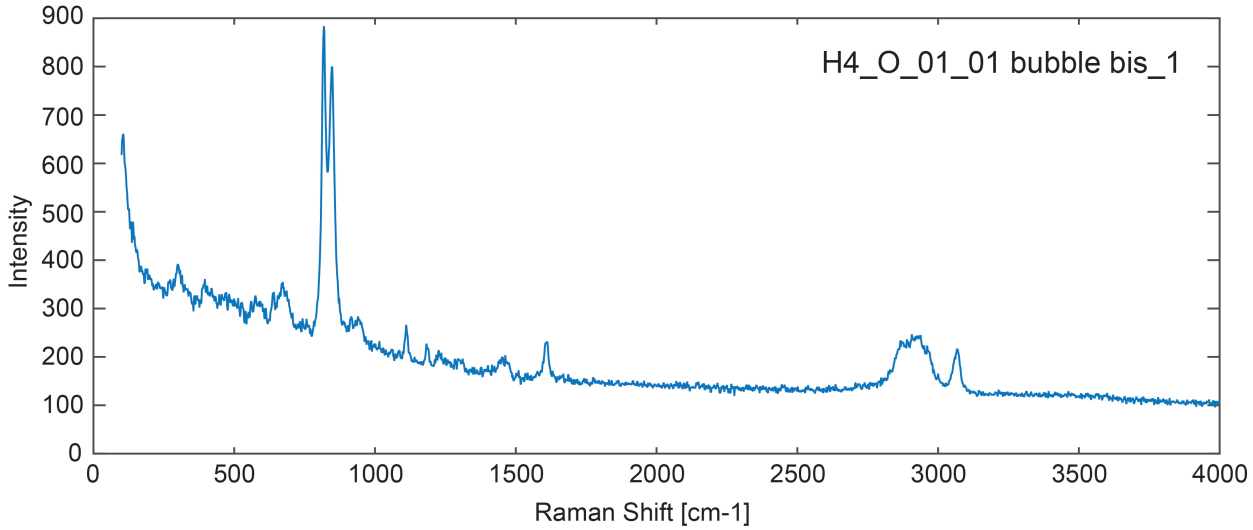
H4_O_01_01 bubble bis_1
Intensity
Raman Shift [cm-1]
0
100
200
300
400
500
600
700
800
900
0
500
1000
1500
2000
2500
3000
3500
4000

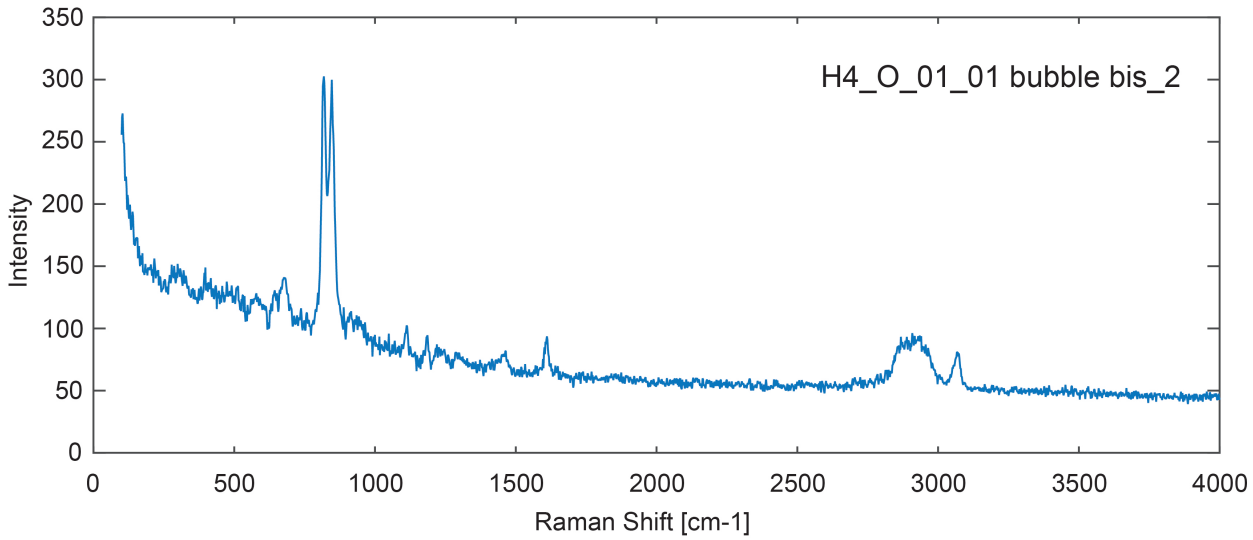
H4_O_01_01 bubble bis_2
Intensity
Raman Shift [cm-1]
0
50
100
150
200
250
300
350
0
500
1000
1500
2000
2500
3000
3500
4000

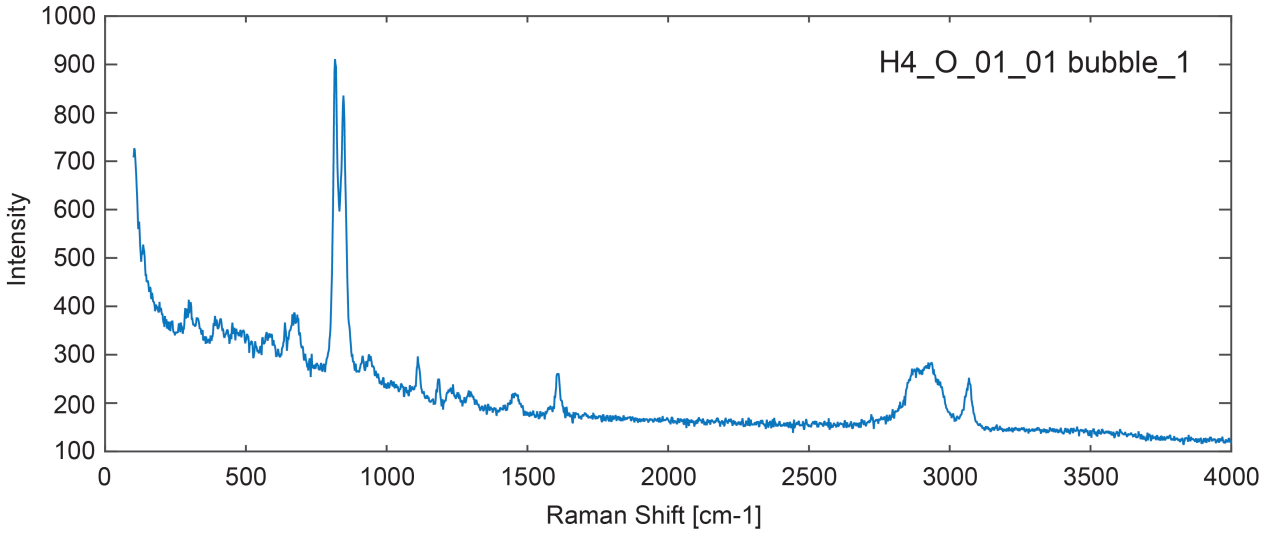
H4_O_01_01 bubble_1
Intensity
Raman Shift [cm-1]
100
200
300
400
500
600
700
800
900
1000
0
500
1000
1500
2000
2500
3000
3500
4000

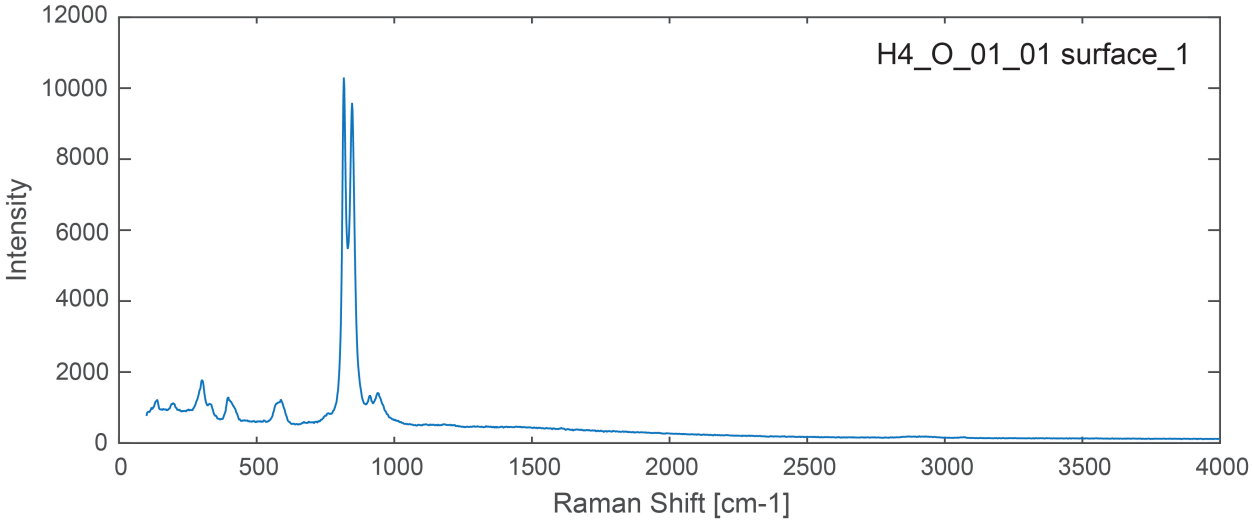
H4_O_01_01 surface_1
Intensity
Raman Shift [cm-1]
0
2000
4000
6000
8000
10000
12000
0
500
1000
1500
2000
2500
3000
3500
4000

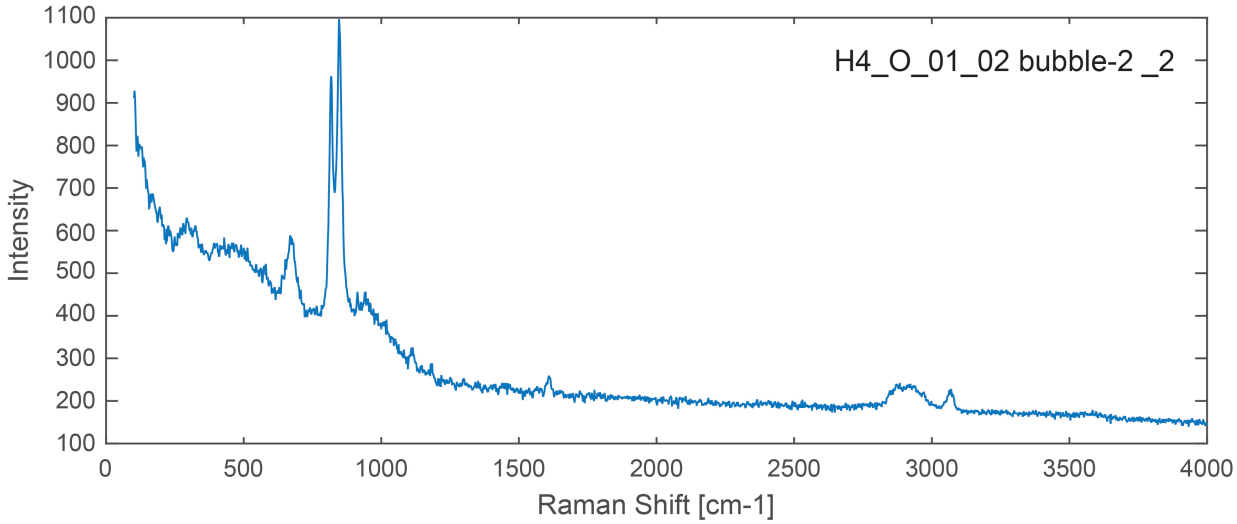
H4_O_01_02 bubble-2 _2
Intensity
Raman Shift [cm-1]
100
200
300
400
500
600
700
800
900
1000
1100
0
500
1000
1500
2000
2500
3000
3500
4000

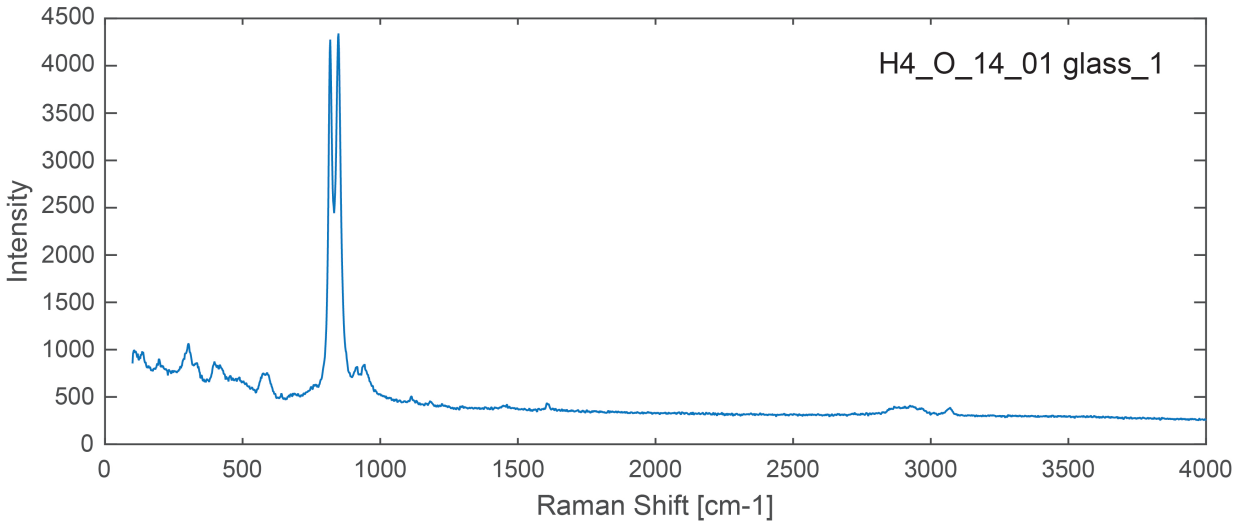
H4_O_14_01 glass_1
Intensity
Raman Shift [cm-1]
0
500
1000
1500
2000
2500
3000
3500
4000
0
500
1000
1500
2000
2500
3000
3500
4000
4500

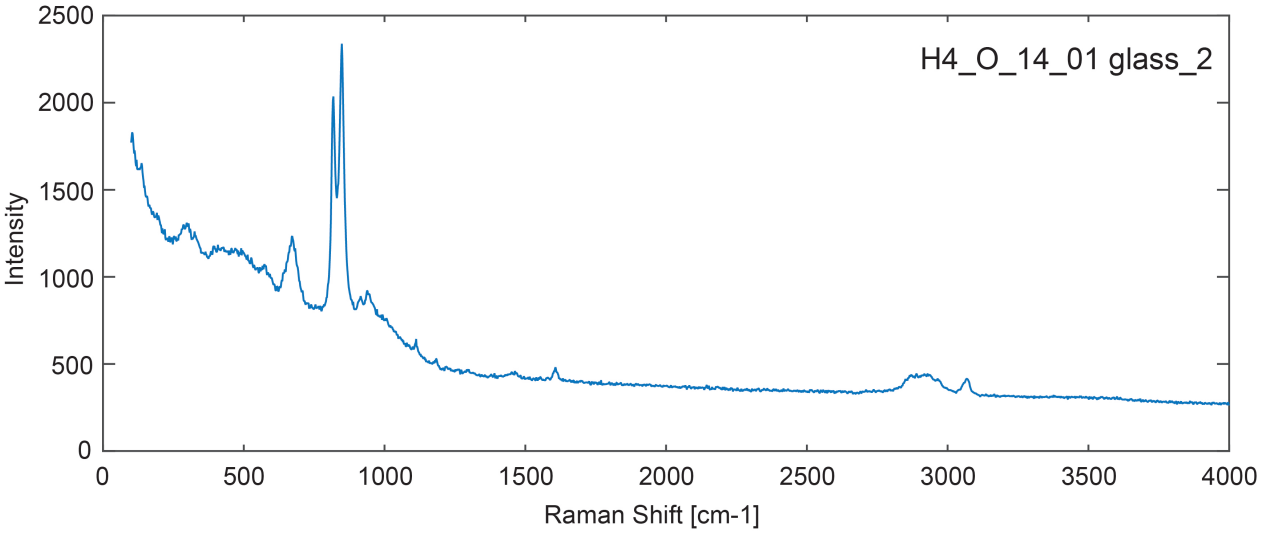
H4_O_14_01 glass_2
Intensity
Raman Shift [cm-1]
0
500
1000
1500
2000
2500
3000
3500
4000

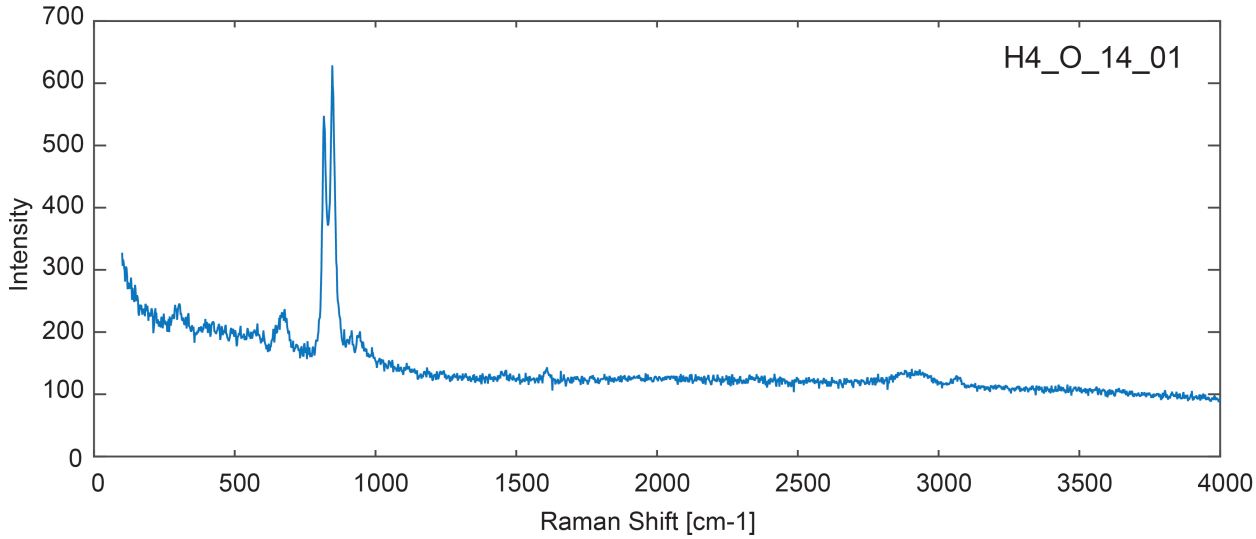
H4_O_14_01
Intensity
Raman Shift [cm-1]
0
100
200
300
400
500
600
700
1000
1500
2000
2500
3000
3500
4000

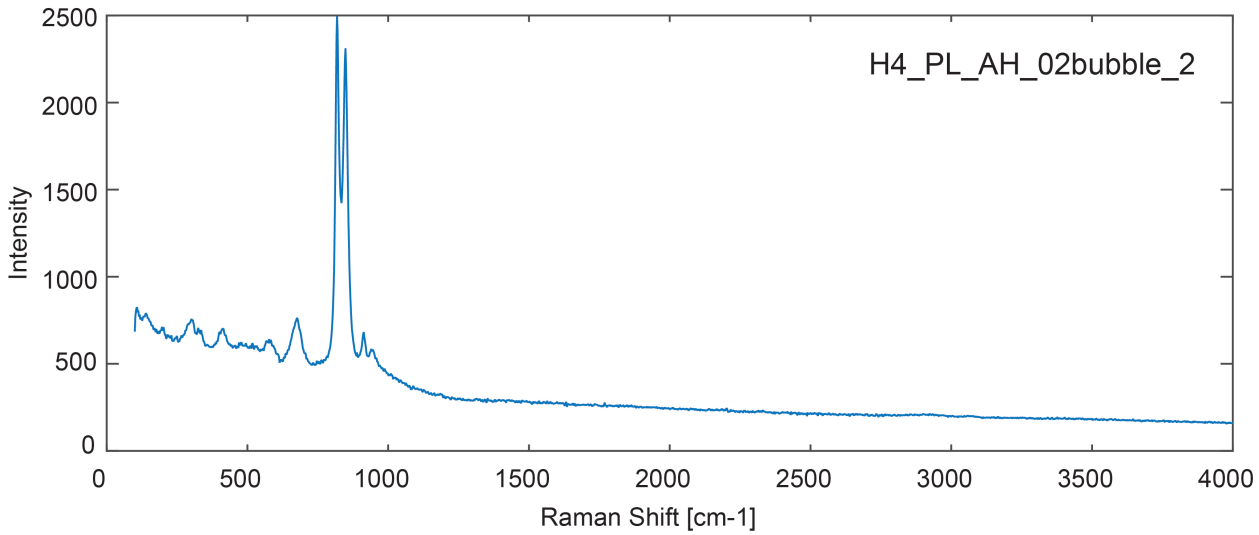
H4_PL_AH_02bubble_2
Intensity
Raman Shift [cm-1]
0
500
1000
1500
2000
2500
3000
3500
4000

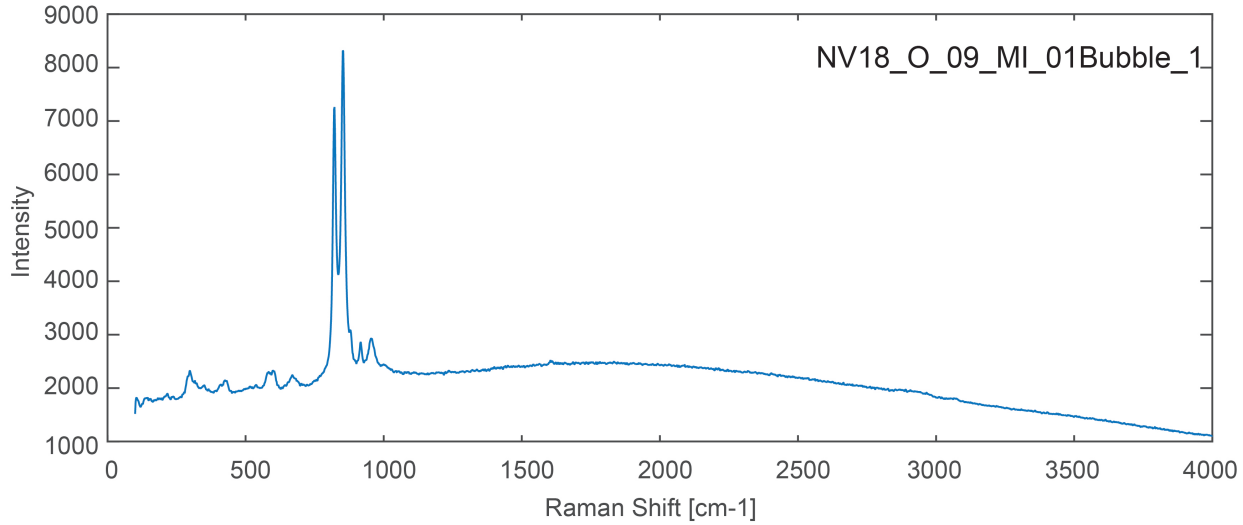
NV18_O_09_MI_01Bubble_1
Intensity
Raman Shift [cm-1]
9000
8000
7000
6000
5000
4000
3000
2000
1000
0
500
1000
1500
2000
2500
3000
3500
4000

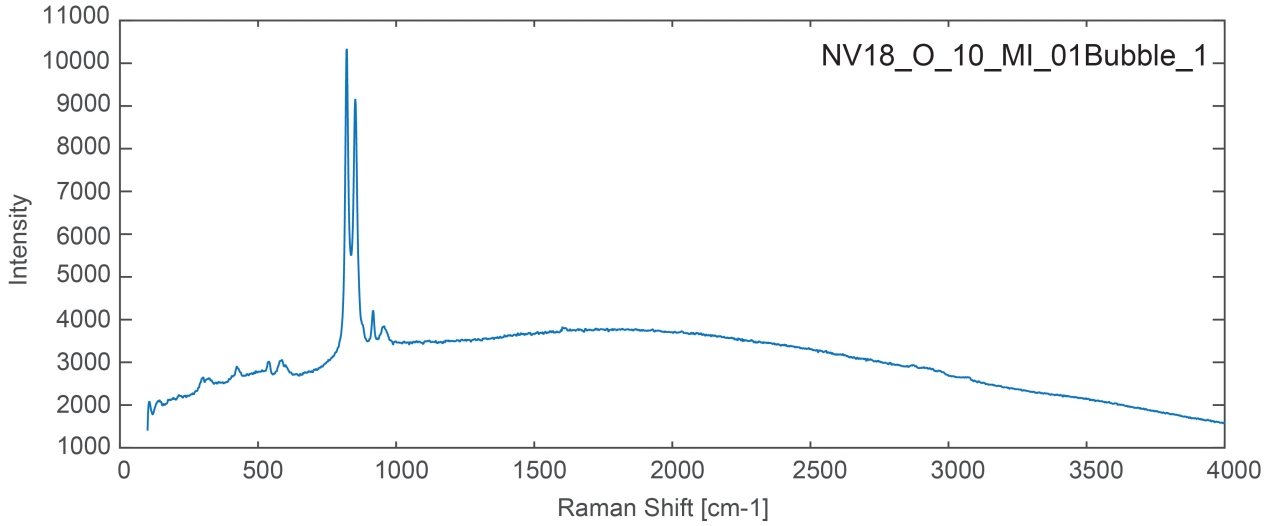
NV18_O_10_MI_01Bubble_1
Intensity
Raman Shift [cm-1]
11000
10000
9000
8000
7000
6000
5000
4000
3000
2000
1000
0
500
1000
1500
2000
2500
3000
3500
4000

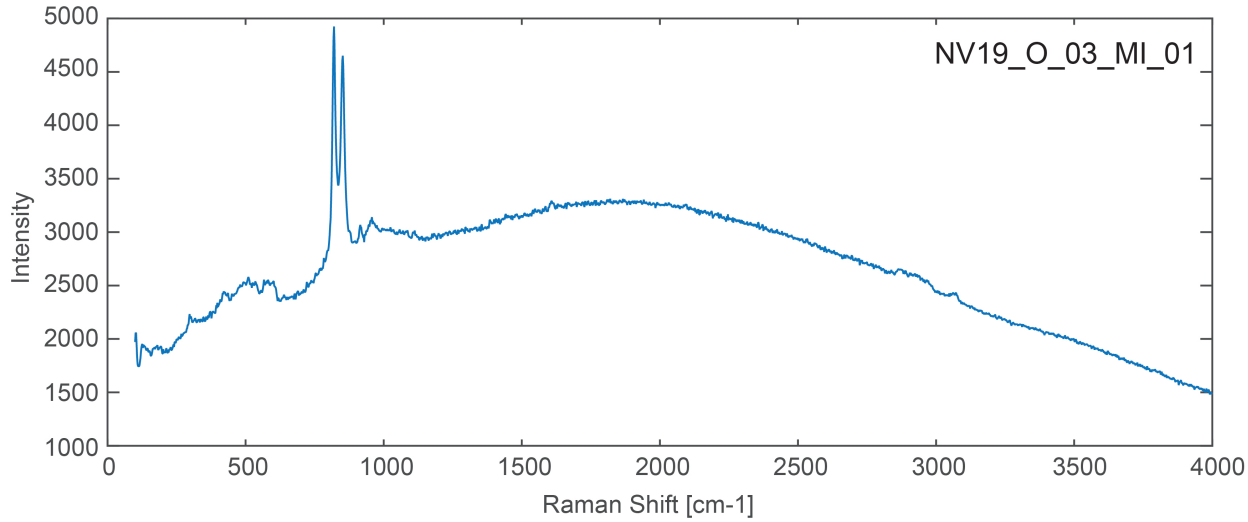
NV19_O_03_MI_01
Intensity
Raman Shift [cm-1]
5000
4500
4000
3500
3000
2500
2000
1500
1000
0
500
1000
1500
2000
2500
3000
3500
4000

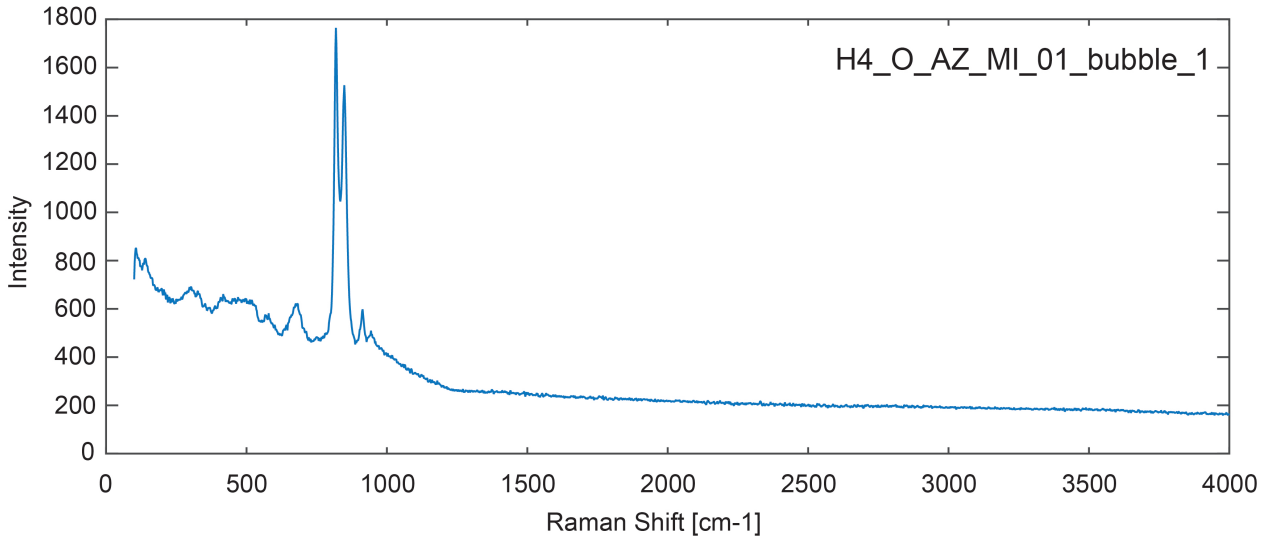
H4_O_AZ_MI_01_bubble_1
Intensity
Raman Shift [cm-1]
0
200
400
600
800
1000
1200
1400
1600
1800
0
500
1000
1500
2000
2500
3000
3500
4000

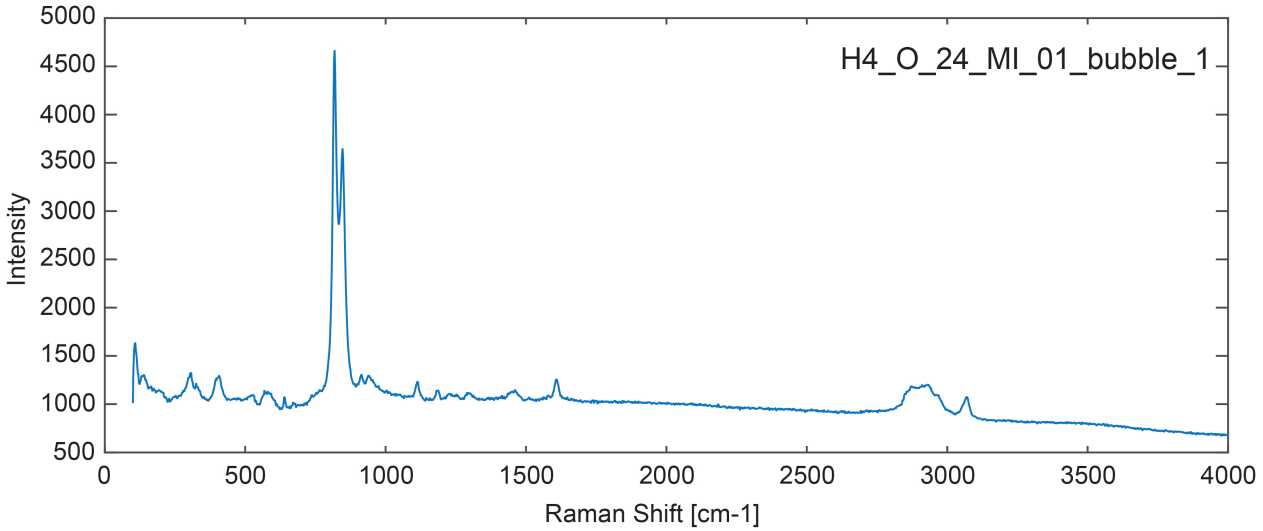
H4_O_24_MI_01_bubble_1
Intensity
Raman Shift [cm-1]
500
1000
1500
2000
2500
3000
3500
4000
4500
5000
0
500
1000
1500
2000
2500
3000
3500
4000

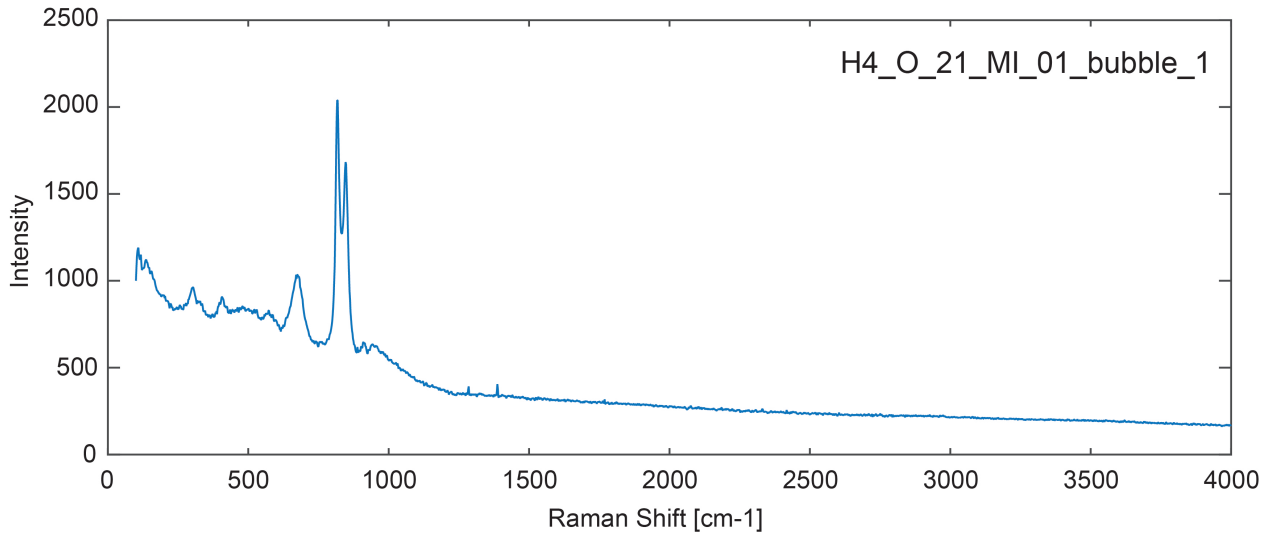
H4_O_21_MI_01_bubble_1
Intensity
Raman Shift [cm-1]
0
500
1000
1500
2000
2500
0
500
1000
1500
2000
2500
3000
3500
4000

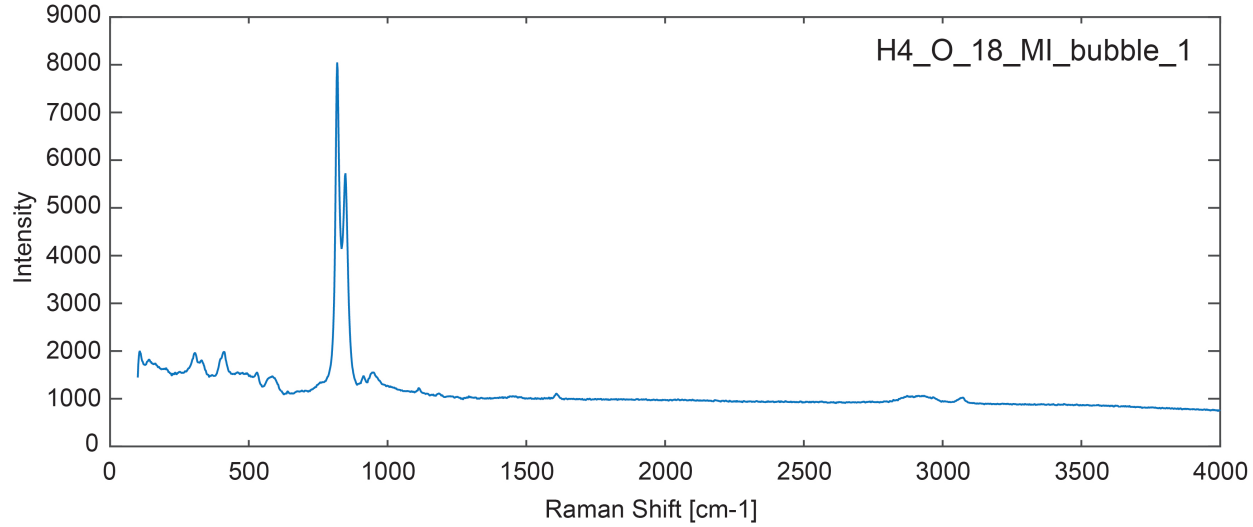
H4_O_18_MI_bubble_1
Intensity
Raman Shift [cm-1]
0
1000
2000
3000
4000
5000
6000
7000
8000
9000
0
500
1000
1500
2000
2500
3000
3500
4000

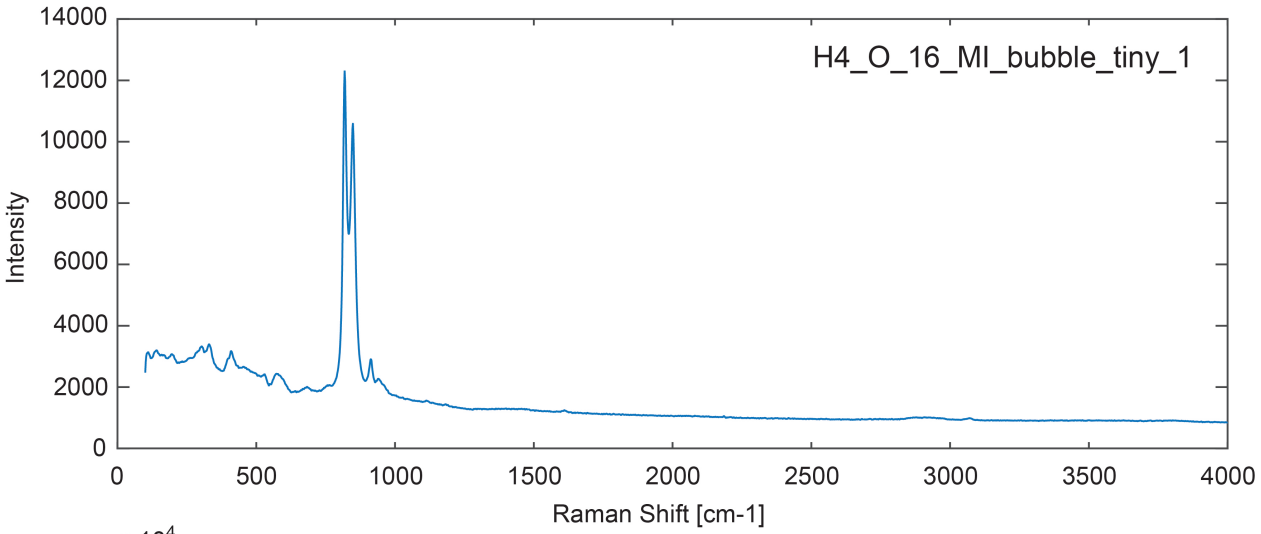
H4_O_16_MI_bubble_tiny_1
Intensity
Raman Shift [cm-1]
0
2000
4000
6000
8000
10000
12000
14000
0
500
1000
1500
2000
2500
3000
3500
4000

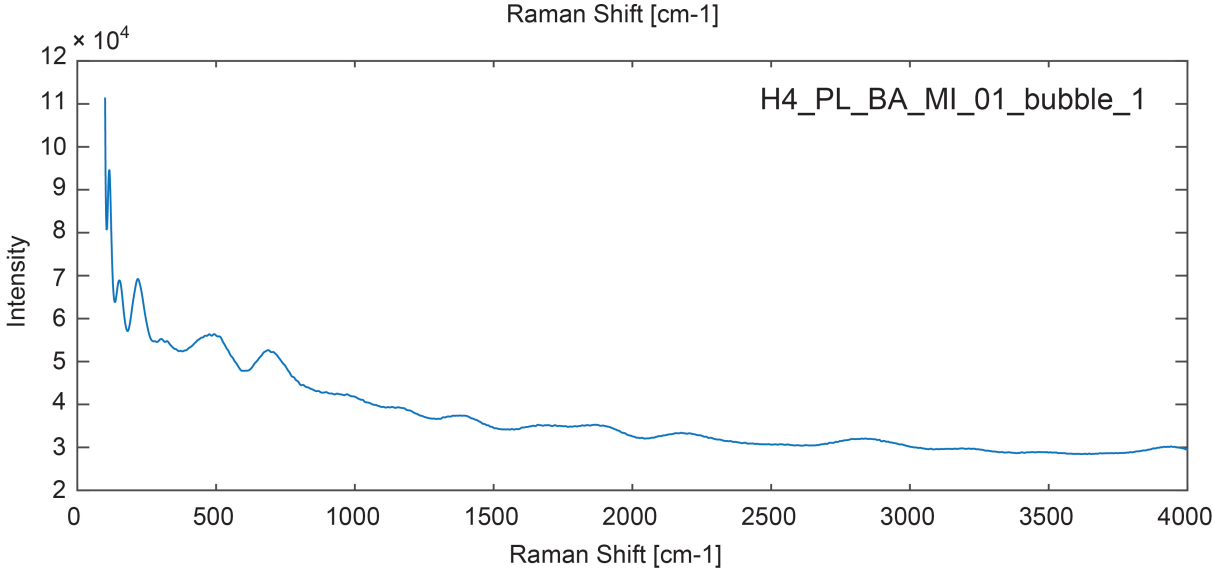
H4_PL_BA_MI_01_bubble_1
× 10^4
Intensity
Raman Shift [cm-1]
2
3
4
5
6
7
8
9
10
11
12
0
500
1000
1500
2000
2500
3000
3500
4000

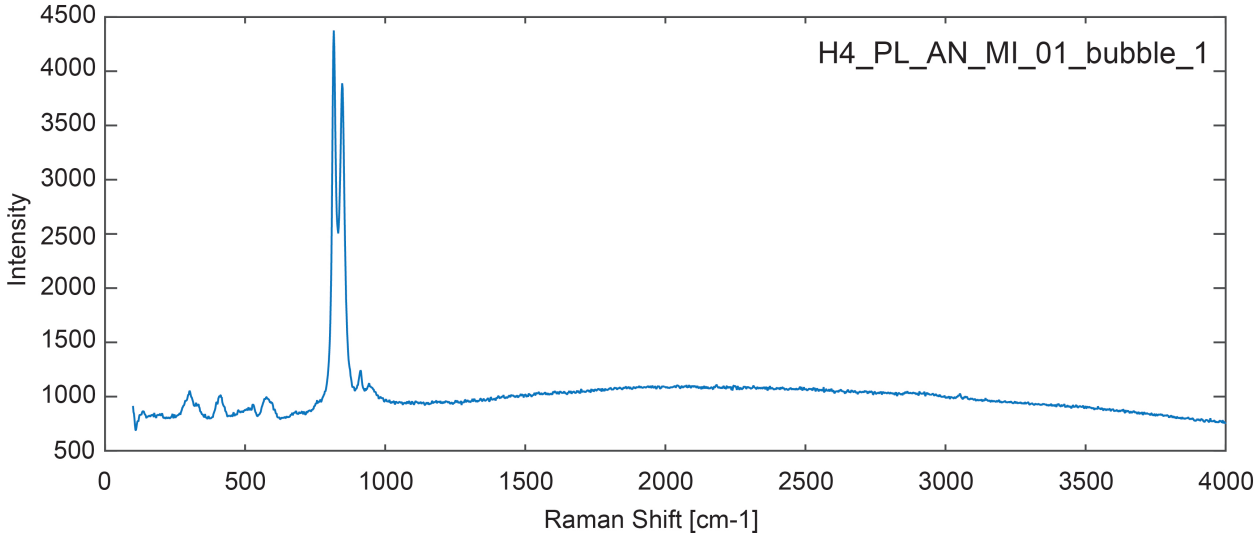
H4_PL_AN_MI_01_bubble_1
Intensity
Raman Shift [cm-1]
4500
4000
3500
3000
2500
2000
1500
1000
500
0
500
1000
1500
2000
2500
3000
3500
4000

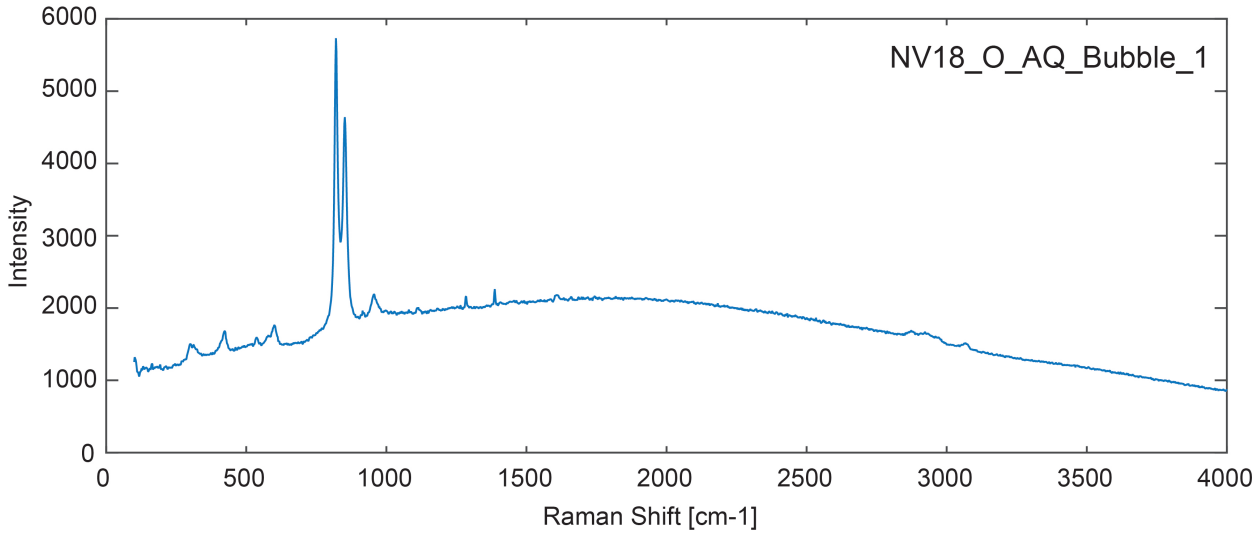
NV18_O_AQ_Bubble_1
Intensity
Raman Shift [cm-1]
6000
5000
4000
3000
2000
1000
0
500
1000
1500
2000
2500
3000
3500
4000

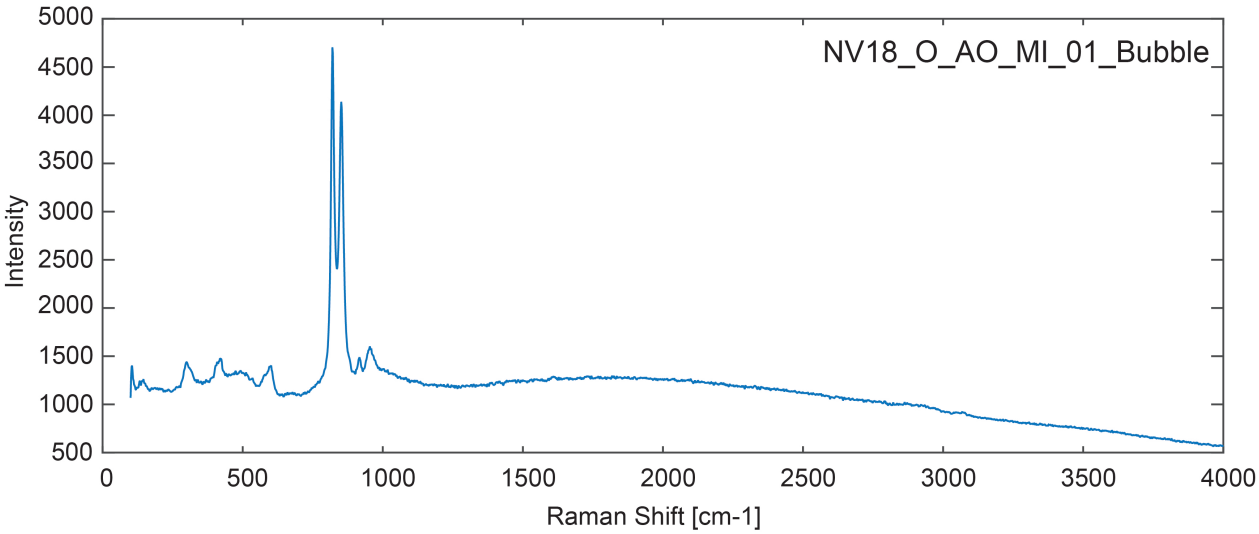
NV18_O_AO_MI_01_Bubble_
Intensity
Raman Shift [cm-1]
5000
4500
4000
3500
3000
2500
2000
1500
1000
500
0
500
1000
1500
2000
2500
3000
3500
4000

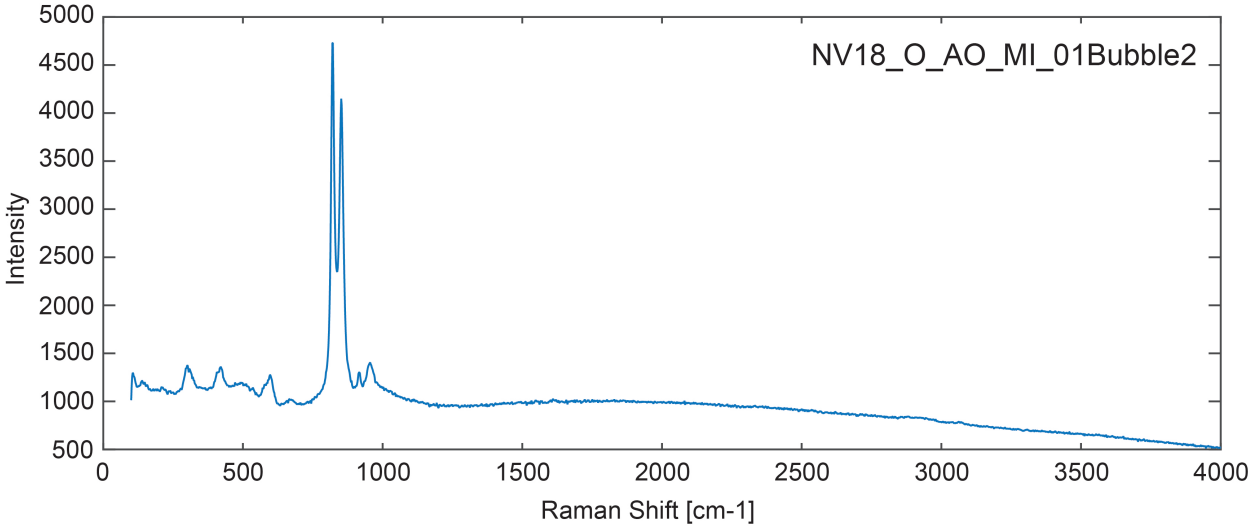
NV18_O_AO_MI_01Bubble2
Intensity
Raman Shift [cm-1]
5000
4500
4000
3500
3000
2500
2000
1500
1000
500
0
500
1000
1500
2000
2500
3000
3500
4000

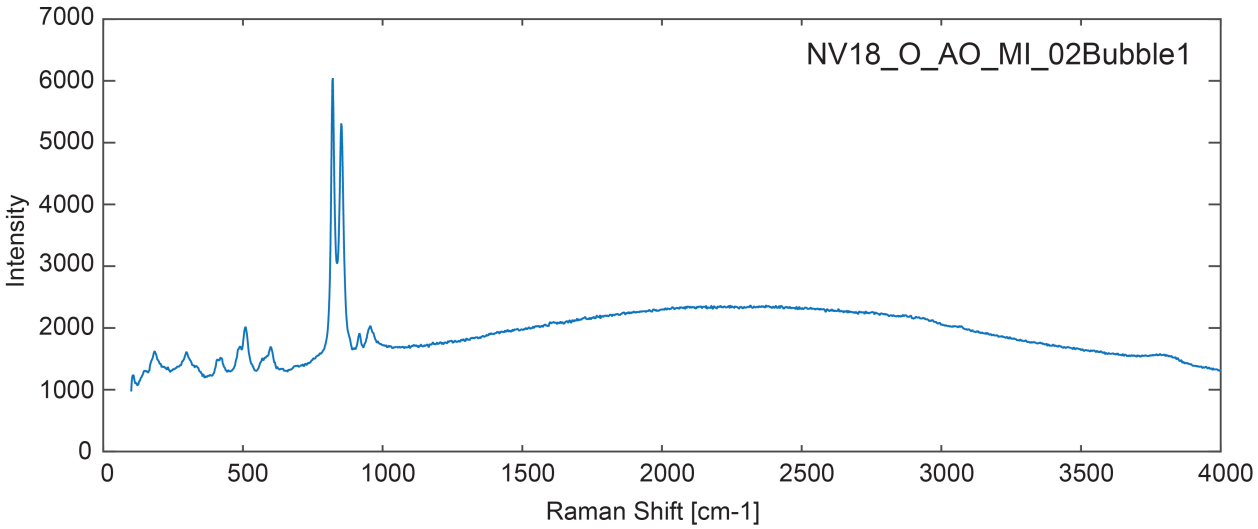
NV18_O_AO_MI_02Bubble1
Intensity
Raman Shift [cm-1]
7000
6000
5000
4000
3000
2000
1000
0
500
1000
1500
2000
2500
3000
3500
4000

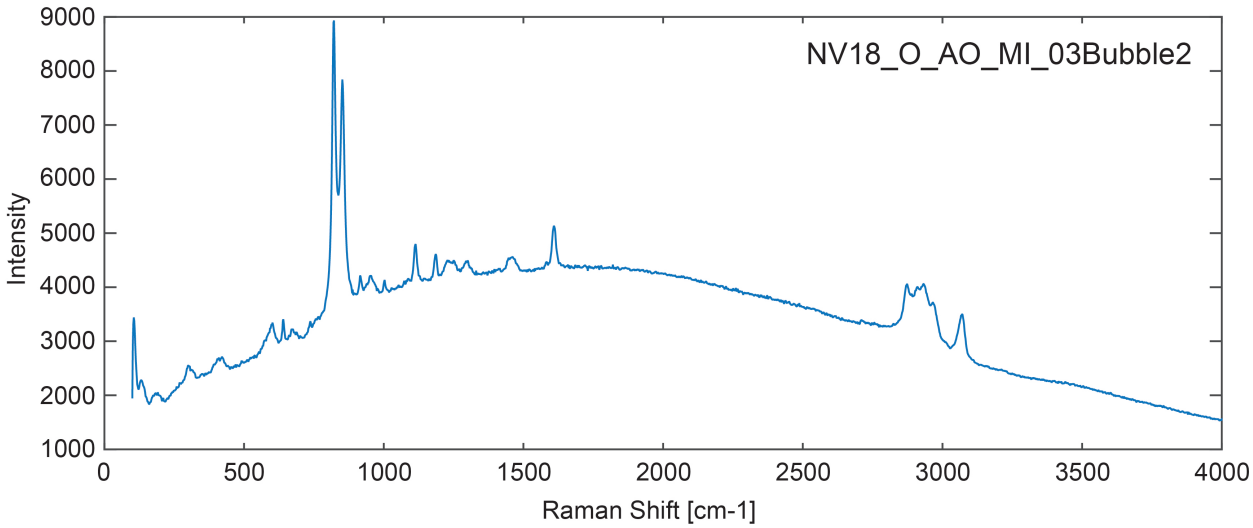
NV18_O_AO_MI_03Bubble2
Intensity
Raman Shift [cm-1]
9000
8000
7000
6000
5000
4000
3000
2000
1000
0
500
1000
1500
2000
2500
3000
3500
4000

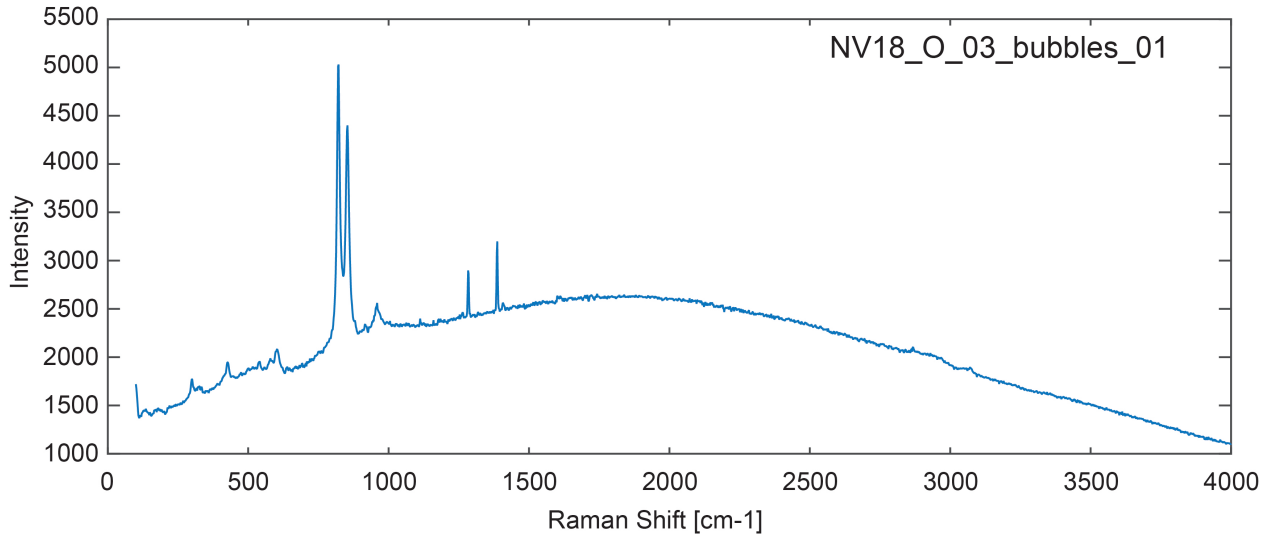
NV18_O_03_bubbles_01
Intensity
Raman Shift [cm-1]

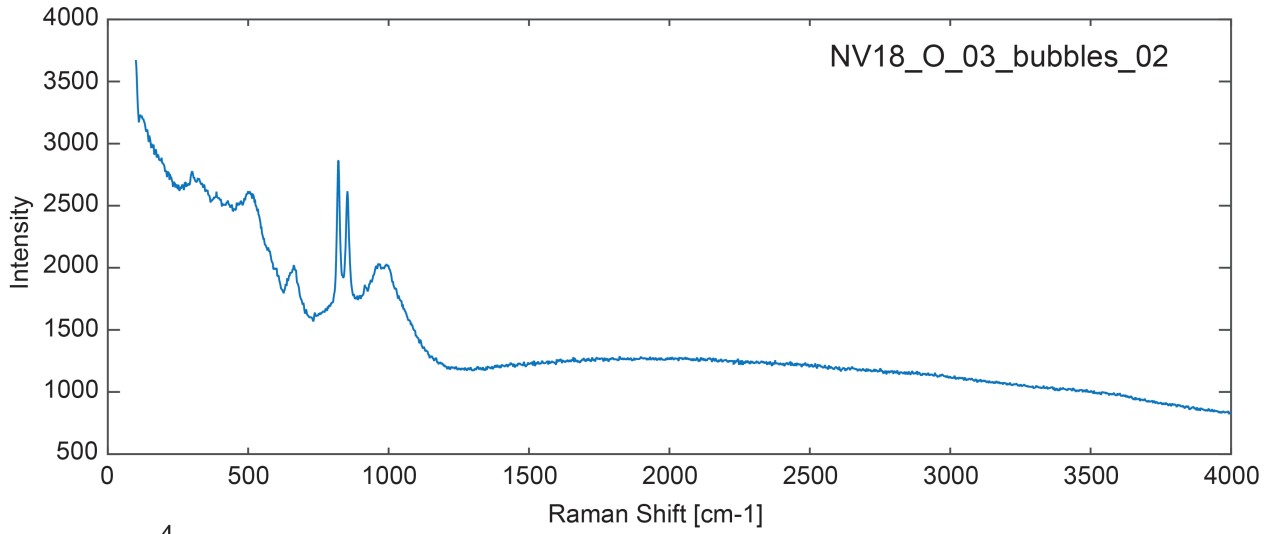
NV18_O_03_bubbles_02
Intensity
Raman Shift [cm-1]

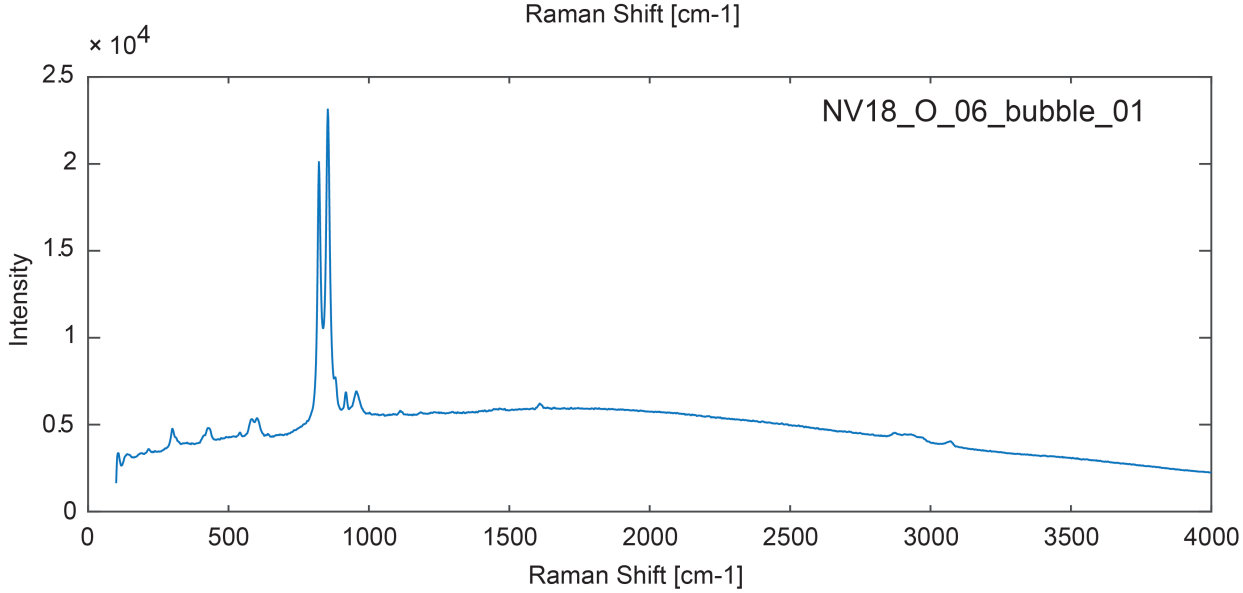
× 10^4
NV18_O_06_bubble_01
Intensity
Raman Shift [cm-1]

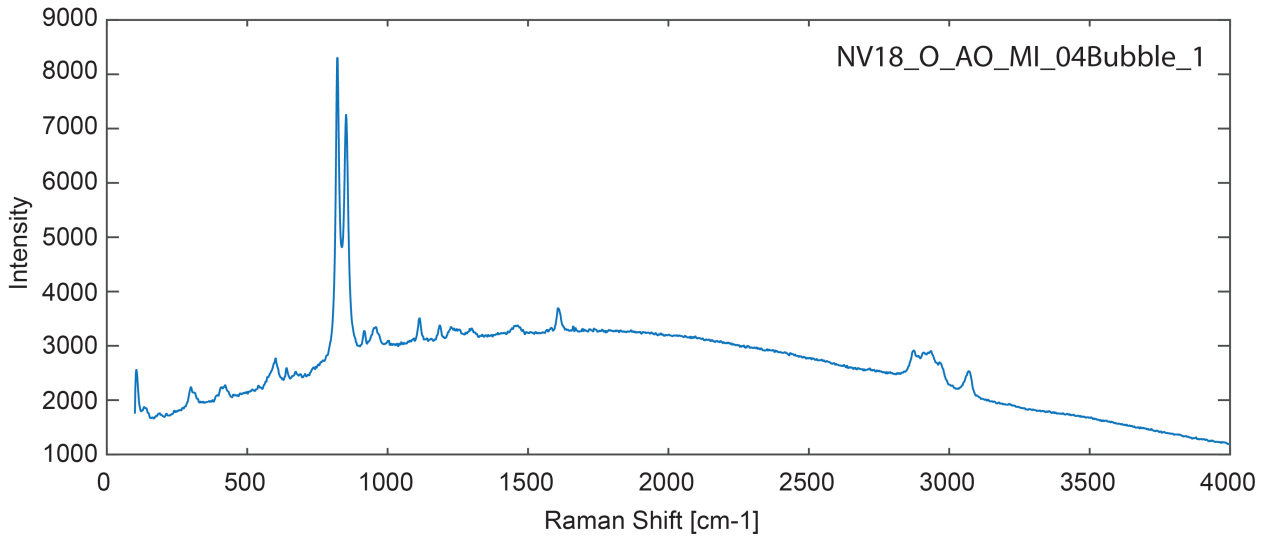
NV18_O_AO_MI_04Bubble_1
Intensity
Raman Shift [cm-1]
9000
8000
7000
6000
5000
4000
3000
2000
1000
0
500
1000
1500
2000
2500
3000
3500
4000

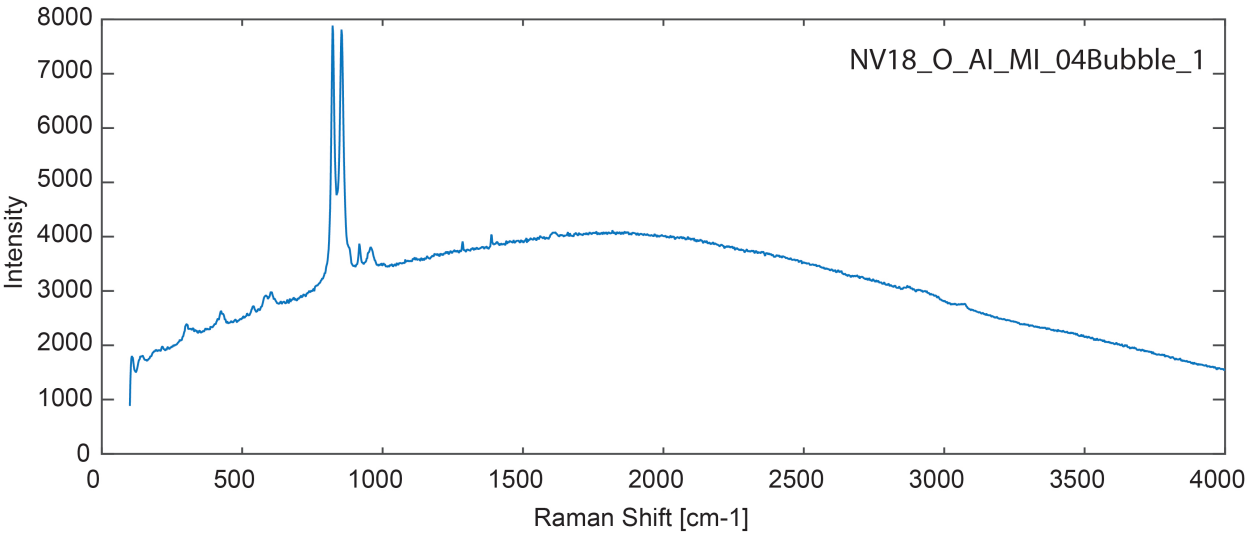
NV18_O_AI_MI_04Bubble_1
Intensity
Raman Shift [cm-1]
8000
7000
6000
5000
4000
3000
2000
1000
0
500
1000
1500
2000
2500
3000
3500
4000

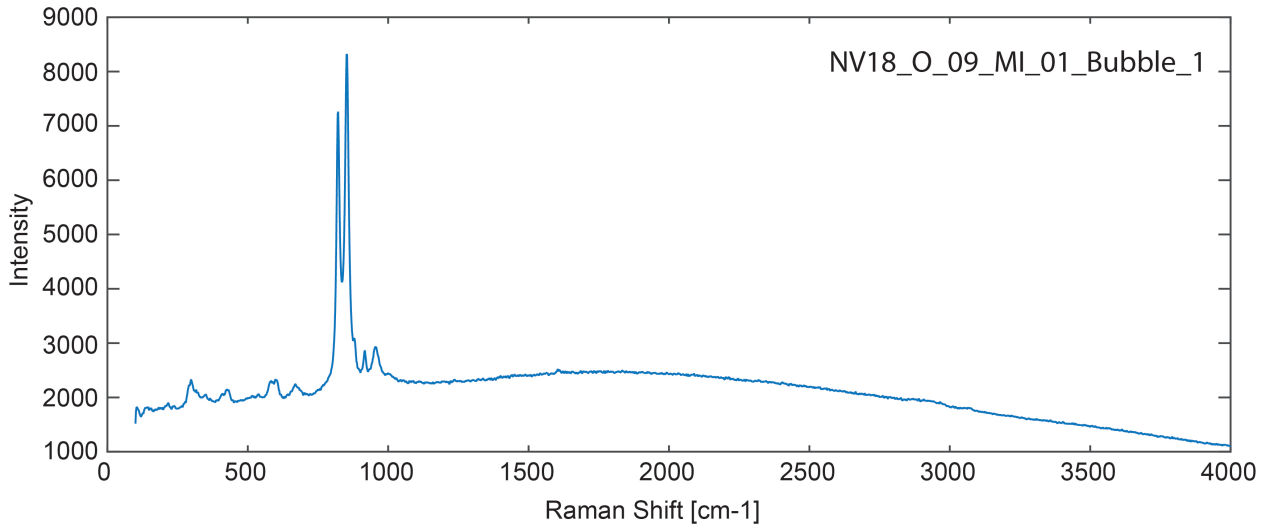
NV18_O_09_MI_01_Bubble_1
Intensity
Raman Shift [cm-1]
9000
8000
7000
6000
5000
4000
3000
2000
1000
0
500
1000
1500
2000
2500
3000
3500
4000

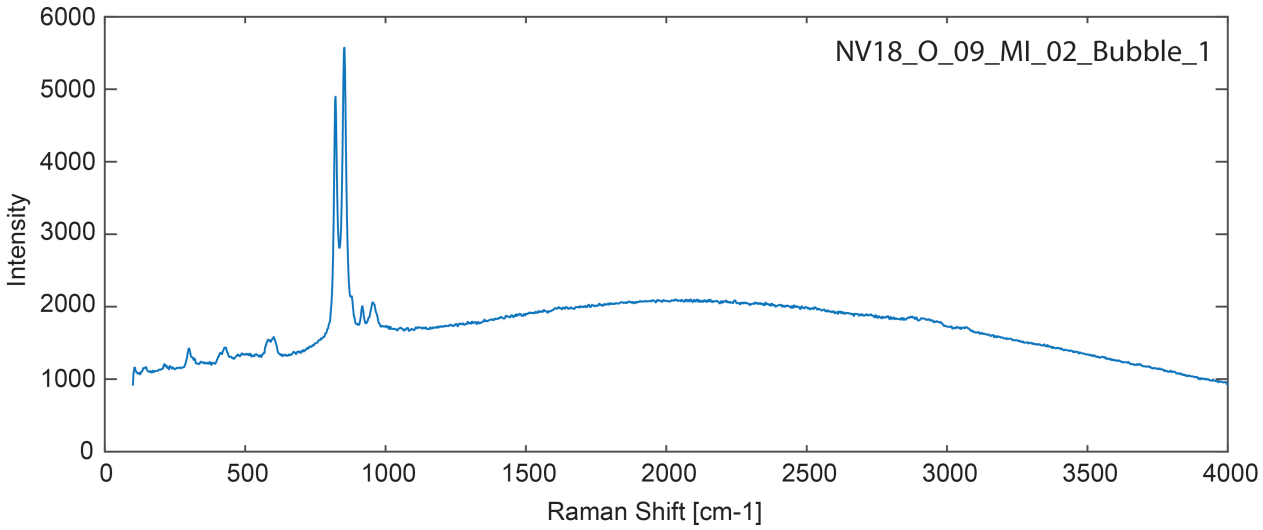
NV18_O_09_MI_02_Bubble_1
Intensity
Raman Shift [cm-1]
0
1000
2000
3000
4000
5000
6000
0
500
1000
1500
2000
2500
3000
3500
4000

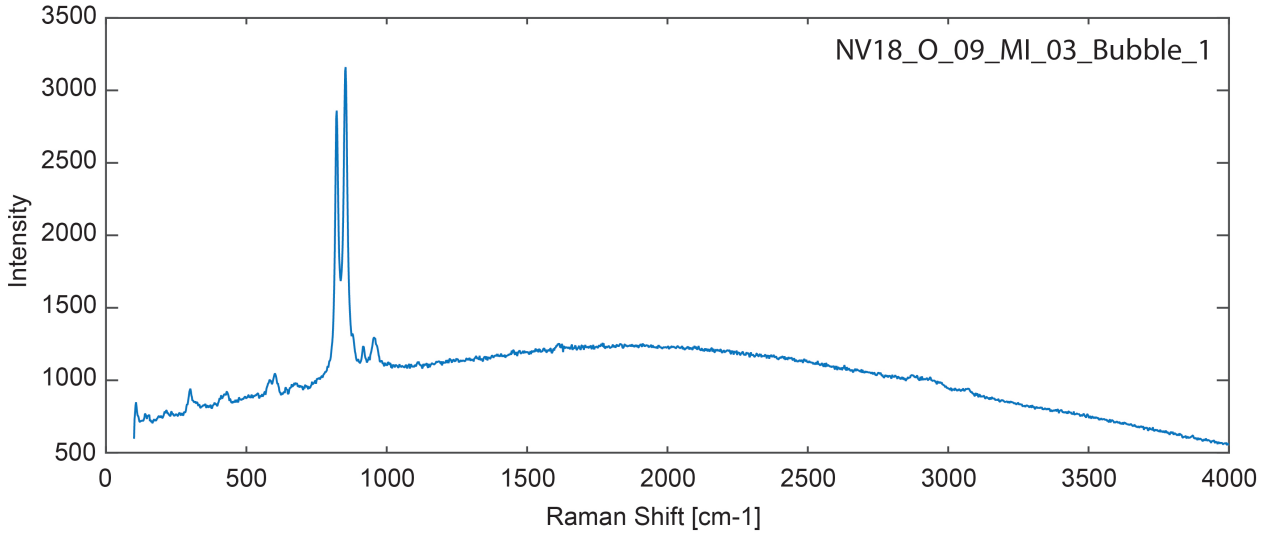
NV18_O_09_MI_03_Bubble_1
Intensity
Raman Shift [cm-1]
500
1000
1500
2000
2500
3000
3500
0
500
1000
1500
2000
2500
3000
3500
4000

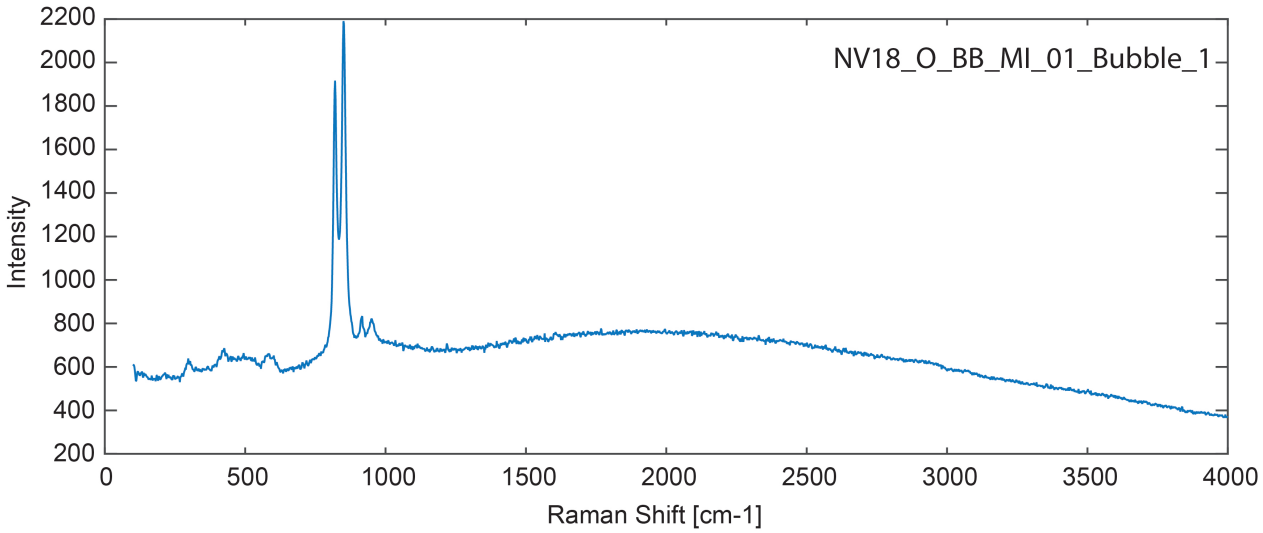
NV18_O_BB_MI_01_Bubble_1
Intensity
Raman Shift [cm-1]
200
400
600
800
1000
1200
1400
1600
1800
2000
2200
0
500
1000
1500
2000
2500
3000
3500
4000

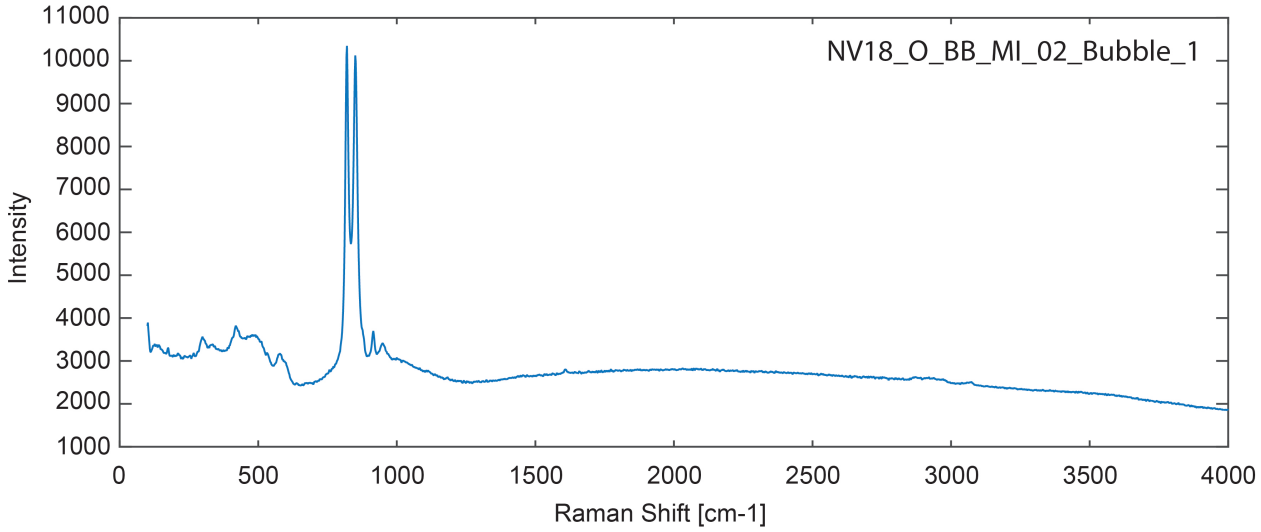
NV18_O_BB_MI_02_Bubble_1
Intensity
Raman Shift [cm-1]
11000
10000
9000
8000
7000
6000
5000
4000
3000
2000
1000
0
500
1000
1500
2000
2500
3000
3500
4000

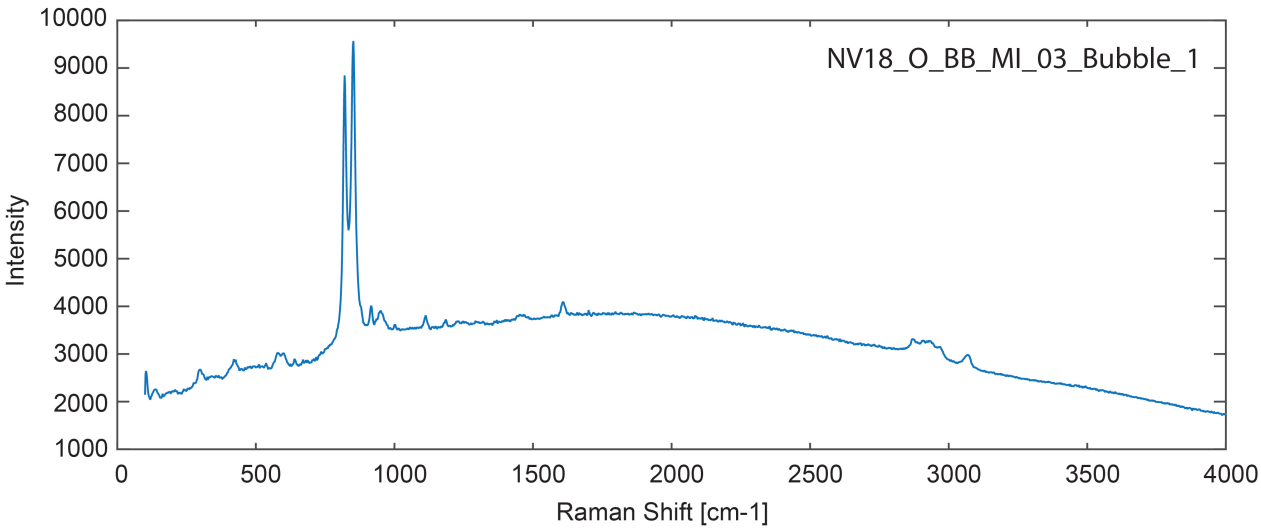
NV18_O_BB_MI_03_Bubble_1
Intensity
Raman Shift [cm-1]
10000
9000
8000
7000
6000
5000
4000
3000
2000
1000
0
500
1000
1500
2000
2500
3000
3500
4000

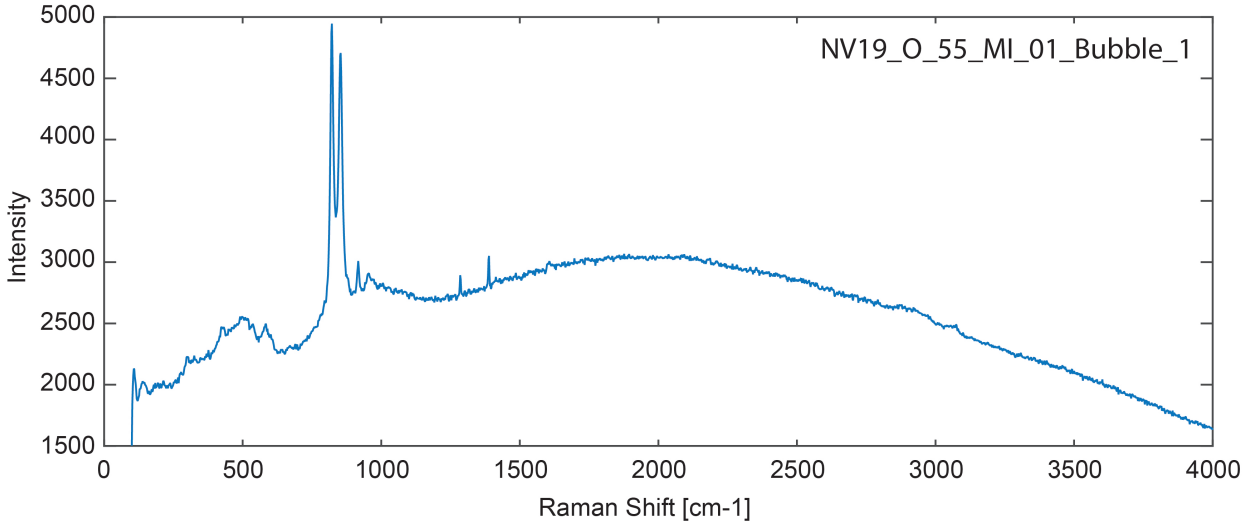
NV19_O_55_MI_01_Bubble_1
Intensity
Raman Shift [cm-1]
5000
4500
4000
3500
3000
2500
2000
1500
0
500
1000
1500
2000
2500
3000
3500
4000

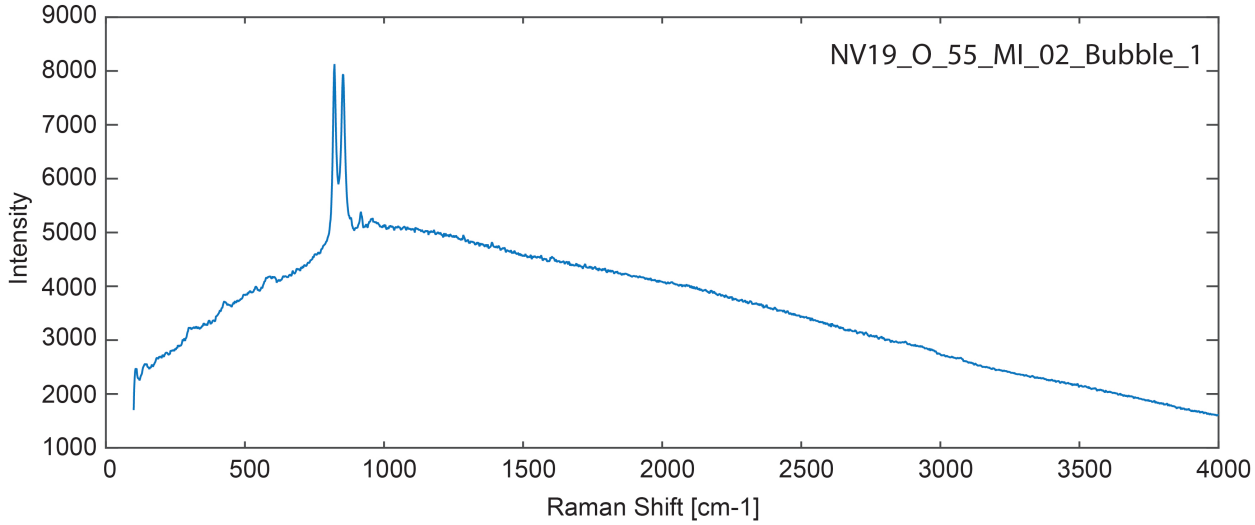
NV19_O_55_MI_02_Bubble_1
Intensity
Raman Shift [cm-1]

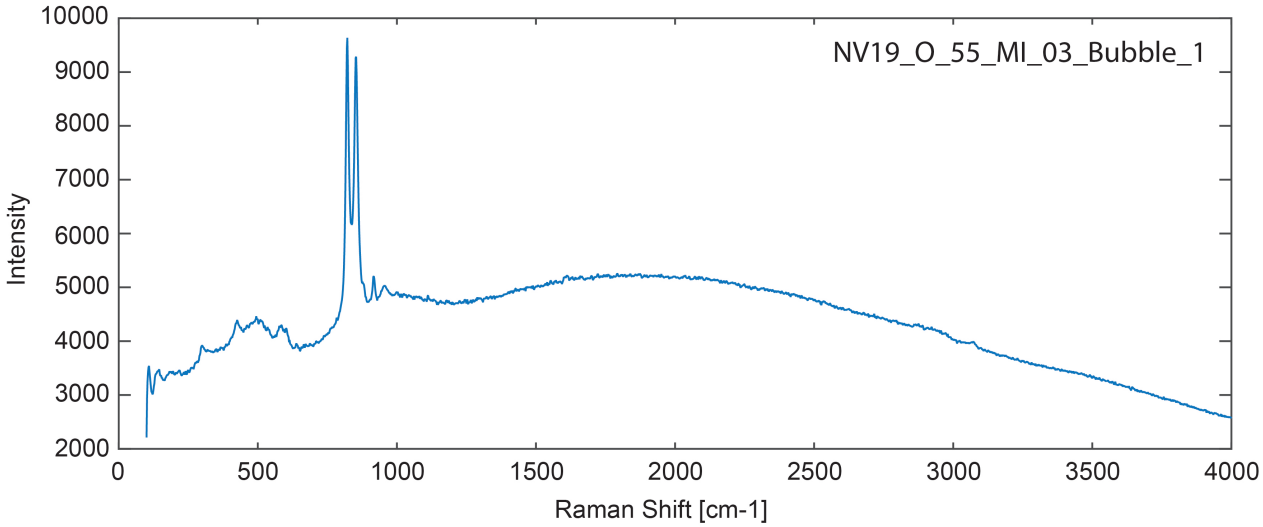
NV19_O_55_MI_03_Bubble_1
Intensity
Raman Shift [cm-1]

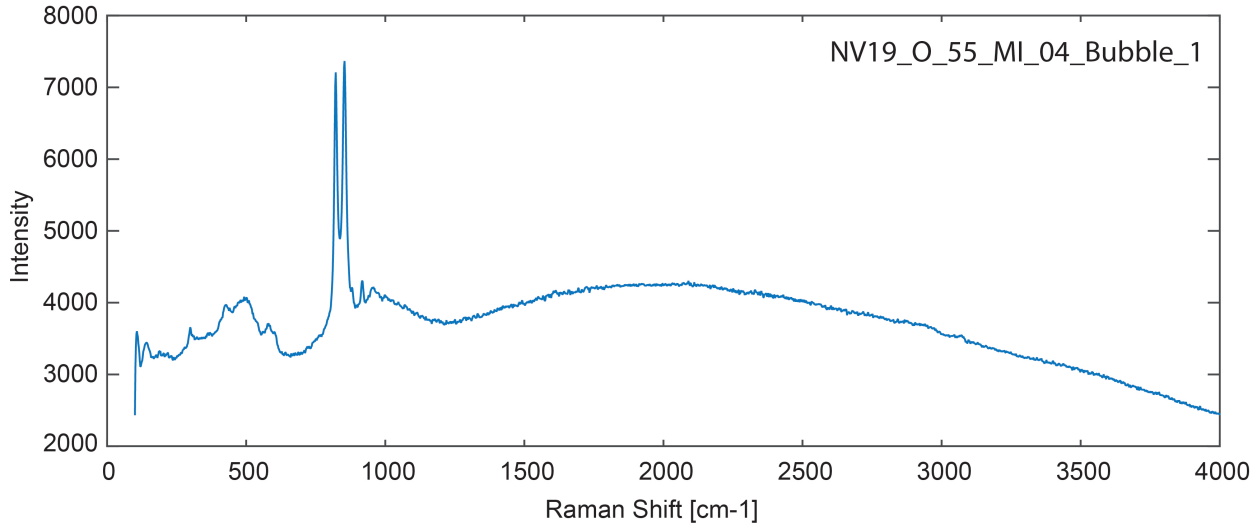
NV19_O_55_MI_04_Bubble_1
Intensity
Raman Shift [cm-1]

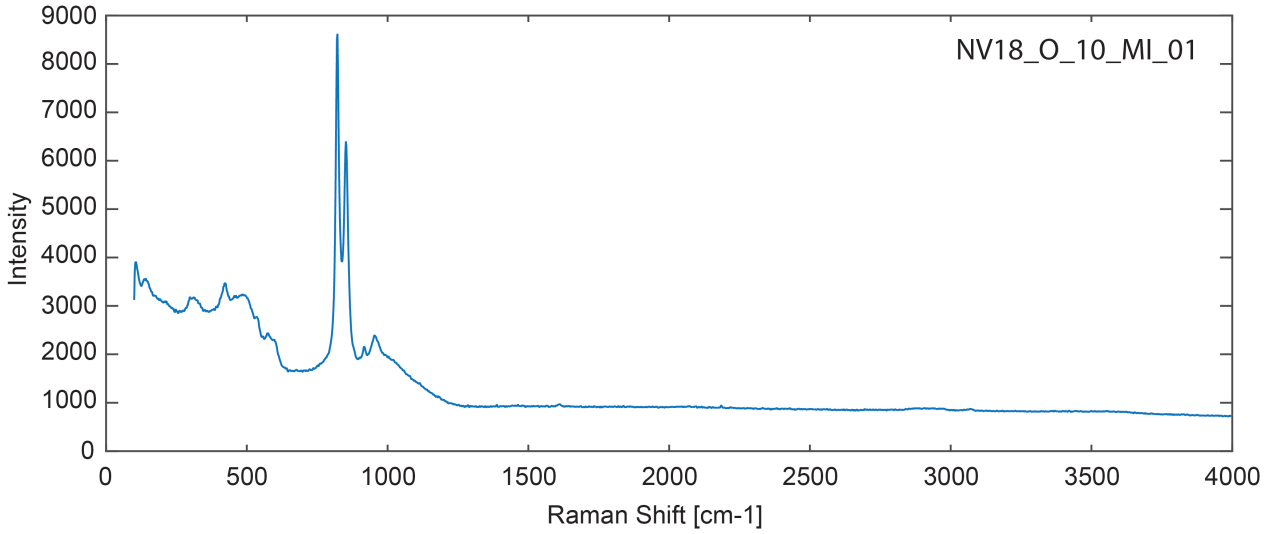
NV18_O_10_MI_01
Intensity
Raman Shift [cm-1]
0
1000
2000
3000
4000
5000
6000
7000
8000
9000
0
500
1000
1500
2000
2500
3000
3500
4000

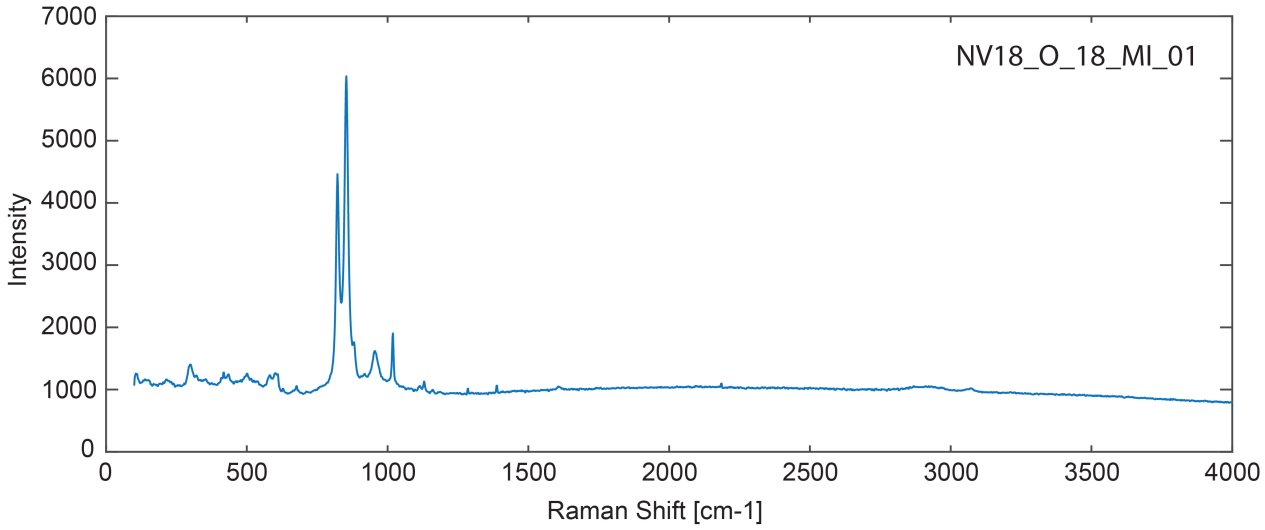
NV18_O_18_MI_01
Intensity
Raman Shift [cm-1]
0
1000
2000
3000
4000
5000
6000
7000
0
500
1000
1500
2000
2500
3000
3500
4000

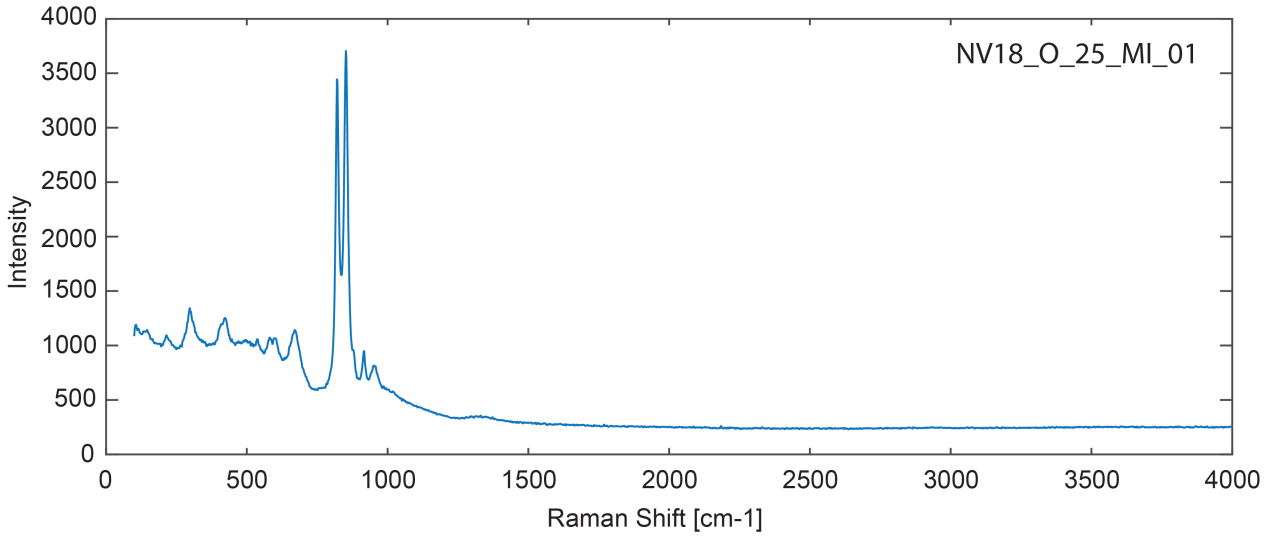
NV18_O_25_MI_01
Intensity
Raman Shift [cm-1]
0
500
1000
1500
2000
2500
3000
3500
4000
0
500
1000
1500
2000
2500
3000
3500
4000

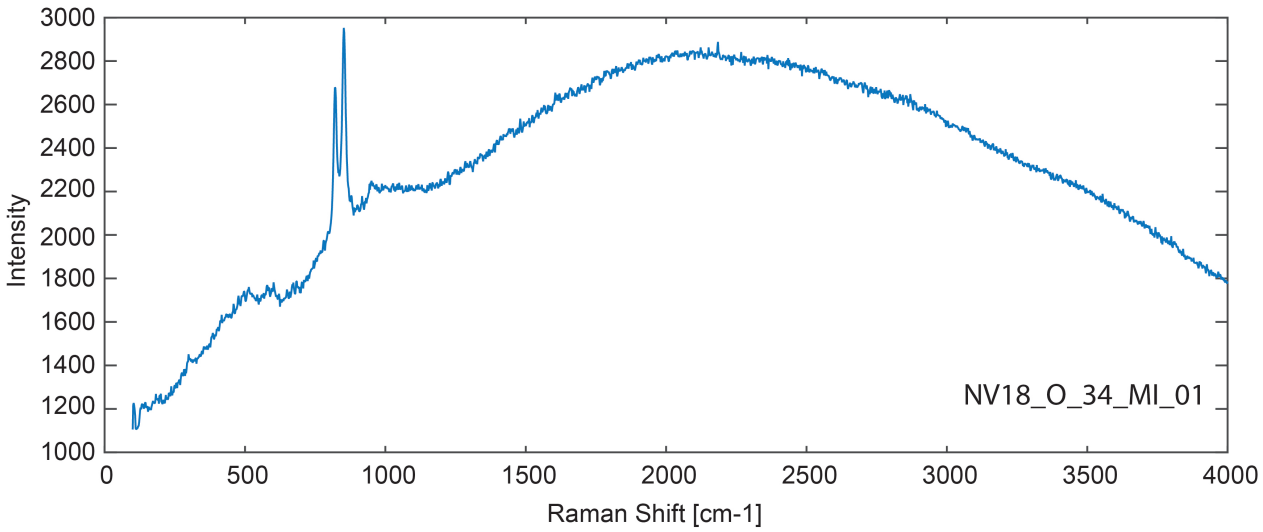
NV18_O_34_MI_01
Intensity
Raman Shift [cm-1]

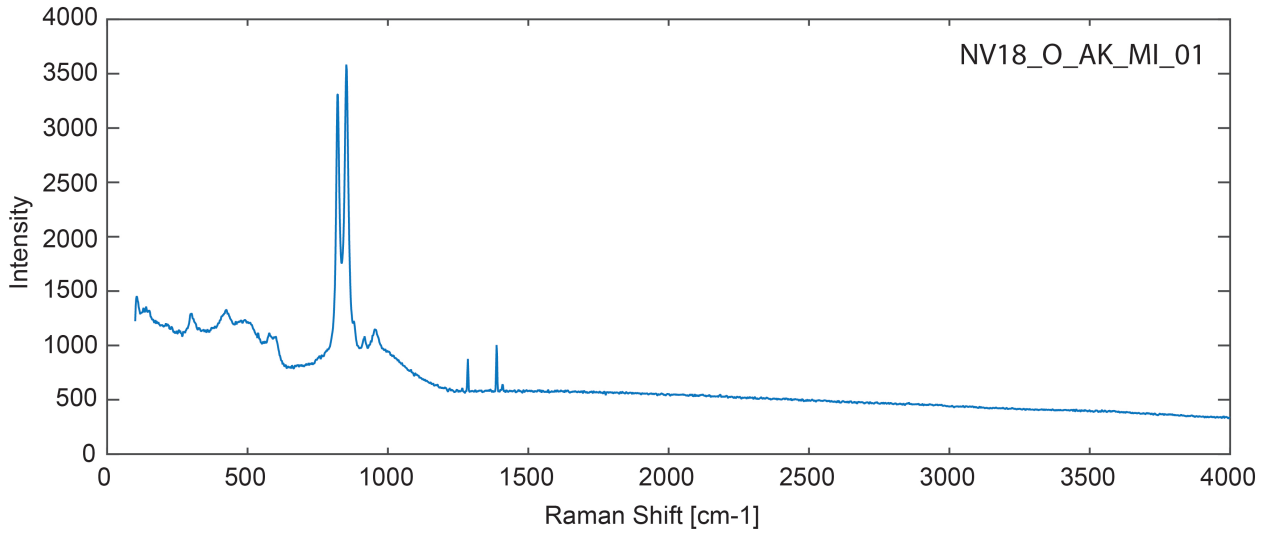
NV18_O_AK_MI_01
Intensity
Raman Shift [cm-1]

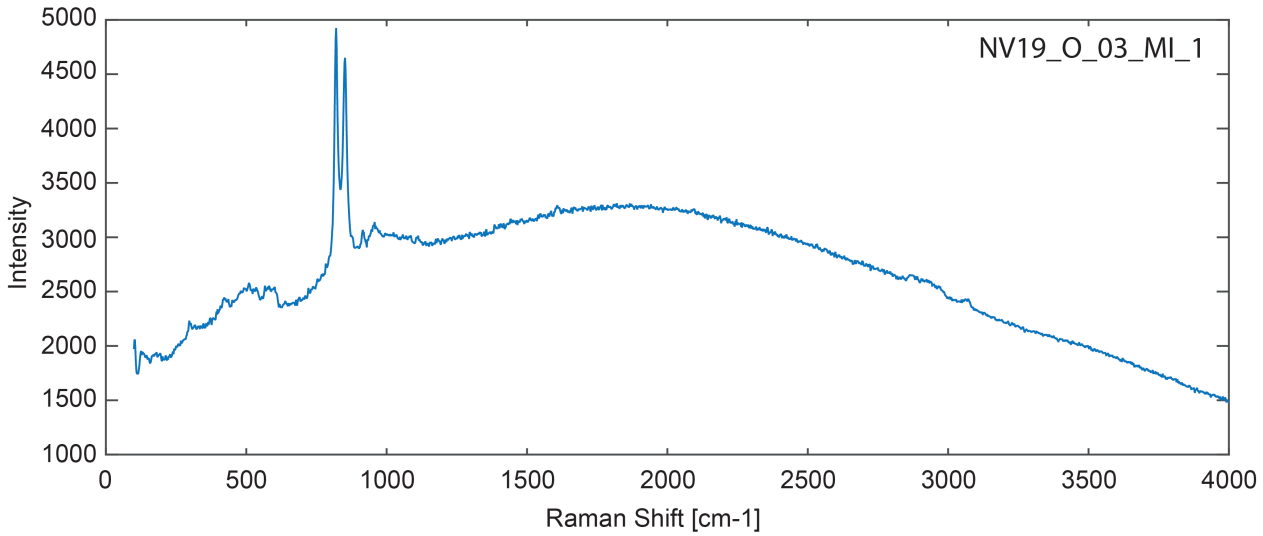
NV19_O_03_MI_1
Intensity
Raman Shift [cm-1]

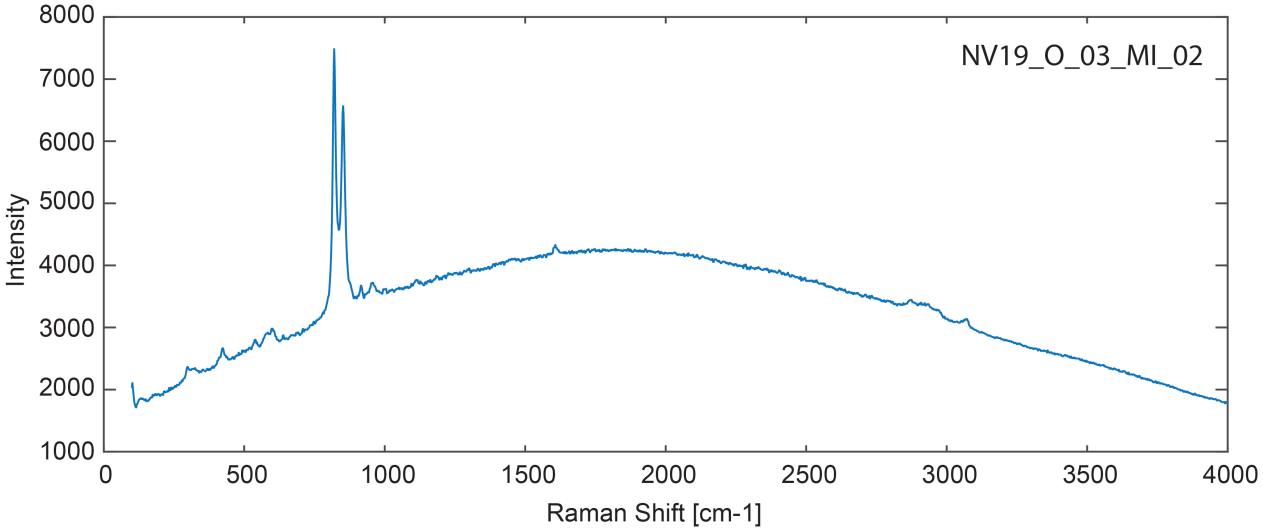
NV19_O_03_MI_02
Intensity
Raman Shift [cm-1]
8000
7000
6000
5000
4000
3000
2000
1000
0
500
1000
1500
2000
2500
3000
3500
4000

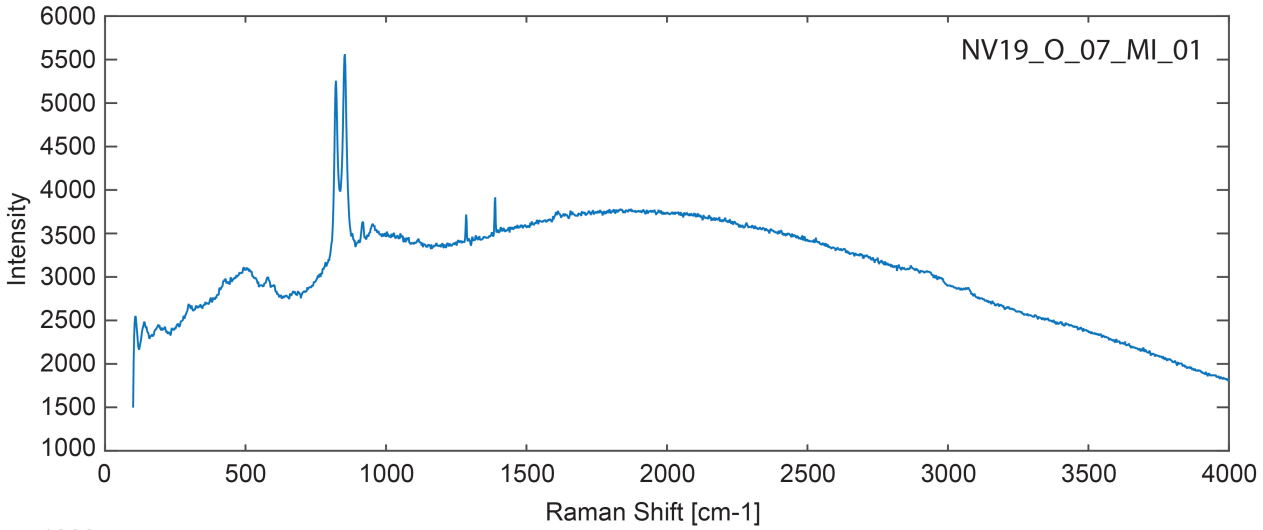
NV19_O_07_MI_01
Intensity
Raman Shift [cm-1]
6000
5500
5000
4500
4000
3500
3000
2500
2000
1500
1000
0
500
1000
1500
2000
2500
3000
3500
4000

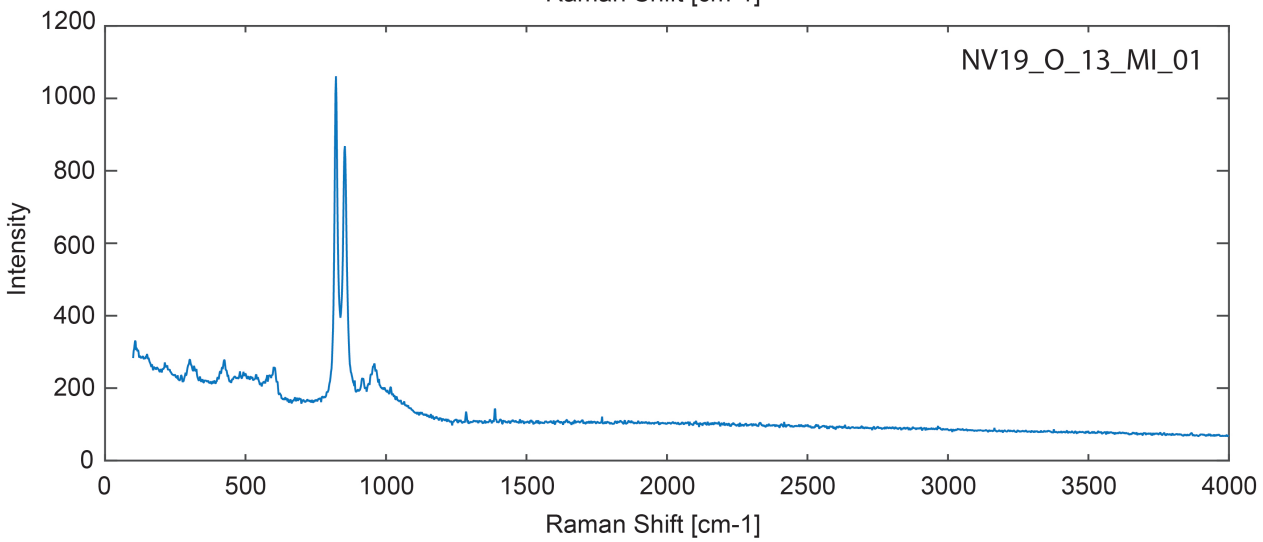
NV19_O_13_MI_01
Intensity
Raman Shift [cm-1]
1200
1000
800
600
400
200
0
500
1000
1500
2000
2500
3000
3500
4000

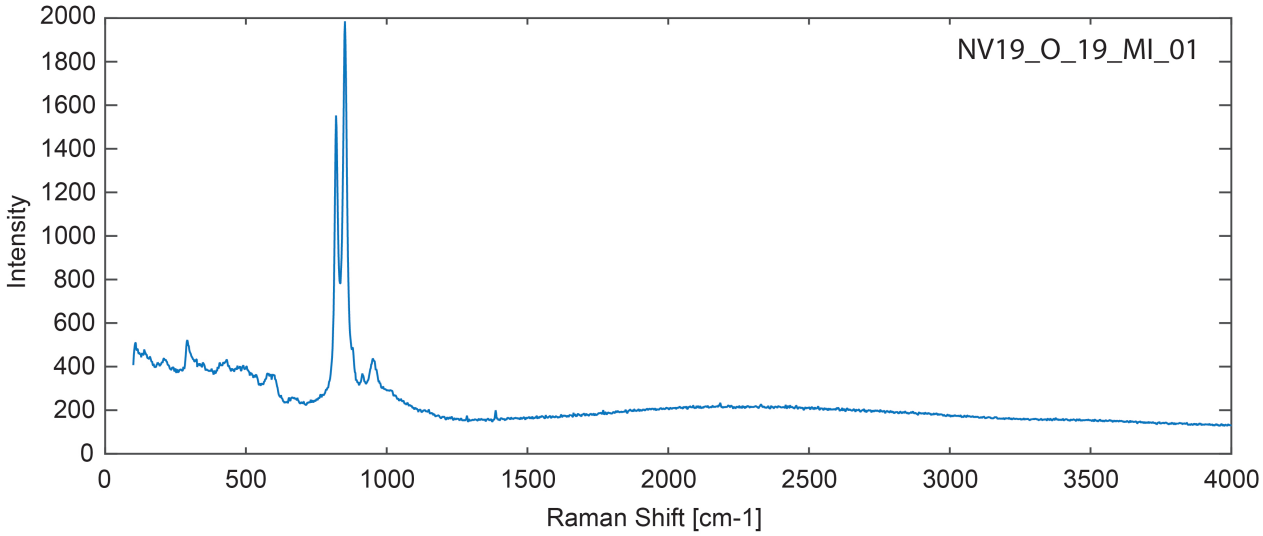
NV19_O_19_MI_01
Intensity
Raman Shift [cm-1]

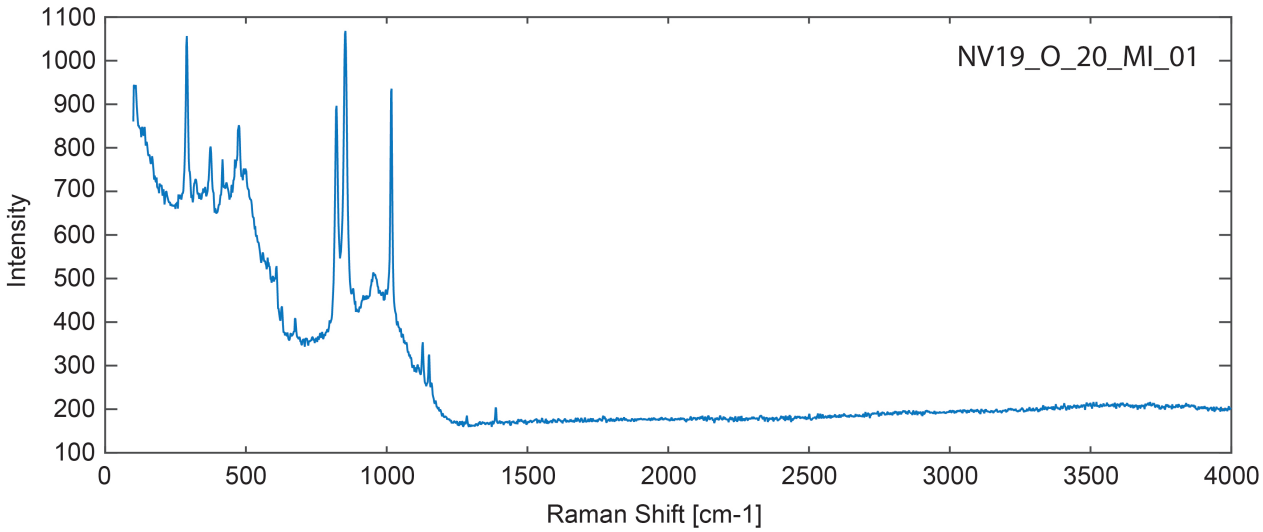
NV19_O_20_MI_01
Intensity
Raman Shift [cm-1]

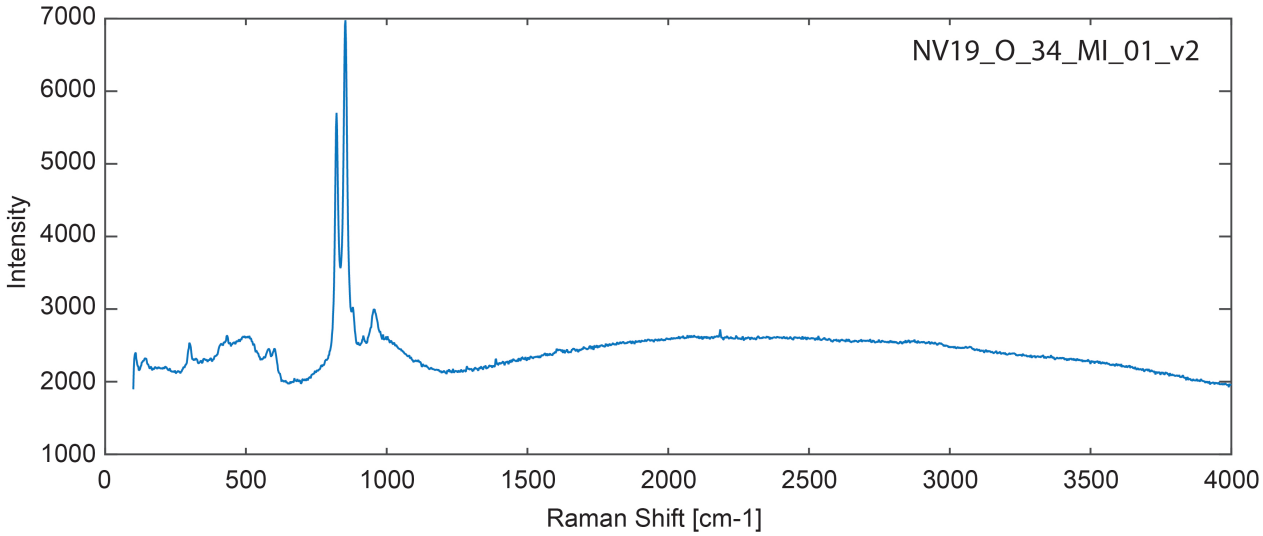
NV19_O_34_MI_01_v2
Intensity
Raman Shift [cm-1]